Beam Dynamics Studies in Recirculating Machines

THÈSE N° 6981 (2016)

ÉCOLE POLYTECHNIQUE FÉDÉRALE DE LAUSANNE

POUR L'OBTENTION DU GRADE DE DOCTEUR ÈS SCIENCES

PAR

Dario PELLEGRINI

ÉCOLE POLYTECHNIQUE
FÉDÉRALE DE LAUSANNE

Suisse
2016

Quality means doing it right when no one is looking.
— Henry Ford

Acknowledgements

Riassunto

L'LHeC e il Drive Beam di CLIC condividono non solo le alte correnti di fascio che li rendono proni a mostrare instabilità, ma anche lattice e schemi operativi non convenzionali, nei quali la sequenza temporale dei bunch varia lungo la macchina. Per stabilire la fattibilità di questi progetti occorrono simulazioni realistiche che considerino i principali effetti di dinamica di fascio e le loro interconnessioni. Questi includono ottica lineare e non lineare con elementi dipendenti dal tempo, radiazione di sincrotrone coerente e incoerente, wakefields a corto e lungo raggio, effetto beam-beam e accumulo di ioni.

Per potere investigare effetti multi-bunch in macchine ricircolanti, è stata scritta ex-novo una nuova versione del codice di tracciamento PLACET. PLACET2 integra già la maggior parte degli effetti menzionati in precedenza e può facilmente ricevere ulteriore fisica. Il suo design innovativo permette di descrivere lattice complessi e tracciare uno o più bunch in accordo con l'operazione della macchina, riproducendo la divisione di un treno di bunch su più linee di fascio.

A seguito dei test preliminari, PLACET2 è stato applicato al design dell'LHeC basato su un Linac a recupero di energia completando la prima simulazione di tracciamento da iniettore a dump. Il trasporto del fascio è stato verificato in presenza di radiazione di sincrotrone incoerente ed effetti di wakefields e beam-beam. In sezioni specifiche del lattice, sono state rilevate perdite di energia per radiazione inaspettatamente alte e sono state proposte soluzioni per migliorare le prestazioni della macchina e la qualità del fascio. Queste incudono un nuovo design delle sezioni di separazione del fascio, ed archi di ritorno basati su magneti a funzione combinata. Il bypass del detector, che era inizialmente mancante, è stato disegnato e integrato nella macchina.

Sono state completate simulazioni di tracciamento anche per PERLE, la quale è stata sviluppata per validare su piccola scala la tecnologia e l'operazione dell'LHeC. Le sue prestazioni sono state verificate ed il design è stato consolidato e migliorato.

Il lavoro a CTF3 è stato focalizzato sul Combiner Ring. La sua lunghezza gioca un ruolo fondamentale nel determinare la fase del fascio ricombinato e deve essere regolata con attenzione. La possibilità di controllare la lunghezza dell'anello tramite variazioni dell'ottica è stata misurata sulla macchina e riprodotta con il modello in PLACET2. Inoltre il programma è stato utilizzato per riprodurre un'instabilità di tipo multi-bunch, che apparì durante la messa in

Riassunto

opera della macchina.

Parole chiave: Fisica degli Acceleratori, Collisori di Particelle, Dinamica di Fascio, Ricircolazione, Simulazioni di Tracciamento, Effetti Collettivi, Effetti Multi-bunch, Linac a Recupero di Energia, LHeC, CLIC, CTF3.

Abstract

The LHeC and the CLIC Drive Beam share not only the high-current beams that make them prone to show instabilities, but also unconventional lattice topologies and operational schemes in which the time sequence of the bunches varies along the machine. In order to asses the feasibility of these projects, realistic simulations taking into account the most worrisome effects and their interplays, are crucial. These include linear and non-linear optics with time dependent elements, incoherent and coherent synchrotron radiation, short and long-range wakefields, beam-beam effect and ion cloud.

In order to investigate multi-bunch effects in recirculating machines, a new version of the tracking code PLACET has been developed from scratch. PLACET2, already integrates most of the effects mentioned before and can easily receive additional physics. Its innovative design allows to describe complex lattices and track one or more bunches accordingly to the machine operation, reproducing the bunch train splitting and recombination to and from multiple beamlines.

After some initial testing, PLACET2 has been applied to the LHeC Energy Recovery Linac design in order to complete the first end-to-end tracking simulation. The transport of the beam to the dump has been verified in presence of incoherent synchrotron radiation, wakefields and beam-beam effect. Unexpected high radiation losses have been found in specific sections of the lattice, solutions have been proposed to improve both the machine performance and the beam quality. These include a new design of the spreading sections and return arcs based on combined function magnets. The detector bypass, that was originally missing, have now been designed and integrated in the lattice.

Tracking simulations have also been performed for PERLE, which have been developed to validate on a smaller scale the technology and the operation of the LHeC. Its performances have been assessed and the design has been consolidated and improved.

The work at CTF3 focused on the Combiner Ring. Its length plays a crucial role in the phase structure of the combined beam and must be carefully tuned. The control of the ring length by means of optics scaling, has been measured on the machine and reproduced with the PLACET2 model. Moreover the code has been used to verify a multi-bunch instability that

Abstract

appeared during the commissioning of the ring.

Key words: Accelerator Physics, Particle Collider, Beam Dynamics, Beam Recirculation, Tracking Simulation, Collective Effects, Multi-bunch Effects, Energy Recovery Linac, LHeC, CLIC, CTF3.

Contents

Contents

1 Why Beam Recirculation

The LHC Run 1, completed in 2012, led to the discovery of an Higgs-like particle, potentially completing the Standard Model of Particle Physics. This great success rewards commendable efforts spent into the design, construction and operation of the greatest collider ever built. Nevertheless we consider our understanding of Universe far from being complete. A number of questions regarding for instance the origin of matter-antimatter asymmetry, the nature of dark matter and dark energy, the reason for having three generations of quarks and leptons with such a different mass scale, are still unanswered. Theoreticians have proposed a number of theories beyond the Standard Model, but none of them has yet been experimentally validated.

At the time of writing, after a period of major consolidation, the LHC is back online at an almost doubled energy and the physics community is striving to overcome the theoretical impasse. While the Run 2 data taking is ongoing, the debate on what will be the next machine at the energy frontier is stronger than ever and a number of alternatives are being prepared.

The main protagonists of this debate are a new generation of *circular colliders* approximately three times larger than the LHC and being designed to reach proton-proton collisions at energies up to 100 TeV; and the *linear colliders* which plan to accelerate and collide electrons and positrons up to 3 TeV by means of linear accelerators. Indeed, as the light leptons are nearly 2000 times lighter than protons, when they are bent in circular orbits they radiates massive amount of energy, making an electron storage ring at the TeV scale extremely impractical and expensive, if not impossible. Other machines have been proposed, such as *muon colliders* and *gamma-gamma colliders*, but the technological difficulties of the firsts, and the necessity to rely on primary charged beams for the seconds, pose them in the background.

In addition to the employ as discovery tools at the energy frontier, particle accelerators have found applications spanning from basic sciences to medical and industrial utilisation. Today the research in accelerator physics points not only at increasing the energy, but also the intensity, the cost and the reliability of these versatile machines.

In this multi-coloured context, beam recirculation techniques are gaining more and more

attention following from the excellent ratios between the beam parameters and machine size and cost that they can achieve. Making the beam travel few times through the same elements, it is possible to obtain compact designs, which characterise rings; but at the same time, as the beam keeps a relatively short path into the machine, its parameters be pushed as hard as in linacs, where there is no need to obtain stable equilibrium conditions.

The machine layouts resulting from the adoption of beam recirculation are more than variegate. However the targets at which recirculation aims are basically two: *energy increase*, with multiple passages on the accelerating phase of field, and *energy recovery*, with passages on the decelerating phase. One recirculating machine standing out from this classification is the CLIC Drive Beam, whose goal is to modify the time structure of a train of bunches; details are discussed in Sec. 1.2.1.

In the next sections we will review how beam recirculation is employed to obtain attractive beam parameters in a wide field of applications.

1.1   Applications of Beam Recirculation

1.1.1   Colliders

A particle collider has two crucial parameters: the collision energy and rate (or *luminosity*). To obtain a general figure of merit, these have to be normalized with respect to the power consumption and the overall cost of the machine.

When two bunches cross, of the many billions of particle that they may contain, only very few actually collide. Therefore rings, storing the accelerated beams and colliding them multiple times, have an intrinsic advantage over linacs, which discard the beams after a single crossing. However, in case of light particles such as electrons, rings suffer from synchrotron radiation which causes energy losses and increases the beam sizes. Therefore, while at low energy rings are very effective, the TeV scale is only accessible with linear collider. The competitiveness of linacs at medium energy, say from 10 to 100 GeV, can match the one of rings by employing recirculating techniques. Indeed at these energies the beams can still be bent, but the emission of radiation is significant. A linac can deliver smaller beams and focus them more at the collision point without concerns about their long term stability.

A linac-based collider can be made more compact and cost effective by applying multi-turn acceleration and can maintain a low power consumption extracting the energy of the collided beam decelerating it. The compactness and the flexibility of these linacs make them suitable to match existing beams: a common situation in the field of electron-hadron collisions encountered in studies such as the LHeC [1] and the eRHIC [2]. Another example of a high energy collider based on recirculation is SAPPHiRE [3] which aims at accelerating powerful electron beams to produce photon beams for collisions.

1.1.2 Light Sources

Light Sources are facilities optimized to generate high quality synchrotron radiation with many application in material, biological and medical sciences. The radiation can be extracted from the bending magnets, although higher intensities and cleaner spectra are obtained with special *undulator* magnets. Although there exists an ultimate physical restriction to the radiation sharpness following from diffraction, the limit coming from the beam quality is generally encountered first.

To improve the beam parameters (in particular the bunch length and the peak current) while maintaining high average currents, a new generation of ERL-based light sources is currently under study. The simplest designs are composed of a full-energy linac and an oval-shape return arc which hosts many light lines. These facilities are often coupled to a Free Electron Laser (FEL).

Free Electron Lasers generate intense pulses of coherent electromagnetic radiation spanning from the infrared to the X-rays. The radiation builds up in long undulating sections (properly matched to stimulate a micro-bunching instability) and reaches a gain of several order of magnitudes in the emitted radiation intensity. To ensure the high brilliance and the quality of the radiation, the bunches must be very intense, short and the transverse emittance needs to be kept as small as possible. The small beam sizes are provided by linacs, delivering beams in the energy range from some tens of MeV up to 17.5 GeV in the case of the Euro XFEL [4].

There are two main tendencies in the design of FELs, which derive from the linear colliders technologies. By adopting the CLIC warm x-band technology one aims at achieving high gradient acceleration, obtaining compact and cheap facilities. On the other hand the employment of superconducting technology allows for boosting the repetition rate and the radiation flux.

Although the lasing process strongly affects the quality of the beam, energy recovery (at least partial) can be applied to FELs allowing higher average currents. This was demonstrated at the JLab FEL [5] with superconducting technology and at the NovoFEL [6] with warm technology. Nowadays many small scale or testing facilities are being built and operated all around the world, paving the path to larger projects such as the Femto Science Factory [7] (Germany), and the XFELO [8] (Japan). The latter, whose concept is shown in Fig. 1.1, is based on a 3 GeV linac and foresees two operation modes: the energy recovery, with high current in the return arc, and the two-turn acceleration, delivering a 6 GeV beam to the FEL line.

Compton Scattering

Photon energies in the γ-rays range can be obtained by means of Compton back scattering of low energy photons on an electron beam. According to the desired photon energy, which typically spans in the tens of MeV, the required energy of the electron beam is around 1 GeV. Compton facilities may rely on a ring (as HIγS [9]), although the highest photon fluxes are obtained at linacs (as ELI-NP [10]). Compton scattering may not fully deplete the electron
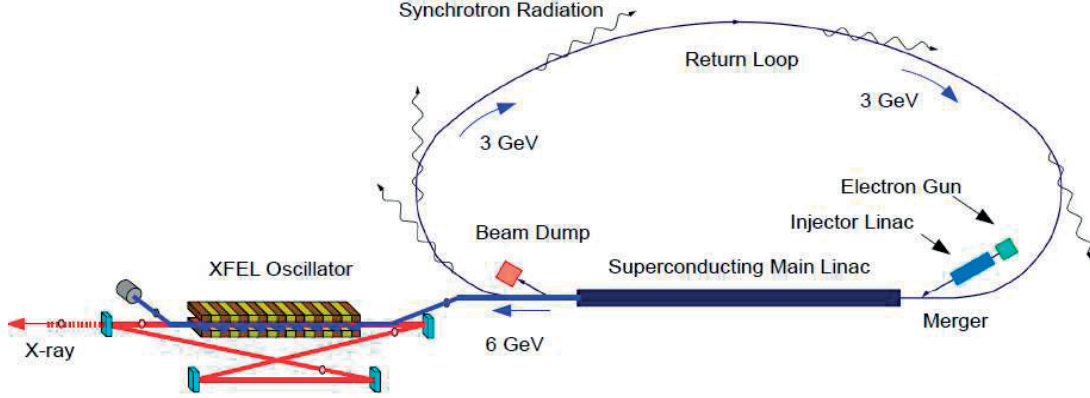
Figure 1.1: Conceptual layout of the 3 GeV ERL light source integrated with an XFEL oscillator at KEK [8].

beam, in these cases the application of energy recovery allows for higher intensity. The feasibility of a ERL-based Compton Scattering facility has been explored for PERLE [11], a small scale ERL facility in the design phase at CERN, with very promising results.

1.1.3 Electron Cooling

Electron cooling allows to reduce the beam emittance of a hadron beam, by superimposing an electron beam. Their velocities are matched and the coulomb interaction transfers the chaotic motion between the two beams, effectively reducing the emittance (or the temperature) of the ion beam. At a collider one may whish to keep the cooling active during collision in order to counteract the emittance growth given by the beam-beam and the intrabeam scattering.

While at low energy the electron beams for the cooling are simply generated with DC voltages, higher energy hadron beams are more demanding. Indeed the cooling efficiency drops with γ^2, so the electron beams need to be pushed both in energy (up to tens of MeV) and intensity (up to fractions of A), resulting in important powers. The energy recovery in this case becomes essential and ERL-based electron coolers play a crucial role in delivering a continuous, intense, low-emittance beam at a tolerable power consumption.

1.1.4 Fixed target and gas target experiment

Although the energy frontier is now domain of colliders, many intensity demanding experiments are pursued with fixed and gas targets. In these cases the high density of the target (compared to a beam) relaxes the requirements on beam intensity. As the centre of mass energy only goes with the squared root of the beam energy, the acceleration may profit from recirculation, achieving compact machines delivering low currents, but high energy beams to the experiments. This is the case of CEBAF [12] at JLab: an extremely versatile machine which

can simultaneously feed up to four experiments with beams with different intensities and energies by extracting them from the linac at different turn numbers. Its layout is presented in Fig. 1.2.
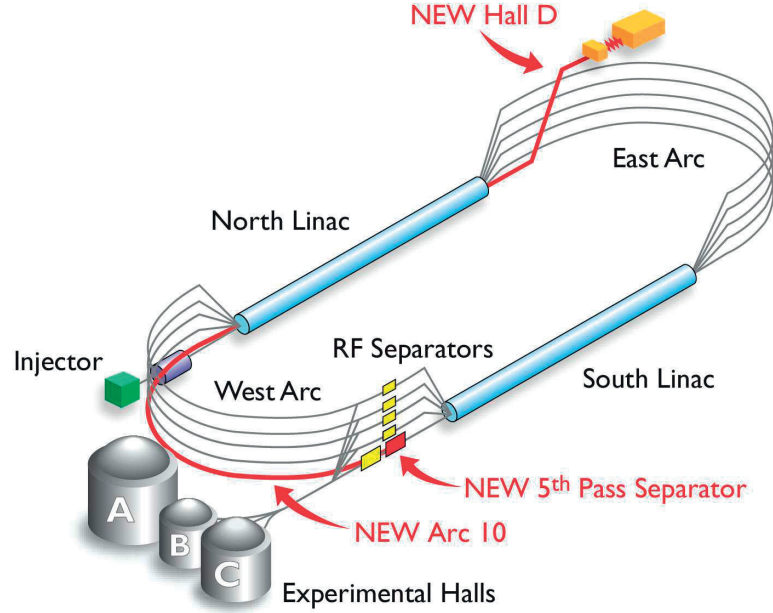
Figure 1.2: The CEBAF layout highlighting the interventions of the 6 GeV to 12 GeV upgrade (additional cavities have also been added in the linacs) [12].

If thin or gas targets are chosen, the energy recovery may also be advantageous, an example is the MAGIX [13] experiment at MESA (Germany).

1.1.5 Muon injectors

Being fundamental particles, $\mu^+\mu^-$ collision are potentially as clean as the ones between e^+e^-. Their mass, 200 times bigger than the electron one, makes them much less prone to emit synchrotron radiation, therefore they can be stored them in multi-TeV rings for collisions. However muons have an average lifetime of only 2.2 µs which drives the design of the whole machine.

The components of a muon collider consist in a production and cooling stage, a full energy injector and a fixed-field storage ring for collisions. In particular the injector needs to provide extremely fast acceleration from the GeV to the TeV scale. Multi-pass linacs either in racetrack or in dogbone [14] configuration are the most promising designs. They allow one to maintain a small number of components while avoiding the requirement of varying the field of the magnets during the acceleration (as in a synchrotron) which would slow it down to unacceptable time scales.

1.2 Linear Colliders

Collisions between e^+e^- beams at the TeV scale are conceivable only by means of Linear Colliders, which, avoiding to bend the beam, circumvent the massive energy losses and beam degradation caused by synchrotron radiation at that energy scale. Although each pair of bunches collides only once, competitive luminosities are obtained taking advantage of the very contained beam sizes coming from strong focussing and low emittance. The limitation coming from the disruption of the crossing beams (beam-beam effect) is much more relaxed compared to what is acceptable in a ring.

The two present studies for Linear Colliders, CLIC [15] and ILC [16], share a number of issues and fundamental concepts. Their main components are: the particle sources of which the positron one is particularly challenging, the damping rings which cool the beams down to very small sizes, the main linacs which accelerate the beams to full energy, the beam delivery system including the final focus, and, finally, a post-collision diagnostic lines and the dumps. The technology choice for the main linacs has a cascade of consequences on the machine design and performances which, in the case of CLIC, results in an extensive use of beam recirculation to distribute the power to the main linacs.

While ILC plans to use 1.3 GHz superconducting cavities to minimise power losses and extend the pulse duration, CLIC aims at maximising the accelerating gradient employing 12 GHz normal conducting cavities, therefore targeting an higher energy: 3 TeV centre of mass versus 1 TeV of the ILC. The adoption of warm cavities forces CLIC to have extremely short pulses (244 ns), to minimize ohmic losses caused by the storage of RF power into the cavities, but also to reduce the breakdown rate in presence of very high accelerating gradients[1].

The RF specifications of the CLIC main linacs would require 35 000, 50 MW klystrons operating at 12 GHz, together with their ancillaries. To reach the 244 ns pulse length, a factor ~5 time compression needs to be introduced, leading to important power losses. This rather unattractive, if not impossible, solution is circumvented with the concept of two beams acceleration. The Drive Beam Complex, acting as a gigantic klystron, accelerates long trains of bunches and rearranges their structure to match the main linac RF requirements, finally transferring the power to the colliding beams. The complete CLIC layout is schematised in Fig. 1.3, which shows both the Main Beam and the Drive Beam Complexes.

1.2.1 The CLIC Drive Beam Recombination Complex

In the CLIC Drive Beam Complex 1638, 1 GHz klystrons produce 15 MW, 142 µs pulses which are used to accelerate a train of 70 272 bunches at 0.5 GHz up to 2.4 GeV. The peculiar lattice topology of the Recombination Complex, composed of one delay loop and two combiner rings, splits this train in 24 parts and folds each of them 24 times. The resulting beam consists

---

[1] An empirical law for the break down rates states [17]: $BDR \propto E^{30}\tau^5$ where E is the gradient and τ the pulse duration.
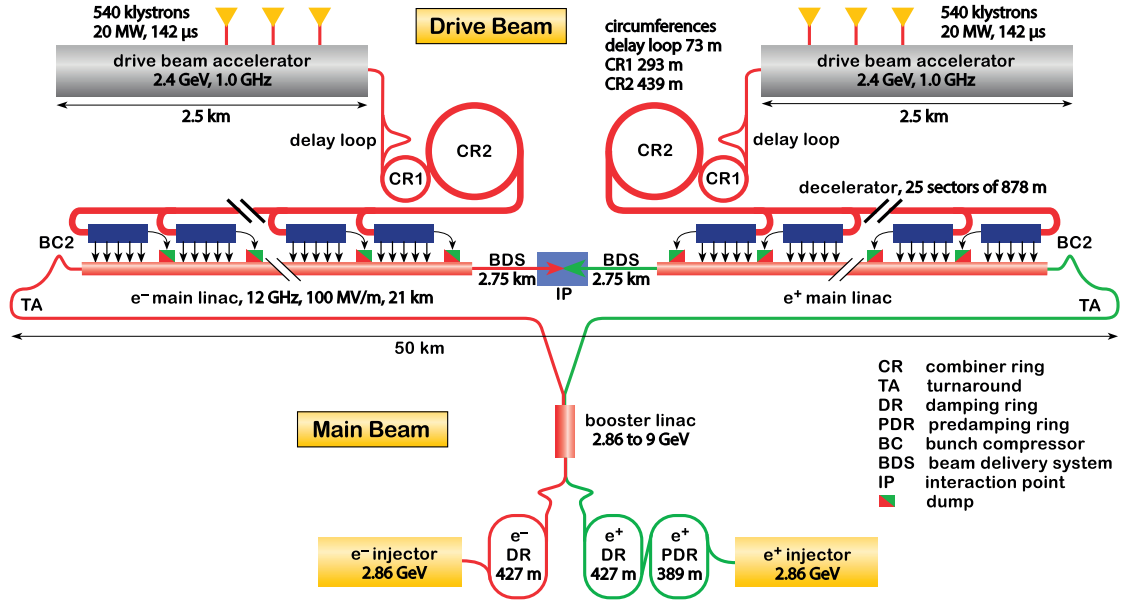
Figure 1.3: The layout of CLIC including both the Main Beam and the Drive Beam Complexes [15].

of 24 bursts of 100 A average beam current, separated by 5612 ns. These bursts are 244 ns long and contain 2928 bunches at 12 GHz. Note that the actual numbers may be slightly different in order to compensate for transients. The so structured Drive Beam is directed to the main linac tunnel. The Power Extraction and Transfer Structures (PETS) decelerate the Drive Beam and transport its power to the nearby accelerating structures of the main beam under the form of RF. The properly timed Main Beam receives this power minimising its storage in the cavities and therefore the ohmic losses and the breakdown rate.

The full schematics of the CLIC Drive Beam Complex is shown in Fig. 1.4. The recombination process starts at the source: bunches are generated at 0.5 GHz, but every 244 ns the injector phase is rapidly shifted by 180° switching from even to odd bunches. The Drive Beam Linac, operating at 1 GHz, accelerates both of them. When the beam arrives at the delay loop, a 0.5 GHz RF deflector kicks the even bunches to a longer beamline, while the odd bunches take a shorter path. A proper calibration of the path lengths ensures that the two beams reach the second RF deflector with the right timing and become interleaved. 244 ns gaps are now present in the beam and the bunch frequency has been doubled.

The beam then proceeds towards the first Combiner Ring where it is injected by means of a 1 GHz RF deflector. Before completing the full turn, a second RF deflector, placed before the injection septum, creates an orbit bump. The length of the ring is tuned so that when first pulse completes the first turn, the second is starting to be injected. The first RF deflector simultaneously kicks the second pulse in the ring and closes the bump of the first pulse. A
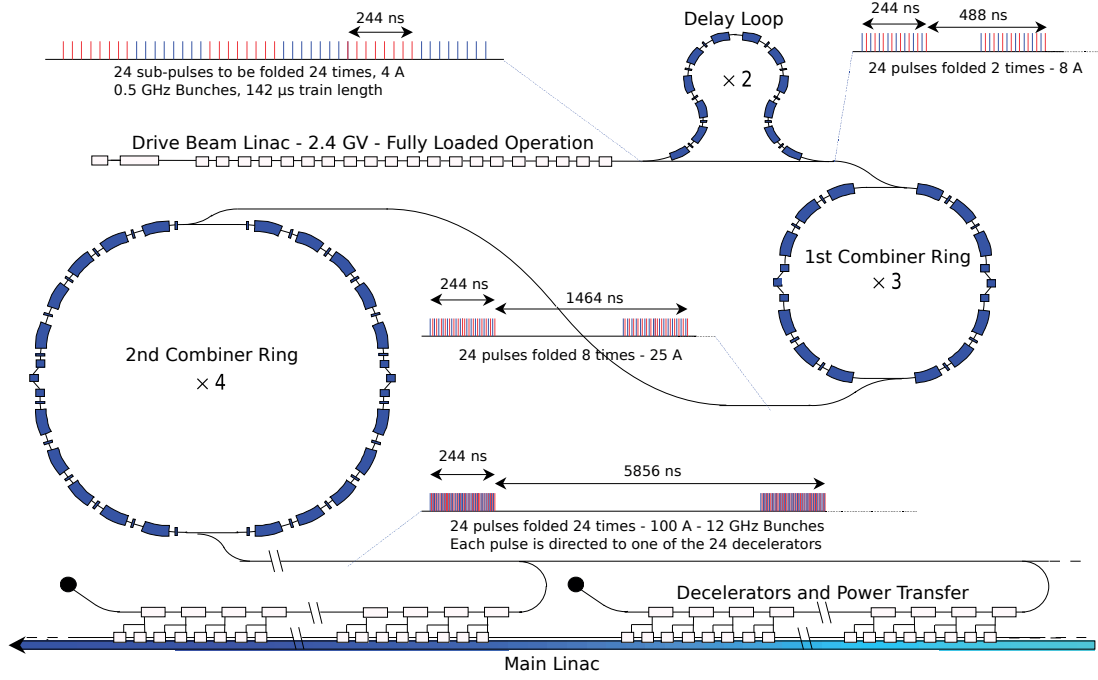
Figure 1.4: Detailed view of the CLIC Drive Beam Complex including the structure of the bunch train at each location.

further repetition of this injection process, allows one to obtain a factor three recombination[2]. The beam is then extracted and directed to the second combiner ring where, with a similar scheme, a factor four recombination is gained (see Fig. 1.5). The resulting beam, recombined by a factor $2 \times 3 \times 4 = 24$, has the properly time structure required to power the main linac.

It should be noted that all the components installed in the main tunnel require either a limited amount of power (quadrupoles, diagnostic, correctors) or none (PETS) and there is no need of a second tunnel hosting the klystrons, although 24 turnaround loops need to be dug to invert the direction of the drive beam pulses at each decelerating section.

Figure 1.6 shows a snapshot of a recombining beam with one delay loop and one factor four combiner ring. Two batches are already turning in the Combiner Ring, while a third one is being injected. The injector, located at $(0,0)$ generates bunches with a constant frequency, one can note how after the delay loop the frequency is doubled, while in the ring it is increased by another factor four.

---

[2]Carefully tuning the length of the ring, the injection can be repeated up to five times, maintaining enough separation between the orbit bump and the septum.

$$C_{ring} = (n + \tfrac{1}{4})\,\lambda$$
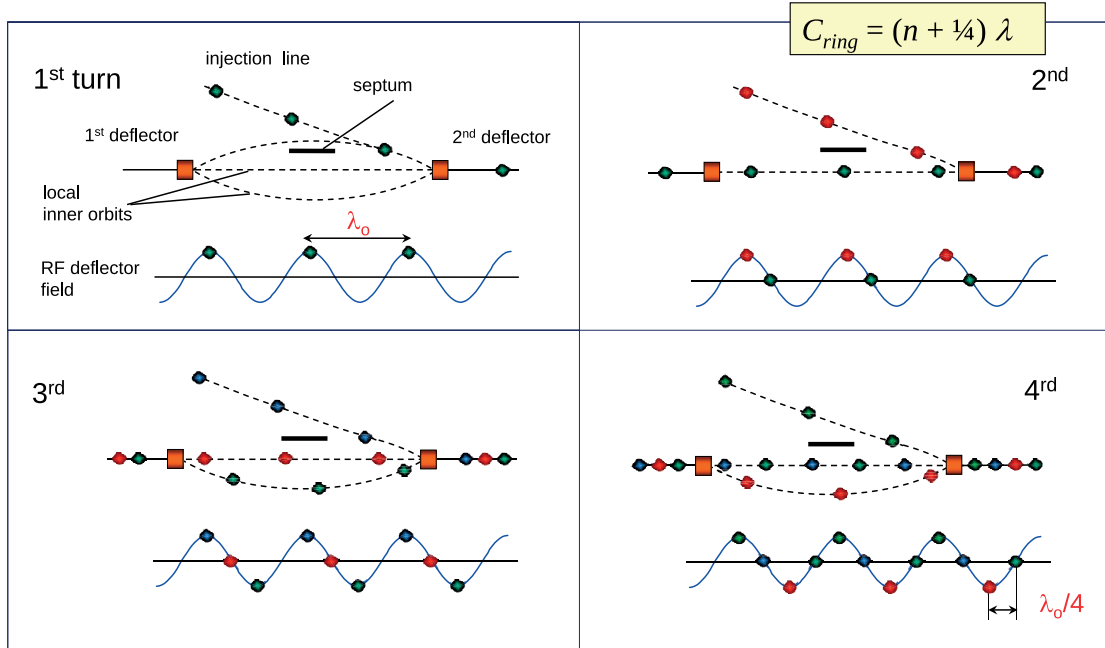
Figure 1.5: RF injection in a factor 4 Combiner Ring. The circumference of the ring is tuned so that the phase of the RF deflectors is shift of $\pi/2$ at every turn. The two deflectors kick open and close orbit bumps for the turning bunches while while new bunches are kicked on the closed orbit. By tuning the length of the ring and the extraction timing, the combination factor can even be pushed to 5, beyond that the bumps pass too close to the septum.
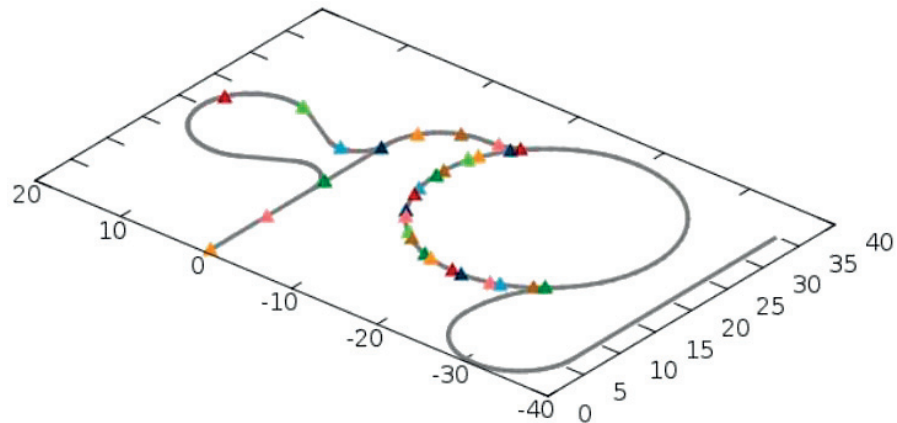
Figure 1.6: Illustration of the beam recombination process. Each triangle represents a bunch. The bunches enter into the lattice from the line starting at 0,0. Note how the bunch spacing after the delay loop, and then in the ring, decreases compared to the one at the injection.

2 Beam Physics and Modelling of Single and Multi-bunch Effects

In this chapter we will introduce and contextualise different physics effects that are relevant to the investigated projects. We will cover wakefields, synchrotron radiation and beam-beam effects. These are critical aspects of the beam dynamics of the LHeC, CLIC, CTF3 and many other accelerators. Their analytical descriptions will be presented, together with the fundamental concepts required for their derivation.

2.1 Short-Range Wakefields

When a charged particle travels through a vacuum chamber, it induces electromagnetic fields which can act back on the particle itself and on the trailing ones. The main sources of such fields are geometry variations of the beam pipe and the resistivity of the vacuum chamber. These cases (but also many other ones like coherent synchrotron radiation and space charge [18]) can be analysed by means of a *wake function*. We shall now see how it is defined and how it can be used.

2.1.1 Wake Function and Impedance

Consider a system of two charges q_1 and q_2, with the same velocity $v = v_z = c$, separated by a distance z. The fields generated by q_1 result in a force that acts on q_2:

$$\boldsymbol{F} = q_2 \left[(E_x - v_z B_y)\hat{\boldsymbol{x}} + (E_y + v_z B_x)\hat{\boldsymbol{y}} + E_z\hat{\boldsymbol{z}} \right] \equiv \boldsymbol{F}_\perp + \boldsymbol{F}_{/\!/}; \tag{2.1}$$

where a parallel component, oriented along the direction of motion and a transverse component, laying in the perpendicular plane, have been separated.

Integrating the force in the longitudinal direction one gets a change of energy for the longitudinal direction, and a deflecting momentum in the transverse direction:

$$U = \int_0^L \boldsymbol{F}_{/\!/} \, \mathrm{d}s; \qquad \boldsymbol{M} = \int_0^L \boldsymbol{F}_\perp \, \mathrm{d}s. \tag{2.2}$$

In a system with cylindrical symmetry, it is convenient to write the Maxwell equations in cylindrical coordinates and apply a multipolar expansion to obtain the general expressions:

$$\int_0^L \boldsymbol{F}_\perp \, \mathrm{d}s = -q_2 I_m W_m(z) m r^{m-1} \left(\hat{r} \cos m\theta - \hat{\theta} \sin m\theta \right); \tag{2.3}$$

$$\int_0^L \boldsymbol{F}_\| \, \mathrm{d}s = -q_2 I_m W_m'(z) r^m \cos m\theta; \tag{2.4}$$

where $W_m(z)$ and $W_m'(z) = \mathrm{d}W_m(z)/\mathrm{d}z$ are functions to be determined.

At $m = 0$ one finds:

$$\int_0^L \boldsymbol{F}_\| \, \mathrm{d}s = -q_2 I_0 W_\|(z); \tag{2.5}$$

while the transverse component vanish. The intensity I_0 in this case coincides with q_1.

The first non-vanishing transverse component is the dipole one, obtained for $m = 1$:

$$\int_0^L \boldsymbol{F}_\perp \, \mathrm{d}s = -q_2 I_1 W_\perp(z) \left(\hat{r} \cos\theta - \hat{\theta} \sin\theta \right); \tag{2.6}$$

here θ represents the mode polarization. Without loss of generality one can set $\theta = 0$, orienting the polarization along the x axis:

$$\int_0^L \boldsymbol{F}_\perp \, \mathrm{d}s = -q_2 I_1 W_\perp(z) \hat{x}; \tag{2.7}$$

in this case I_1 becomes the dipole strength: $I_1 = q_1 x_1$.

Adjusting the units to get the energies in eV and the kick in radians, one gets, at the leading order:

$$W_\| = -\frac{1}{q_1 q_2} \Delta E \quad \left[\frac{\mathrm{V}}{\mathrm{C}} \right]; \tag{2.8}$$

$$W_\perp = -\frac{E_0}{q_1 q_2} \frac{\Delta x_2'}{x_1} \quad \left[\frac{\mathrm{V}}{\mathrm{C\,m}} \right]. \tag{2.9}$$

In the context of linear machines the wakes functions are often normalized with the structure length.

It is sometimes convenient to work in the frequency domain. This is done by Fourier transforming the wake functions, which defines the impedance:

$$Z_{\|m}(\omega) = \int e^{-i\omega z/c} W_m'(z) \frac{\mathrm{d}z}{c}; \tag{2.10}$$

$$Z_{\perp m}(\omega) = i \int e^{-i\omega z/c} W_m(z) \frac{\mathrm{d}z}{c}. \tag{2.11}$$

It should be noted that the derivation up to now did not include anything strictly related to wakefields. Indeed these function are very comprehensive and can be used to describe a number of effects. Some general properties can be derived restricting them to represent physical observables. For instance the wake function must be real. Causality also constraints the wake function, forcing $W_m(z) = 0 \ \forall \ z < 0$, although the opposite is true in the special case of overtaking radiation observed in the framework of coherent synchrotron radiation. We shall now proceed to specialize them for the case of wakefields, giving some additional properties.

Panofsky-Wenzel theorem

Panofsky-Wenzel theorem connects the transverse and the longitudinal directions of the wake function at the same order [19] and it is very useful both for measures and cavity design. It can be formulated for the force or for the impedance as follows:

$$\nabla_\perp \int_0^L \boldsymbol{F}_{/\!/} \, \mathrm{d}s = \frac{\partial}{\partial z} \int_0^L \boldsymbol{F}_\perp \, \mathrm{d}s; \tag{2.12}$$

$$Z_{/\!/ m}(\omega) = \frac{\omega}{c} Z_{\perp m}(\omega). \tag{2.13}$$

Beam loading theorem

The beam loading theorem states that a particle sees half of the longitudinal potential that it induces [20]. An easy prove can be given considering two equal charges following each other across an empty cavity with a separation equal to half of the RF period. Initially both the charges carry an energy E. When the first charge travels across the cavity it induces a potential V and its energy changes by $-qfV$, where f is an unknown fraction. The second charge loses energy as well, but also picks up the potential left by the first charge, therefore its energy changes by $-qfV + qV$. By comparing the energies before and after one gets:

$$E_1 + E_2 = \left(E - qfV\right)_1 + \left(E - qfV + qV\right)_2; \tag{2.14}$$

from which one sees that $f = 1/2$, therefore, in terms of wake function:

$$W_{/\!/}(0) = \frac{1}{2} W_{/\!/}(0^+). \tag{2.15}$$

2.1.2 Estimation of impedances and wake functions

The calculation of the impedance is an electrodynamic problem consisting in finding the fields produced by an exciting charge. A number of analytic models has been developed to approach the problem which can be very useful for preliminary studies [18]. When the design of a component has been established extremely accurate solutions can be obtained by means of numerical solvers, as HFSS [21] and Gdfidl [22]. The accuracy of these solvers has been

recently confirmed in a wakefield measure performed at FACET with a two-beam technique [23].

In linacs the dominating contributions to wakefields typically come from the RF cavities. The analytical expression for the longitudinal wake function in RF cavities was found by Gluckstern [24], with a modification by Yokoya and Bane [25]. At high frequencies the longitudinal *monopole* impedance is connected to the transverse *dipole* impedance by [26]:

$$Z_{\perp 1}(\omega) \approx \frac{2c}{\omega a^2} Z_{/\!/ 0}(\omega), \tag{2.16}$$

therefore allowing to obtain the transverse wake function short range approximation. These expressions, as summarised in [27], are:

$$W_{/\!/}(s) \approx \frac{Z_0 c}{\pi a^2} \exp\left(\sqrt{\frac{s}{s_{00}}}\right),$$

$$W_{\perp}(s) \approx \frac{4 Z_0 c s_{00}}{\pi a^4} \left[1 - \left(1 + \sqrt{\frac{s}{s_{00}}}\right) \exp\sqrt{\frac{s}{s_{00}}}\right],$$

with:

$$s_{00} = \frac{g}{8}\left(\frac{a}{\alpha(g/L)L}\right)^2, \tag{2.17}$$

where α stands for the electromagnetic constant and the geometrical parameters a, g, L are illustrated in Fig. 2.1. Figure 2.2 shows the plots of the wake functions for the LHeC cavity parameters as described in [28]. As a consequence of the large iris, the induced potentials are very small compared, for example, to the ones found in CLIC.
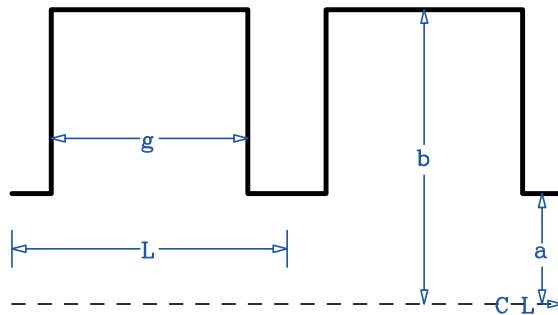
Figure 2.1: Geometrical parameters shown for two cells of the considered structure.
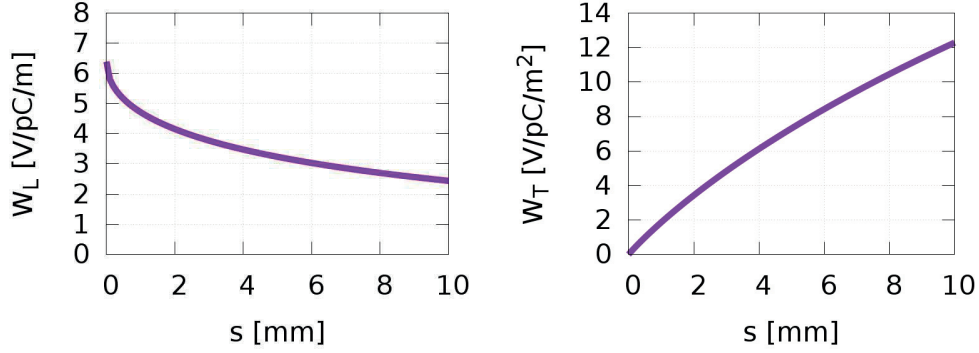
Figure 2.2: Longitudinal and transverse short-range wake functions computed for the LHeC cavity proposal.

2.1.3 Computational and Beam Dynamics aspects

The wake functions describe the potential generated by a single charge. The effect on a bunch is obtained convolving the single-particle wake function with the charge distribution, $\lambda(s)$:

$$V_z(z) = q \int_s^{+\infty} W_z(s - s') \lambda(s') \, ds', \tag{2.18}$$

$$V_x(z) = q \int_s^{+\infty} W_x(s - s') x(s') \lambda(s') \, ds'. \tag{2.19}$$

In the longitudinal direction, the effect of short range wakefields is the introduction of correlated energy spread which can be partially compensated by running the RF off crest. The wakes become more severe for shorter bunches; this is a consequence of the increased charge density, with an additional contribution from the fact that the wake function is larger at short distances.

In the transverse direction the wakes kick the tail of the bunch. In this case, following from the fact that the wake function starts from zero and rises with the distance, longer bunches suffer more. In order to better understand the influence of wakefields on the beam dynamics, a two-particle model can be considered [29]. Fixing a constant focussing strength: $K(s) = 1/\beta^2$ and arbitrary initial conditions, the Hill's equation describing the motion of the unperturbed leading particle becomes:

$$\frac{d^2 x_1}{ds^2} + \frac{1}{\beta^2} x_1 = 0; \qquad x_1(0) = x_0; \qquad \frac{dx_1}{ds}(0) = 0; \tag{2.20}$$

which is solved by:

$$x_1(s) = x_0 \cos\left(\frac{s}{\beta}\right). \tag{2.21}$$

For the trailing particle, there is an additional contribution from the wakefields which depends on the motion of the first particle. The transverse kick can be derived from 2.9 and added in the Hill's equation:

$$\frac{\mathrm{d}^2 x_2}{\mathrm{d}s^2} + \frac{1}{\beta^2} x_2 = \frac{q^2 W_x}{cP_z} x_0 \cos\left(\frac{s}{\beta}\right); \qquad x_2(0) = x_0; \qquad \frac{\mathrm{d}x_2}{\mathrm{d}s}(0) = 0; \tag{2.22}$$

this can be solved making an ansatz:

$$x_2(s) = x_0 \cos\left(\frac{s}{\beta}\right) + x_0 \frac{q^2 W_x \beta}{cP_z} s \sin\left(\frac{s}{\beta}\right). \tag{2.23}$$

It should be noted that the amplitude of the second particle grows linearly with s. Generally parameters such has the Twiss function and the momentum depend on s, therefore the amplitude of the second particle is related to the integral:

$$\int \frac{\beta(s)}{cP_z(s)} \mathrm{d}s \approx \int \frac{\beta(s)}{E(s)} \mathrm{d}s, \tag{2.24}$$

which suggests that the lattice should focus the beam stronger especially at low energies.

If the focussing strength of the second particle is changed: $\beta \to \beta'$, the new equation of motion becomes:

$$\frac{\mathrm{d}^2 x_2}{\mathrm{d}s^2} + \frac{1}{\beta'^2} x_2 = \frac{q^2 W_x}{E} x_0 \cos\left(\frac{s}{\beta}\right). \tag{2.25}$$

At this point one can note that, if the following condition is satisfied:

$$\frac{1}{\beta'^2} = \frac{1}{\beta^2} + \frac{q^2 W_x}{E}, \tag{2.26}$$

the second particle performs the same exact motion as the first particle, therefore cancelling the effect of wakefields. This was originally discovered by Balakin, Novokhatsky and Smirnov, therefore is called BNS damping [30, 31]. The fundamental idea consists in the fact that the defocussing kick received by the wakes, can be compensated by the kick in a quadrupole magnet if this is made stronger by lowering the particle rigidity. In fact, what one needs to do to suppress the effect of wakes, is to reduce the energy of the particles in the tail of the bunch by adjusting the RF phase. The correlated energy spread can be removed in the final section of the linac, where the high beam rigidity makes the wakes less effective.

2.2 Long-Range Wakefields

Long-range wakefields manifest themselves when the electric field induced by the beam builds up at particular locations of the accelerator and persist until the passage of additional bunches.

In this case the wake-function approach may require to compute the convolution with the charge distribution over a long train of bunches. This can be prohibitive or even impossible in the case of modification of the bunch train during the machine operation, as typically happens when the beam recirculation is in place. A local approach is therefore adopted. This consists in modelling the interaction between a bunch and a mode and apply it at every cavity, for every higher order mode (HOM) on top of the accelerating one.
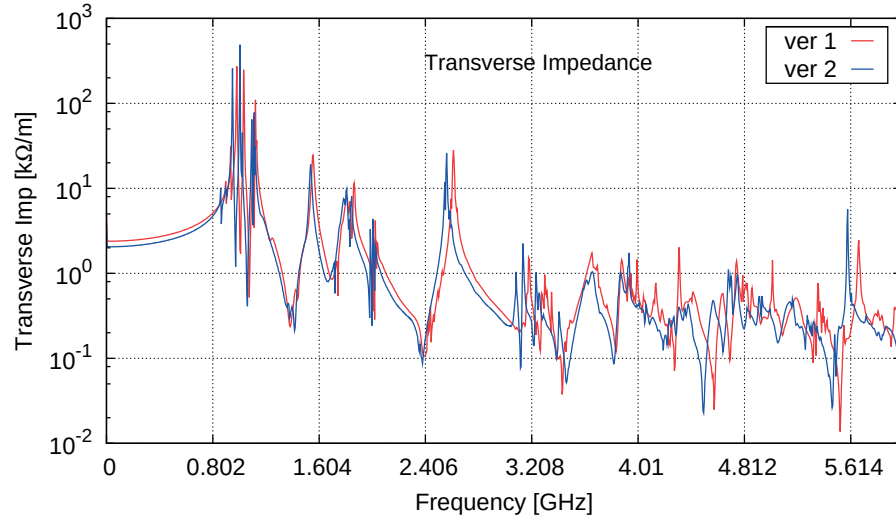
Figure 2.3: Impedance spectra for two LHeC cavity designs proposed in [28].

Figure 2.3 shows the transverse impedance spectra of the two proposed designs for the LHeC cavities [28]. Each peak in the spectrum corresponds to a transverse mode of oscillation of the electromagnetic field. These modes can be characterised with frequency, impedance and Q-factor (which is related to the width of the resonance). It is possible to convert the transverse impedance, measured in Ohm, to an amplitude, measured in V/C/m using the following relation:

$$A\,[\text{V/C/m}] = \frac{\omega^2}{cQ}\,I\,[\text{Ohm}], \tag{2.27}$$

which can be derived for instance from eq. 1 in [32]. In literature the amplitude A is sometimes multiplied by the wave number $k = 2\pi/\lambda = \omega/c$, and/or normalised with respect to the length of the cavity.

In first approximation the impedance is proportional to the frequency, therefore the amplitudes of the HOMs are proportional to ω^3. This relation was initially used to scale the modes available for the Superconducting Proton Linac cavity design [33] at 720 MHz to the LHeC frequency of 802 MHz.

2.2.1 Long Range Wakefields in Rings and Linacs

In a ring the perturbed bunches come back to the same locations. According to the tune, a kick received at the previous turn, may partially result in a displacement leading to additional loading of the modes. This positive feedback mechanism can lead to instabilities and losses, this scenario is called *regenerative* beam breakup. However the losses may take place slow enough so that the reduced intensity tends to make the beam stable again.

On the other hand, in a linac the excitation is initiated by the trailing bunches of the pulse. As more and more bunches reach the same cavity, they keep loading the HOMs, receiving in turn stronger and stronger kicks, which result in an additional loading of the HOMs in the following cavities. At the same time the trailing bunches are not very much perturbed and they keep seeding the excitation with their full intensity. In this scenario the long-range wakefields lead to *cumulative* beam breakup. In sufficiently long linacs, this leads to total disruption of the beam that, with the only exception of the leading bunches, is not able to reach the end.

When a linac is recirculated and operated with continuous injection, the beam feedback mechanism is added, on top of the big number of cavities. This can have dramatic effects on the BBU threshold current.

Analytical estimations of long-range wakefields effect in linacs date back to the sixties [34] but are found even in recent studies, for instance in [35] where they are applied to linear colliders. The studies have also been extended to ERLs [36], however in the case of LHeC the multi-turn recirculation, the great number of cavities and the many HOMs make the study particularly difficult and a simulation approach is preferred.

In the next sections we will present the physics of long-range wakefields as it is modelled in PLACET2 and we demonstrate its fundamental concepts applying it to a simple, single-cavity ERL. For this study we focus on the transverse modes, in particular the dipolar ones, which are strong and easily excited by orbit displacements.

2.2.2 Modelling and Computation

As the bunch train structure is modified during the operation of a recirculating machine, with continuous substitution of spent bunches with fresh bunches and modifications of the train structure, it is not possible to asses wakefields computation with a global approach. Therefore we adopt a local approach in which we model the interaction between a bunch and a mode. Arbitrary complex studies can then be performed filling the cavities with the relevant modes, setting up the train of bunches to be injected and letting the tracking core of PLACET2 propagate all the bunches preserving their time sequence.

As every oscillation process, the status of a mode can be represented with two parameters:

amplitude, ρ, and phase, θ. Complex numbers are therefore a natural choice:

$$z = \rho e^{i\theta}. \tag{2.28}$$

The time evolution of the mode in the absence of external perturbations, contains a damping term and rotation term:

$$z(t + \mathrm{d}t) = z(t) \underbrace{\exp\left(-\frac{\omega}{2Q} dt\right)}_{\text{damping}} \underbrace{\exp\left(i\omega dt\right)}_{\text{rotation}}. \tag{2.29}$$

The two interactions, Bunch $\rightarrow$ Mode (excitation) and Mode $\rightarrow$ Bunch (kick), can be written as:

$$\Im(z) = \Im(z_0) + Ne\,A\delta x; \tag{2.30}$$

$$x' = x'_0 + \frac{e\Re(z)}{\gamma\,m_e\,c^2}. \tag{2.31}$$

An incoming bunch interacts with the imaginary part of the mode. The strength of the interaction depends on the bunch charge Ne, the mode amplitude or impedance (A) and the offset of the bunch δx. After a rotation of 90° the mode excitation manifests itself as a voltage that kicks the bunch.
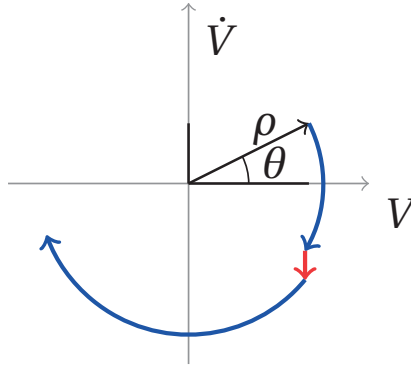
Figure 2.4: Scheme of the evolution of a mode, including the time rotation (blue) and the excitation from a bunch (red).

Figure 2.4 shows a representation of the evolution of a mode, including the excitation from a passing bunch. It should be noted that the damping in eq. 2.29 does not depend on the amplitude. Therefore if bunches keep exciting the mode with the same intensity (bigger than the damping), the mode grows indefinitely. In reality the growth is exponential, as a loop between orbit and mode excitation establishes.

This approach may appear rudimentary as it does not take into account the dispersion of the

modes, the bunch length and the group velocity of the cavity is forced to zero (only works for standing waves/trapped mode), nevertheless it is still capable of producing realistic results in a very fast way. This is a major requirement given the size of the LHeC ERL. For a more in-depth analysis of wakefields in travelling waves structures please refer to [37, 38] or, for a model developed for the CLIC decelerators, to [39].

2.2.3 Maximisation of the BBU threshold current

In presence of only one cavity with a single or dominant mode it is possible to estimate the threshold current with the formula:

$$I_{th} = \frac{2pc}{e\omega \frac{R}{Q} Q} \frac{1}{|T_{12}| \sin(\omega t_r)}. \tag{2.32}$$

Although this equation can rarely be applied in real-life cases, it summarises all the concepts that can be exploited to increase the BBU threshold current. In the first factor one finds the beam rigidity p/e and additional quantities (R, Q, ω) that can be targeted with the resonator design. The second factor contains terms related to the beam dynamics. The transfer matrix term: $T_{12} = \sqrt{\beta_1 \beta_2} \sin(\varphi)$ tells how much of the kick given at the first passage becomes a displacement at the second one, with the additional amplification given by the β functions. Finally the term $\sin(\omega t_r)$, where t_r is the arc time of flight, takes into account the phase of the mode, which is crucial to determine if the second interaction builds up the mode, or tends to suppress it.

When optimising the optics of a (recirculating) linac for the BBU one points to reduce:

$$\left\langle \frac{\beta}{E} \right\rangle = \int \frac{\beta}{E} ds, \tag{2.33}$$

maintaining the beam strongly focussed at low energies.

Equation 2.33 has been derived from the two-particle model described in Sec. 2.1.3, it also follows from eq. 2.32. A heuristic derivation can be obtained from the bunch-mode interaction described before. Indeed the contribution of the beam energy is evident in eq. 2.31, while the one of β appears both in eq. 2.30 and eq. 2.31, making the beam displacement $\delta x = \sqrt{\beta \varepsilon_c}$[1] bigger and decreasing the value of $x_0' = \sqrt{\varepsilon_c / \beta}$ therefore making the perturbation more significant. When the two terms are multiplied the linear dependency of the integral on β is obtained.

The betatron phase advance φ also plays a crucial role: in principle one would like to have $\varphi = n\pi$ between each cavity, so that the kick received at one cavity does not result in a dangerous displacement at the following one. However this requires multiple quadrupole magnets between the cavities and conflicts with the simplicity of the common FODO lattice. Still

---

[1] ε_c is the action of the bunch centroid.

scanning the phase advance in dedicated matching sections one may improve the threshold current.

Finally a proper tuning of the time of flight can totally suppress an offending mode to the point that no current can possibly excite it. In the next paragraph this possibility will be presented studying a single-cavity beam recirculator.

2.2.4 Analysis of a single cavity ERL

In order to familiarise with the physics described in the previous section, we consider a simple, hypothetical machine hosting one single cavity as shown is Fig. 2.5. The bunches go through the cavity, are recirculated by the arc and go through the cavity a second time before being dumped.
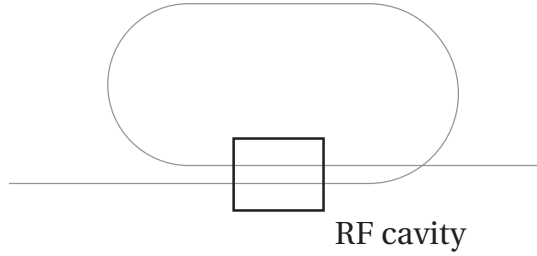
RF cavity

Figure 2.5: Scheme of a machine with a single localised source of HOMs, as could be a single cavity ERL.

The return line is a matrix that delays the beam and applies a betatron phase advance of 90°. The cavity is fitted with the 26 major transverse dipole HOMs from the Superconducting Proton Linac cavity design [33], as will be the case for the LHeC. An offset is given to the first bunch in order to initiate the excitation, before injecting half million bunches perfectly aligned, spaced by 25 ns. The charge of every bunch is increased until the threshold current is reached. This is shown in Fig. 2.6, where the amplitudes of the 26 modes are plotted every times that a bunch enters into the cavity.

As the instability is driven by a single mode that has become self sustained, one can adjust the time of flight to suppress that mode, and consequently the instability. The idea is illustrated in Fig. 2.7. The mode kicks the bunch at the first turn. When the bunch comes back, the betatron phase advance of 90° has fully transformed the kick into a displacement. However if the phase of the mode is correct, which means arriving at the right time, the bunch can extract energy from the mode, damping it.

Calling T_{HOM} the period of the offending mode and T_{arc} the time of flight, the condition that must be satisfied is:

$$\left(n \pm \frac{1}{4}\right) T_{HOM} = T_{arc} \qquad n \in \mathbb{N}. \tag{2.34}$$
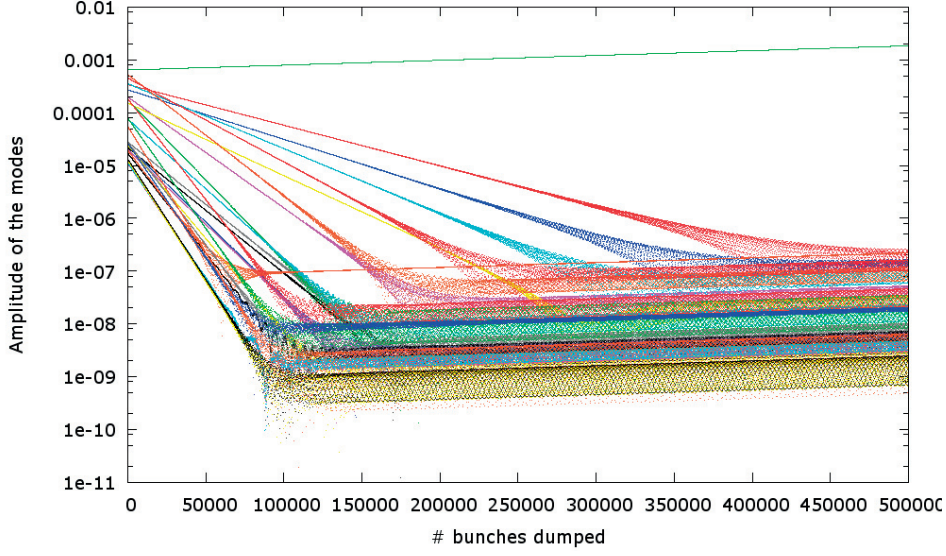
Figure 2.6: Amplitudes of the 26 modes in the cavity plotted every times a bunch goes through the cavity. The horizontal axis is scaled to that it coincides with the number of bunches that have been dumped. The single perturbation introduced at the beginning, survives indefinitely through one mode that has become self sustained, leading to an instability. The other modes can still contribute to the cross talking between different bunches, but they are not particularly dangerous. It can be noted that they decay to a minimum before starting to be sustained by the leading mode, growing with its same slope.

Here the factor 1/4 realizes the phase rotation of the HOM so that the interaction with the bunch is maximized at the second passage.

The + sign is for betatron phase advances between 0 and π (positive kick → positive offset)

The − sign is for betatron phase advances between π and 2π (positive kick → negative offset)

In the case of an ERL, T_{arc} must assume discrete values, according to the fundamental frequency of the cavity:

$$T_{arc} = \left(m + \frac{1}{2}\right) T_{RF} \qquad n \in \mathbb{N}, \tag{2.35}$$
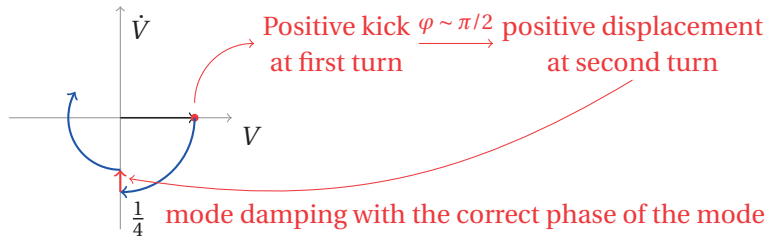
Figure 2.7: Concept of mode suppression by adjusting the time of flight.

Where the factor 1/2 is required to shift the RF phase from acceleration to deceleration.

Equating the left hand side of eq. 2.34 with the right hand side of eq. 2.35 one gets:

$$n = \frac{f_{HOM}}{f_{RF}}\left(m + \frac{1}{2}\right) - \frac{1}{4}. \tag{2.36}$$

Satisfying eq. 2.36 consists of finding integer values of m so that n is also (close to) an integer. For $f_{RF} = 802$ MHz and $f_{HOM} = 939.8$ MHz some of the smallest m which better approximate the solution are:

m	n
15	17.914
16	19.085
21	24.945
33	39.007
39	46.038
...	...

Figure 2.8 shows the modes with the same beam current as before, but with the arc length tuned to $m = 33$. The offending mode is now completely suppressed and the beam stability has been recovered.
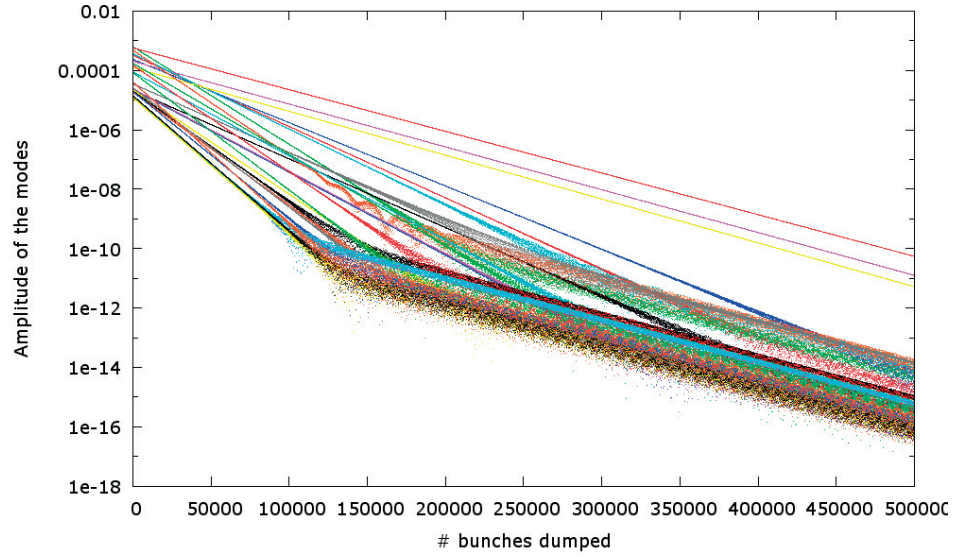
Figure 2.8: Amplitudes of the 26 modes in the cavity for a time of flight that suppresses the offending mode.

2.3   Synchrotron Radiation

The radiation emitted by accelerated charges is a critical point in the beam dynamics of high energy accelerators. It has been driving the design of electron and positron rings for the last half century, with many of them specifically built to optimise its emission. In the transport of high energy beams, for example in the LHeC recirculating arcs and in the CLIC Drive Beam, its effects need to be carefully evaluated and mitigated. In the final focus system of linear colliders it appears not only at the bending magnets, but also at the focussing ones, creating aberrations which goes under the name of Oide effect [40].

Nowadays it is considered also in proton machines. At the LHC it creates a heat load from within the beam pipe that has to be dissipated by the cryogenic system. In the future proton colliders it will lead to a reduction the beam emittance during the fill, with profound implications on the machine operation and, ultimately, affecting the luminosity profile.

In the next sections we will review the fundamental mechanism of radiation, with specific applications to the beam dynamics. We will not go through all the details of the derivations, but we will touch the conceptual steps and the main results. The work has been adapted from many sources: [41, 42, 43, 44] with additional contributions from [45].

2.3.1   Fundamentals

Charges at rest or in uniform motion are surrounded by a static field which extends to infinity. In the case of electric charges this field is called Coulomb fields and its intensity decays with the square of the distance. In the rest frame it can be written as:

$$\boldsymbol{E} = \frac{q}{4\pi\varepsilon_0} \frac{\boldsymbol{r}}{|\boldsymbol{r}|^3}. \tag{2.37}$$

Consider a charge in uniform motion and a distant observer. At the time t the charge is accelerated for a short interval $\mathrm{d}t$. As a consequence of the finiteness of the speed of light, this will not be readily known to the observer, which continues to see the field generated before the perturbation took place. On the other hand, close to the charge there is a new set of field lines, which obey the Coulomb law relatively to the uniform motion, after the perturbation. Somewhere in between the charge and the observer a distortion of the field lines is propagating at the speed of light. This distortion is called *radiation*. It will reach the observer at the time t', the *retarded time*, which depends on the *retarded distance d'* between the observer and the particle when it was accelerated:

$$t' = t + \frac{d'}{c}. \tag{2.38}$$

So, in general, if one wants to know the radiation at the time t, the relevant motion of the particle took place at the time $t - d'/c$.

If the observer absorbs the radiation its state is altered. For instance it can get accelerated in a similar way as the emitting charge was, which is the basic principle of radio communication. This tells that the radiation transports some energy in addition to the one of the Coulomb field, and this energy can only come from the emitting charge. Therefore a fundamental statement of the classical theory of electrodynamics is obtained: accelerated charges emits radiation and by doing that they loose energy.

2.3.2 Liénard-Wiechert fields

The general result that takes into account the arbitrary motion of relativistic charge for the computation of the electric field was found independently by Liénard (1898) and Wiechert (1900). The non-covariant formulation, which decouples the electric and magnetic fields, is:

$$E(x, t) = \frac{q}{4\pi\varepsilon_0} \left[\frac{n - \beta}{\gamma^2(1 - n \cdot \beta)^3 r^2} \right]_{\text{ret}} + \frac{q}{4\pi\varepsilon_0 c} \left[\frac{n \times \{(n - \beta) \times \dot{\beta}\}}{(1 - n \cdot \beta)^3 r} \right]_{\text{ret}} ; \tag{2.39}$$

$$cB = [n \times E]_{\text{ret}}. \tag{2.40}$$

Here n_{ret} represents the unit vector connecting the observation point with the position of the particle at the retarded time, while the distance value is given by r; β and γ are the Lorentz parameters.

Equation 2.39 contains two terms: the first is called *velocity field* as it only contains β, in the second one finds $\dot{\beta}$ and therefore it os called *acceleration field.* The velocity field decays with r^2, which is the same behaviour of the Coulomb field. Instead the acceleration field decays with r and therefore it is the dominant field to a far observer.

An alternative way to write the expression for the electric field is (O. Heaviside 1902, R.P. Feynman 1950):

$$E = -\frac{q}{4\pi\varepsilon_0} \left[\frac{n}{r^2} + \frac{r}{c} \frac{\mathrm{d}}{\mathrm{d}t} \frac{n}{r^2} + \frac{1}{c^2} \frac{\mathrm{d}^2}{\mathrm{d}t^2} n \right]_{\text{ret}}. \tag{2.41}$$

Here one recognizes the Coulomb term, together with a correction to it, and the acceleration term.

2.3.3 Angular distribution and total power

Let us consider a particle in uniform circular motion. One can chose the inertial frame of reference which moves tangentially to particle trajectory with the same speed of the particle. In this frame of reference the motion of the particle is seen as a cycloid: every time a revolution is completed, a cusp is obtained. Close enough to each of these cusps, the particle moves slowly and is subjected only to an acceleration perpendicular to the horizontal axis. Equation 2.39

can be rewritten taking into account only the acceleration term for $\boldsymbol{\beta} \to 0$:

$$E_a = \frac{q}{4\pi\varepsilon_0 c} \left[\frac{\boldsymbol{n} \times (\boldsymbol{n} \times \dot{\boldsymbol{\beta}})}{r} \right]_{\text{ret}}, \tag{2.42}$$

and considering the Poynting vector:

$$S = \varepsilon_0 c^2 \boldsymbol{E} \times \boldsymbol{B} = \varepsilon_0 c |E|^2 \boldsymbol{n}, \tag{2.43}$$

one can write the angular distribution of instantaneous emitted power:

$$\frac{dP}{d\Omega} = \frac{q^2}{16\pi^2\varepsilon_0 c} \left| \boldsymbol{n} \times \left(\boldsymbol{n} \times \dot{\boldsymbol{\beta}} \right) \right|^2 = \frac{q^2}{16\pi^2\varepsilon_0 c} \dot{\boldsymbol{\beta}} \sin^2 \Theta. \tag{2.44}$$

Where Θ is the angle between $\dot{\boldsymbol{\beta}}$, the acceleration, and $\boldsymbol{n}$, the observation direction. The emitted radiation is identical to the one form a Hertzian dipole and is illustrated in Fig. 2.9.
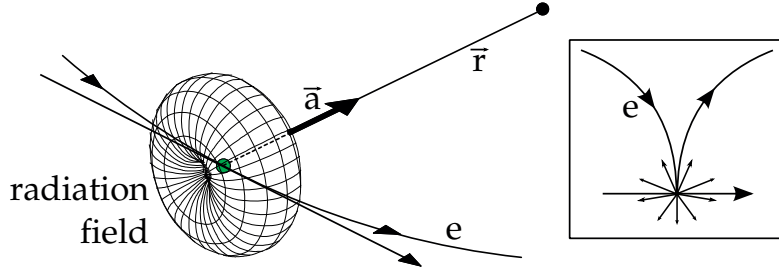
Figure 2.9: Radiation emitted in the co-moving frame of reference.

By integrating eq. 2.44 the classical Larmor formula is recognized:

$$P = \frac{q^2}{6\pi\epsilon_0 c} \left| \dot{\boldsymbol{\beta}} \right|^2. \tag{2.45}$$

To extract the property of the radiation in the laboratory frame, one needs to revise eq. 2.42 keeping the dependency on $\boldsymbol{\beta}$. In this case the spatial distribution is more complicated:

$$\frac{dP}{d\Omega} = \frac{q^2}{16\pi^2\varepsilon_0 c} \frac{|\boldsymbol{n} \times \{(\boldsymbol{n} - \boldsymbol{\beta}) \times \dot{\boldsymbol{\beta}}\}|^2}{(1 - \boldsymbol{n} \cdot \boldsymbol{\beta})^5}. \tag{2.46}$$

In a circular motion, $\boldsymbol{\beta}$ and $\dot{\boldsymbol{\beta}}$ are orthogonal. For $\gamma \gg 1$, this leads to:

$$\frac{dP}{d\Omega} \simeq \frac{q^2}{2\pi^2\varepsilon_0 c} \gamma^6 \frac{|\dot{\boldsymbol{\beta}}|^2}{(1 + \gamma^2\theta^2)^3} \left[1 - \frac{4\gamma^2\theta^2 \cos^2 \phi}{(1 + \gamma^2\theta^2)^2} \right]. \tag{2.47}$$

The velocity has been oriented along the z axis and the acceleration along the x axis, θ and ϕ are then the polar and the azimuthal angles. The peak radiation is emitted for $\theta \to 0$: in the forward direction, as shown in Fig. 2.10. At this point one can customarily define a cutoff

angle, θ_c by fixing the term at the denominator $(1 + \gamma^2 \theta_c^2) = 2$:

$$\theta_c = 1/\gamma. \tag{2.48}$$

The result is that most of the radiation is contained in a cone with aperture $1/\gamma$. A more rigorous definition will follow from the spectral analysis of the radiation.
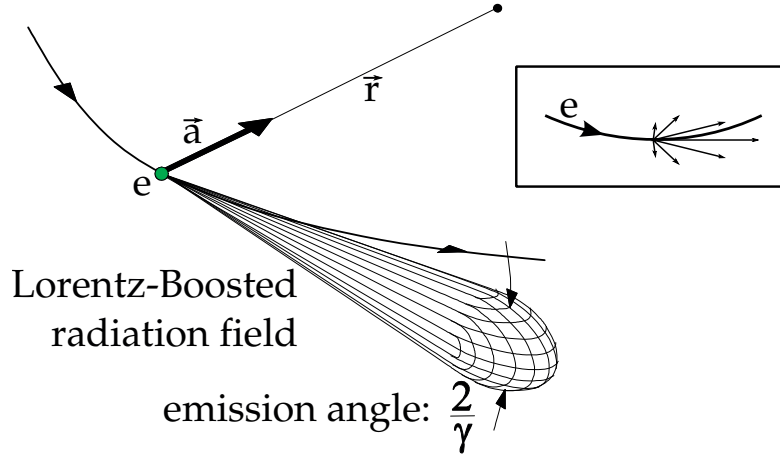
Figure 2.10: Radiation emitted in the laboratory frame of reference.

Again one can get the total power emitted by integration over the angles:

$$P_\gamma = \frac{q^2}{6\pi\varepsilon_0 c} |\dot{\boldsymbol{\beta}}|^2 \gamma^4 = \frac{q^2 c}{6\pi\varepsilon_0} \frac{\beta^4}{\rho^2} \gamma^4 = \frac{q^2 c}{6\pi\varepsilon_0} \frac{1}{\rho^2} \frac{E^4}{(mc^2)^4} = \frac{C_\gamma c}{2\pi} \frac{E^4}{\rho^2} \approx \frac{C_\gamma}{2\pi} c^3 q^2 B^2 E^2, \tag{2.49}$$

where we have introduced the centripetal acceleration: $\dot{\beta} = c\beta^2/\rho$; the particle energy: E and the constant: $C_\gamma = \frac{q^2}{3\varepsilon_0 (mc^2)^4}$. The last approximation allows to use the bending magnetic field: B.

The total energy lost by a particle travelling with some trajectory is obtained by integration:

$$U_0 = \int P_\gamma \, \mathrm{d}t \approx \int P \frac{\mathrm{d}s}{c} \approx \frac{C_\gamma}{2\pi} E^4 \int \frac{1}{\rho^2} \, \mathrm{d}s. \tag{2.50}$$

For historical reasons the last integral takes the name of *second radiation integral*:

$$I_2 = \int \frac{1}{\rho^2} \, \mathrm{d}s. \tag{2.51}$$

2.3.4 Power spectrum

The knowledge of the power spectrum is required for the treatment of the radiation as a quantum phenomenon, therefore allowing a proper evaluation of its effect on a particle beam. The power spectrum and its density are derived starting from the Fourier transform of the

electric field (eq. 2.39):

$$\tilde{\boldsymbol{E}}(\omega) = \frac{1}{\sqrt{2\pi}} \int_{-\infty}^{+\infty} \boldsymbol{E}(t) e^{-i\omega t} \, \mathrm{d}t. \tag{2.52}$$

As before the velocity is oriented along the z axis, x points along the bending radius and y is orthogonal to both. The integral can be computed for the two directions: x and y independently. The resulting expressions for the electric field are:

$$\tilde{E}_x(\omega) = \frac{-q}{\sqrt{24\pi^3 \varepsilon_0 c^2 r'}} \omega\rho \left(\frac{1}{\gamma^2} + \theta^2 \right) K_{2/3}\left(\xi\right), \tag{2.53}$$

$$\tilde{E}_y(\omega) = \frac{iq}{\sqrt{24\pi^3 \varepsilon_0 c^2 r'}} \omega\rho \left(\theta \sqrt{\frac{1}{\gamma^2} + \theta^2} \right) K_{1/3}\left(\xi\right), \tag{2.54}$$

where r' is the retarded distance, K are the modified Bessel functions and:

$$\xi = \frac{\omega\rho}{3c} \left(\frac{1}{\gamma^2} + \theta^2 \right)^{3/2} = \frac{\omega}{2\omega_c} \left(1 + \gamma^2\theta^2 \right)^{3/2}. \tag{2.55}$$

The critical frequency has been introduced:

$$\omega_c = \frac{3}{2} \frac{c}{\rho} \gamma^3. \tag{2.56}$$

The spectral content of the radiation is indeed sensitive to the polarization and one distinguishes between σ-mode (horizontal polarization) and π-mode (vertical polarization). The power density is obtained summing the two components:

$$\frac{\mathrm{d}^2 \mathcal{P}}{\mathrm{d}\omega \, \mathrm{d}\Omega} = f_{\mathrm{rev}} \frac{\mathrm{d}^2 I}{\mathrm{d}\omega \, \mathrm{d}\Omega} \approx \frac{c}{2\pi\rho} 2\varepsilon_0 r'^2 \left(\left| \tilde{E}_x(\omega) \right|^2 + \left| \tilde{E}_y(\omega) \right|^2 \right) \tag{2.57}$$

$$= \frac{q^2}{24\pi^4 \varepsilon_0 c^3} \rho\omega^2 \left(\frac{1}{\gamma^2} + \theta^2 \right)^2 \left[K_{2/3}^2(\xi) + \frac{\theta^2}{1/\gamma^2 + \theta^2} K_{1/3}^2(\xi) \right]. \tag{2.58}$$

The angular spread, θ_c, is defined from eq. 2.55, by requiring $\xi(\theta_c) = \xi(0) + 1$; one gets:

$$\theta_c = \frac{1}{\gamma} \sqrt{\left(1 + \frac{2\omega_c}{\omega} \right)^{2/3} - 1}, \tag{2.59}$$

which not only shows that most of the radiation is contained in a cone of aperture $1/\gamma$ (as already obtained in eq. 2.48), but also that the low frequencies have higher angular aperture.

As a final step eq. 2.58 needs to be integrated over the solid angle to obtain the power density:

$$\frac{\mathrm{d}\mathcal{P}}{\mathrm{d}\vartheta} = \frac{9\sqrt{3}}{8\pi} P_\gamma \vartheta \int_\vartheta^{+\infty} K_{5/3}(x)\,\mathrm{d}x; \qquad \vartheta = \frac{\omega}{\omega_c} \tag{2.60}$$

$$= P_\gamma S(\vartheta). \tag{2.61}$$

The shape of the spectrum is characterized by the S function (shown in Fig. 2.11) while its magnitude depends on P_γ (see eq. 2.49).
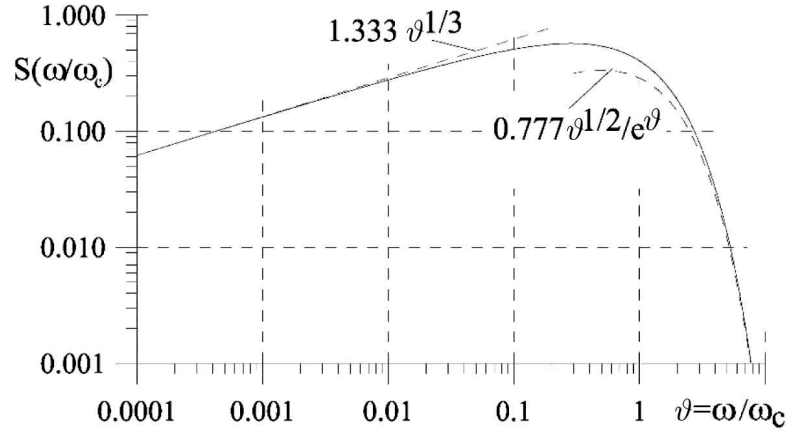
Figure 2.11: The S function: $S(\vartheta) = \dfrac{9\sqrt{3}}{8\pi} \vartheta \int_\vartheta^{+\infty} K_{5/3}(x)\,\mathrm{d}x$; with: $\vartheta = \dfrac{\omega}{\omega_c}$.

2.3.5 Quantum excitation

Calling P_0 the reference momentum, the motion of the particle is described with canonical variables x, $p_x = P_x/P_0$, while δ identifies the momentum deviation normalised to P_0. The action of a particle is written as:

$$2J_x = \gamma_x x^2 + 2\alpha_x x p_x + \beta_x p_x^2, \tag{2.62}$$

where α, γ and β are the Twiss parameters. The subscript x is kept to diversify them with respect to the relativistic parameters, although the same derivation applies to the vertical direction as well.

After the emission of radiation, carrying some momentum dP, the coordinates are changed as

29

follows[2]:

$$\delta \to \delta - \frac{dP}{P_0}; \tag{2.63}$$

$$x \to x + \eta_x \frac{dP}{P_0}; \tag{2.64}$$

$$p_x \to p_x \left(1 - \frac{dP}{P_0}\right) + \eta_{px} \frac{dP}{P_0}. \tag{2.65}$$

This leads to a variation of the action:

$$J_x \to J_x + dJ_x, \tag{2.66}$$

with:

$$dJ_x = -w_1 \frac{dP}{P_0} + w_2 \left(\frac{dP}{P_0}\right)^2, \tag{2.67}$$

where, in the limit of $\delta \to 0$ [3]:

$$w_1 = \alpha_x x p_x + \beta_x p_x^2 - \eta_x (\gamma_x x + \alpha_x p_x) - \eta_{px}(\alpha_x x + \beta_x p_x); \tag{2.68}$$

$$w_2 = \frac{1}{2}\left(\gamma_x \eta_x^2 + 2\alpha_x \eta_x \eta_{px} + \beta_x \eta_{px}^2\right) - \left(\alpha_x \eta_x + \beta_x \eta_{px}\right)p_x + \frac{1}{2}\beta_x p_x^2. \tag{2.69}$$

Equation 2.67 contains two terms. The first reduces the action and comes from the fact that the cavities maintain the energy close to the design one contributing only to the longitudinal momentum, while the particles lose momentum parallel to their motion, therefore also in the transverse direction. The second term is an excitation that comes from the fact that when a particle changes its energy: although its position does not change, its reference orbit is now a dispersive one. The bigger the dispersion function is where the particle emits, the bigger the residual displacement will be where the dispersion is suppressed.

In a classical framework one can assume that, in the limit $dt \to 0$, also $dP \to 0$. However it is known that the emission of the radiation is quantized, therefore the equation of motion for the action in eq. 2.67 have to be written as:

$$\frac{dJ_x}{dt} = -\frac{w_1}{P_0 c} \int_0^{+\infty} \dot{N}(u) u \, du + \frac{w_2}{P_0^2 c^2} \int_0^{+\infty} \dot{N}(u) u^2 \, du, \tag{2.70}$$

where $\dot{N}(u)\,du$ is the number of photons emitted per unit time in the energy range from u to $u + du$. The number of photon must also be equal to the power emitted, divided by the energy

---

[2]The dispersion functions are introduced here: $\eta_x = \left.\frac{dx}{d\delta}\right|_{\delta=0}$; $\eta_{px} = \left.\frac{dp_x}{d\delta}\right|_{\delta=0}$.

[3]The approximation is good in a ring, where the cavities restore the energy lost keeping the momentum around the design one. This limit also means that chromatic effects of the lattice are neglected.

of a single photon: $u = \hbar\omega$; therefore:

$$\dot{N}(u)\,\mathrm{d}u = \frac{\frac{\mathrm{d}\mathscr{P}}{\mathrm{d}\vartheta}\,\mathrm{d}\vartheta}{\hbar\omega}. \tag{2.71}$$

Using the expression for $\mathrm{d}\mathscr{P}/\mathrm{d}\vartheta$ that was obtained for a dipole magnet (see eq. 2.60) one finds:

$$\int_0^{+\infty} \dot{N}(u)\,u\,\mathrm{d}u = P_\gamma; \tag{2.72}$$

$$\int_0^{+\infty} \dot{N}(u)\,u^2\,\mathrm{d}u = 2C_q\gamma^2\frac{E_0}{\rho}P_\gamma; \qquad C_q = \frac{55}{32\sqrt{3}}\frac{\hbar}{mc} \tag{2.73}$$

where the constant C_q has been introduced; for electrons it value is 3.832 m.

The total rate of emission is obtained integrating the flux over all the energies:

$$\mathscr{N} = \int_0^{+\infty} \dot{N}(u)\,\mathrm{d}u = \frac{15\sqrt{3}}{8}\frac{P_\gamma}{u_c}; \qquad u_c = \hbar\omega_c = \frac{3}{2}\frac{\hbar c}{\rho}\gamma^3. \tag{2.74}$$

It is interesting to note how the flux emitted over a certain angle θ, only depends on γ:

$$\frac{\mathscr{N}}{\theta} = \frac{5\alpha}{2\sqrt{3}}\gamma, \tag{2.75}$$

where α is the electromagnetic constant. The mean free path between the emission of two photons is computed as:

$$\langle\lambda\rangle = \frac{L}{\mathscr{N}} = \frac{\theta\rho}{\mathscr{N}} = \frac{2\sqrt{3}}{5\alpha}\frac{\rho}{\gamma}. \tag{2.76}$$

The actual free path is a random variable which follows a Poisson distribution with parameter $\langle\lambda\rangle$.

Simulation of radiation in a tracking code

The expressions for the free path and for the photon energy spectrum, complete the requirements to simulate the emission of incoherent radiation in a tracking code with a Montecarlo approach. Initially a free path is computed for all the particles in a bunch. When a particle travels a distance equal to its free path, a photon energy is randomly extracted from the spectral distribution. In codes that adopt the coordinate set: $\{x, x', y, y', z, E\}$, the energy of the particle is reduced by the photon energy. Codes that use $\{x, p_x, y, p_y, z, P\}$ require also to modify the transverse momenta. Finally a new free path is calculated.

2.3.6 Equilibrium emittance in a ring

By substituting in eq. 2.70 the expression of w_1 (2.68), w_2 (2.69), the integrals (2.72) (2.73) and averaging over the ring circumference, one finds the evolution of the action (for $x \ll \eta_x$ and $p_x \ll \eta_{px}$):

$$\frac{\mathrm{d}\varepsilon_x}{\mathrm{d}t} = -\frac{2}{\tau_x}\varepsilon_x + \frac{2}{j_x\tau_x}C_q\gamma^2\frac{I_5}{I_2}, \tag{2.77}$$

where we introduced the damping time $\tau_x = \dfrac{2}{j_x}\dfrac{E_0}{U_0}T_0$ and the damping partition number $j_x = 1 - \dfrac{I_2}{I_4}$.

The integrals I_4 and I_5 are given by:

$$I_4 = \int \frac{\eta}{\rho}\left(\frac{1}{\rho^2} + 2k_1\right)\mathrm{d}s, \tag{2.78}$$

where the quantity $k_1 = \dfrac{q}{P_0}\dfrac{\partial B_y}{\partial x}$ is the normalized quadrupolar component eventually present in the bending magnets;

$$I_5 = \int \frac{\mathcal{H}_x}{|\rho^3|}\mathrm{d}s. \tag{2.79}$$

$\mathcal{H}$ is the dispersion invariant:

$$\mathcal{H}_x = \gamma_x\eta_x^2 + 2\alpha_x\eta_x\eta_{px} + \beta_x\eta_{px}^2. \tag{2.80}$$

By setting the time derivative to zero in eq. 2.77, one obtains the equilibrium geometrical emittance:

$$\varepsilon_0 = C_q\gamma^2\frac{I_5}{jI_2}. \tag{2.81}$$

In the vertical plane, where ideally there is no dispersion and therefore $\mathcal{H}_y = 0$, the limit to the emittance is given by the aperture of the radiation cone:

$$\varepsilon_y = \frac{13}{55}\frac{C_q}{j_yI_2}\int \frac{\beta_y}{|\rho^3|}\mathrm{d}s. \tag{2.82}$$

The result for the longitudinal plane is cited for completeness:

$$\sigma_{\delta 0}^2 = C_q\gamma^2\frac{I_3}{jI_2}; \qquad I_3 = \int \frac{1}{|\rho^3|}\mathrm{d}s. \tag{2.83}$$

These formulae are the starting point for the estimations of the performances of a ring. They are indeed of critical importance for the comparison of the Linac Ring and the Ring Ring design of the LHeC.

2.3.7   Emittance growth in a transfer line

In a transfer line, without any cavity restoring the central energy, there is no damping. As the beam moves along the line momentum spread and emittance growth are introduced by quantum excitation. In eq. 2.67 and eq. 2.70, the damping term is dropped, keeping only the exciting one.

Rewriting:

$$\mathcal{N}\langle u^2\rangle = \int_0^{+\infty} \dot{N}(u)\,u^2\,\mathrm{d}u = 2C_q\gamma^2\frac{E_0}{\rho}P_\gamma = \frac{55\alpha c(\hbar c)^2}{24\sqrt{3}}\frac{\gamma^7}{|\rho^3|}, \tag{2.84}$$

the quantum excitation of the beam along a path of length L becomes:

$$\Delta\sigma_E^2 = \frac{55\alpha(\hbar c)^2}{48\sqrt{3}}\gamma^7\int_0^L \frac{1}{|\rho^3|}\,\mathrm{d}s. \tag{2.85}$$

By integrating the action (2.70) the dilution of geometrical emittance is obtained, as reported in [18]:

$$\Delta\varepsilon = \frac{55r_c\hbar c}{24\sqrt{3}mc^2}\gamma^5\int_0^L \frac{\mathcal{H}}{|\rho^3|}\,\mathrm{d}s. \tag{2.86}$$

When applying this formula one should keep in mind that the possible betatron mismatch introduced by synchrotron radiation is not taken into account; therefore the emittance growth may be underestimated.

2.4   Coherent Synchrotron Radiation

The generic electric field given by Liénard-Wiechert (see eq. 2.39 and eq. 2.41) depends linearly on the value of the charge. Therefore, when computing the emitted power, one obtains a quadratic dependency on the charge. However, if there are N_b charges, this is only true if they all behave like a single charge, meaning that the fields that they produce are in phase and sum in a constructive way. This typically happens when the emitted radiation has a wavelength comparable to the size of the charge distribution, therefore it emits *coherently* and the emitted power scales with N_b^2. At much shorter wavelengths each charge behaves independently, therefore one only gets a factor N_b in the power and we speak about *incoherent* radiation [46].

The Coherent Synchrotron Radiation (CSR) has become an issue that modern particle accelerators, aiming at short and intense bunches, need to consider. In the context of the LHeC, with

beams at very high energy, the coherent part of the radiation spectrum is masked by the much stronger incoherent part. However for lower energy facilities like the CLIC recombination complex, the CSR may pose lower limits to the bunch length, in conflict with the one required to avoid too much curvature from the RF. Although a full implementation of the CSR is not yet available in PLACET2, in the next sections we explore some of the fundamental aspects which allow for analytical estimations.

2.4.1 Coherently emitted power

To approach the calculation of the power, one can write the total electric field emitted by a set of N_b aligned charges each having a particular delay τ_k with respect to the reference time t:

$$\boldsymbol{E}_N(t) = \sum_{k=1}^{N_b} \boldsymbol{E}(t - \tau_k);$$ (2.87)

and its Fourier transform is:

$$\tilde{\boldsymbol{E}}_N(\omega) = \sum_{k=1}^{N_b} e^{i\omega\tau_k} \tilde{\boldsymbol{E}}(\omega).$$ (2.88)

One should now proceed taking the same steps described in Sec. 2.3.4. However, since the math is now more involved, we skip the intermediate steps; for the full derivation please refer to [42]. For a gaussian distribution of the charges in time, one obtains the power spectrum:

$$\frac{d\mathcal{P}_{csr}}{d\omega} = 1.333 \left(\frac{\omega}{\omega_c}\right)^{1/3} \frac{P_\gamma}{\omega_c} N_b^2 \exp\left(-\omega\sigma_t\right),$$ (2.89)

where the low frequency approximation of the S function, as shown in Fig. 2.11, have been used. This is allowed by the fact that the high frequency component of the power spectrum is suppressed by the exponential term.

By integration of eq. 2.89 one obtains the total power radiated coherently:

$$P_{csr} = 1.333 \frac{\Gamma(2/3)}{2(\omega_c\sigma_t)^{4/3}} P_\gamma N_b^2 = 0.0279 \frac{e^2 c}{\varepsilon_0} \frac{N_b^2}{\rho^{2/3}\sigma_z^{4/3}}.$$ (2.90)

It is interesting to note how the energy dependence in P_γ cancels with the one in ω_c, and the final result does not depend on the beam energy.

For long bunches a transition point is reached around $\sigma_t = N_b^{3/4}/\omega_c$. Substituting this value in eq. 2.90 a linear dependency on N_b is attained. Beyond that, the radiation becomes incoherent and the power goes with:

$$P_i = N_b P_\gamma.$$ (2.91)

For bunch lengths shorter than half of the critical wavelength the whole bunch radiates as a single particle and the emission of power saturates at the fully coherent value:

$$P_f = N_b^2 P_\gamma. \tag{2.92}$$

It should be noted, however, that the metal wall of the beam pipe, can have a shielding effect. Indeed spectral components below the physical aperture of the pipe, cannot propagate within it and are suppressed, mitigating the effect of radiation.

2.4.2 Impact on the Beam Dynamics

In the previous section the general expressions for the power spectrum and the total power lost by coherent synchrotron radiation were derived starting from the sum of the fields produced by many particles. No consideration about how these fields may affect the particles themselves was given.

It turns out that the radiation emitted coherently can be so intense that it actually affects the bunch. This follows from the fact that, while the bunch travels on a bent trajectory, the radiation goes along the chord and *overtakes* it. The propagation of the radiation field along the bunch allows the head of the bunch to collect some of the energy emitted by the tail, therefore we speak of *tail-head* effect.

Comparing the overtaking-radiation fields to the wakefields described in Sec. 2.1.1, one notes a striking similarity. In both cases the bunch travels across its self fields and this introduces energy variations along the bunch. The case of the CSR is pretty unique in the fact that the wake propagates in the forward direction, therefore the causality of the wake function is reversed. When computing the wake functions some complications arise handling the cases where part of the bunch is in the magnet, while part has still to enter or has already exited. All these cases are described in [47] and [48]. The wake may also propagate from one magnet to the next one, as discussed in [49].

Here we report the approximation for the steady-state[4] wake function valid for $\rho/\gamma^2 \ll z \ll \rho$ [18]:

$$W_{//}(z) = -\frac{Z_0 c}{2\pi} \frac{1}{3^{4/3} \rho^{2/3} z^{4/3}}. \tag{2.93}$$

The minus sign indicates that a test particle gains energy from the wake. This is shown in Fig. 2.12, where a long negative tail is visible in the wake function plot, resulting in the energy gain that affects the head of the distribution.

A formula for fast estimations of the energy spread induced by CSR for a gaussian longitudinal

---

[4]In the CSR context steady-state means that all the bunch is inside the magnet and that the radiation emitted while entering the magnet is now far ahead.
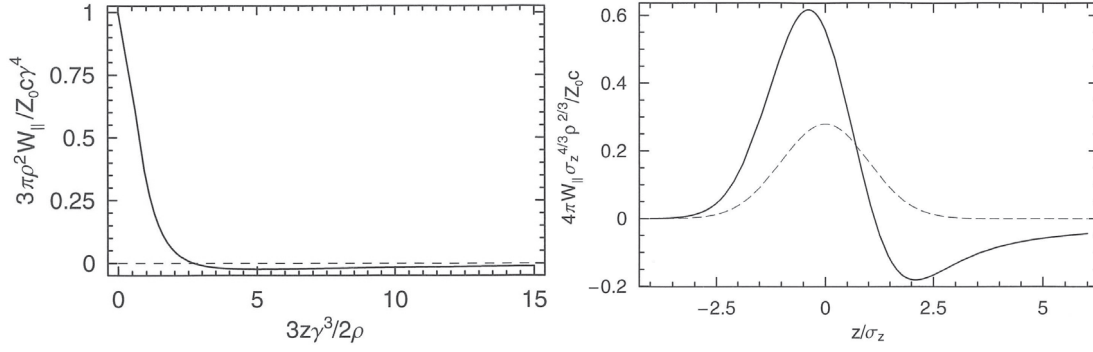
Figure 2.12: Left: normalized wake function leading a charged particle. Right: total wake (solid line) obtained by convolution with a gaussian distribution (dashed line); the head of the bunch correspond to $z > 0$.

charge distribution is derived in [50]:

$$\delta \approx 0.22 \, \frac{N_b r_0 L_d}{\gamma (\rho \sigma_z^2)^{2/3}}, \tag{2.94}$$

where L_d is the dipole length.

The growth of transverse emittance can be calculated as [51]:

$$\frac{\varepsilon}{\varepsilon_0} \approx \sqrt{1 + \frac{0.22^2}{36} \frac{r_0^2 N_b^2}{\gamma^2 \varepsilon_0 \beta} \left(\frac{|\theta|^5 L_d}{\sigma_z^4} \right)^{2/3} \left[L_d^2 \left(1 + \alpha^2 \right) + 9\beta^2 + 6\alpha\beta L_d \right]}. \tag{2.95}$$

2.5 Beam-Beam

The Beam-Beam effect consists in the interaction of two counter-propagating beams. Weather the beams are brought into collision (head-on beam-beam) or are separated by few sigmas (long-range beam-beam), they are subjected to strong non-linear forces originating from their self fields. The beam-beam effect shares many of the parametric dependencies with the luminosity, therefore it is often one of the limiting effects of the performances of a collider.

The amount of beam-beam effect that can be tolerated strongly depends on the type of the machine. The more sensitive machines are the hadron colliders, where the non-linearity leads to emittance blowup and amplitude dependent tune shift that can drive particles into resonances. The e^+e^- circular colliders accept stronger beam-beam as the radiation preserves the beam sizes. In linear colliders, where after the collision the beams are discarded, the beam-beam is pushed much harder, the practical limits coming from the more rapid loss of luminosity from non perfectly aligned beams.

Not always the two beams are symmetric. In these cases one typically identifies a "strong"

beam, which is less perturbed, and a "weak" beam, which is more disrupted. In the case of LHeC, the electron beam (being at a much lower energy) is the weak one. It should also be noted that if the two beams have opposite charges, they attract each other, this takes the name of pinch and results in an enhancement of the luminosity.

2.5.1 Mathematical approach

A general receipt to evaluate the kick that a particle receives when crossing the other beam, consists in the following steps. Initially the potential generated by the charge distribution of the beam, needs to be evaluated; this is done solving the Poisson equation:

$$\nabla^2 U = -\frac{1}{\varepsilon_0}\rho(x, y, z), \tag{2.96}$$

eventually by the method of the Green function. The field is then simply the derivative of the potential:

$$\vec{E} = -\vec{\nabla} U. \tag{2.97}$$

By means of a Lorentz boost the field is transformed into the reference frame of the other beam. The Lorentz force can then be written:

$$\vec{F} = q(\vec{E} + \vec{v} \times \vec{B}), \tag{2.98}$$

and from that the transverse kick:

$$\Delta r' = \frac{1}{mc\beta\gamma} \int_{-\Delta t/2}^{\Delta t/2} F_r(r, s, t)\, dt. \tag{2.99}$$

2.5.2 Solution for round gaussian beams

For a 3D Gaussian charge distribution:

$$\rho(x, y, z) = \frac{Nq}{(2\pi)^{3/2}\sigma_x\sigma_y\sigma_z} \exp\left(-\frac{x^2}{2\sigma_x^2} - \frac{y^2}{2\sigma_y^2} - \frac{z^2}{2\sigma_z^2}\right), \tag{2.100}$$

all the described steps can be applied analytically. The radial force takes the form (additional intermediate steps can be found in [52]):

$$F_r(r, s, t) = \pm\frac{Nq^2(1+\beta^2)}{2\pi\varepsilon_0 r}\left[1 - \exp\left(-\frac{r^2}{2\sigma^2}\right)\right]\left[\exp\left(-\frac{(s+vt)^2}{2\sigma_s^2}\right)\right], \tag{2.101}$$

and consequently the kick is:

$$\Delta\{x, y\}' = \pm \frac{2Nr_e}{\gamma} \frac{\{x, y\}}{r^2} \left[1 - \exp\left(-\frac{r^2}{2\sigma^2}\right) \right].$$

(2.102)
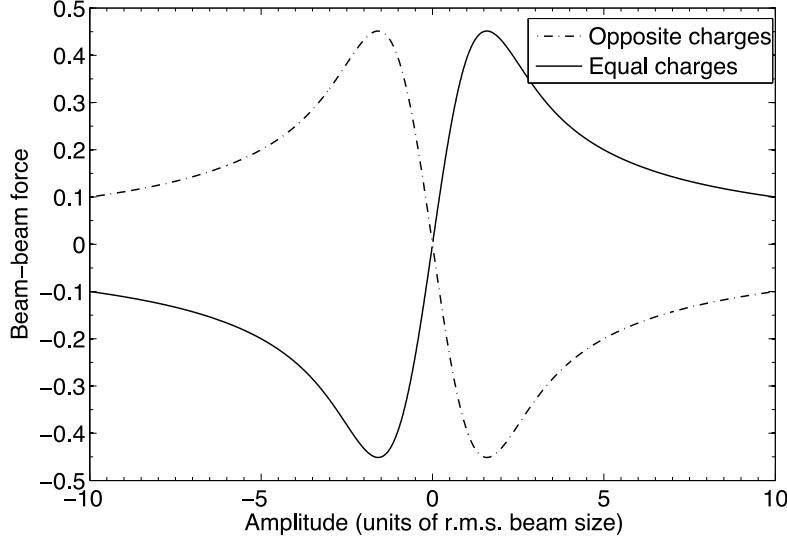
Figure 2.13: The beam-beam force a round gaussian beam. The horizontal axis represents the separation of a test particle with respect to the core of the other beam, while vertical axis is in arbitrary units.

The intensity of the beam-beam force is plotted in Fig. 2.13. One can note that the force is almost linear close to the centre, while at larger separation it smears out, decaying at infinity with $1/\sigma$.

It is important to note that the obtained results follow from the assumption of a smooth gaussian charge distribution. In reality the distribution may be far from gaussian and the smoothness assumption is broken by the granularity of the beam. Particles in the two beams may come close to each other and diffusion processes take place. This is illustrated in Fig. 2.14 where a smooth quadrupole lens is compared to a beam lens. Such scattering processes contribute to the formation of a halo that in a hadron ring needs to be removed in dedicated collimation sections. These advanced aspects are typically assessed with computer simulations and are central issues in today's beam dynamics studies.

2.5.3 Beam-beam disruption parameter, tune shift and limit

The beam-beam disruption parameter is defined as the ratio between the bunch length and its focal length [53]. It quantifies the strength of the beam-beam interaction:

$$D_{\{x,y\}} = \frac{\sigma_z}{f_{\{x,y\}}} = \frac{2Nr_e\sigma_z}{\gamma\sigma_{\{x,y\}}(\sigma_x + \sigma_y)}.$$

(2.103)
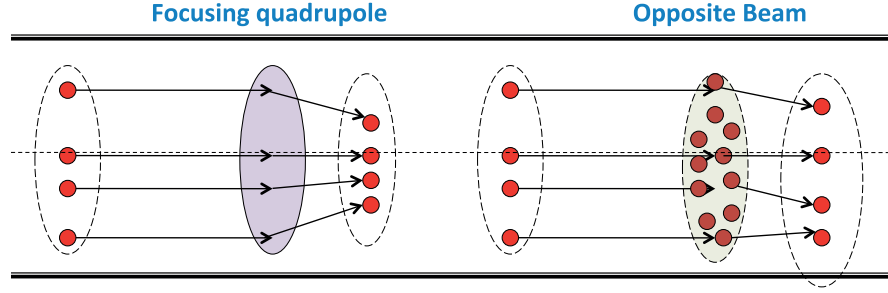
Figure 2.14: As opposed to an ideal lens, the granularity of the other beam leads to scattering and diffusion.

For $D \ll 1$ the particles do not move much in the field of the other beam and the analytical calculations performed in the previous section are good approximations. $D \gg 1$ means that the particles perform oscillations around the other beam and the integration of the force done in eq. 2.99 is no longer valid, as one needs to take into account the varying position of the particle and thus the variable force. In the case of LHeC, the electron disruption parameter is ≈ 6 and indeed the electrons complete more than one full oscillation around the proton beam. The analytic computation overestimates the kick.

For small enough disruption parameters, such as the ones are found at circular colliders, the characterization of the beam-beam strength is typically done taking the derivative of the force at the origin. This gives the *beam-beam parameter* or *tune shift*:

$$\xi_{\{x,y\}} = \frac{N r_e \beta^*_{x,y}}{2\pi\gamma\sigma_{\{x,y\}}(\sigma_x + \sigma_y)}. \tag{2.104}$$

It is interesting to compare eq. 2.103 and eq. 2.104 with the formula for the luminosity:

$$\mathcal{L} = H_D \frac{N^2 n_b f}{4\pi\sigma_x \sigma_y}, \tag{2.105}$$

where H_D is an enhancement factor that collects effects like the hourglass and the pinch, n_b is the number of bunches in a train and f is the repetition frequency (linac) or revolution frequency (ring). One sees that for flat beams ($\varepsilon_x \gg \varepsilon_y$), like the ones that are naturally obtained in presence of strong synchrotron radiation, there is some margin to increase the luminosity maintaining acceptable tune shifts, for instance with $\beta^*_y < \beta^*_x$. Another advantage of flat beams, especially in the extreme case of linear colliders, is the reduction of the photon production which is inverse proportional to the bigger of the beam sizes.

At circular e^+e^- colliders the beam-beam can manifest itself changing the luminosity dependency from N^2 to N. This is known as *beam-beam limit* and is a direct consequence of the increase of vertical emittance. Indeed pushing the bunch intensity, one observes a saturation of the vertical beam-beam parameter, meaning that N/σ_y has to stay constant. Consequently,

rewriting the luminosity as:

$$\mathcal{L} = \frac{n_b f}{4\pi\sigma_x} \frac{N}{\sigma_y} N, \tag{2.106}$$

it can be noted that the dependency on N is now linear.

2.5.4 Beamstrahlung

The beamstrahlung consists in the emission of radiation by particles bent in the field of the opposite beam. The most severe beamstrahlung is encountered with the nano-sized beams of linear colliders. It causes a degradation of the luminosity spectrum, with a number of collisions that take place at lower energies. Moreover the emitted photons may dissipate a consistent amount of power into the walls of the interaction region, generating additional background into the detector.

The description of beamstrahlung is attained through the *beamstrahlung parameter*, which measures the field strength in the rest frame of the particle and can be written as [18]:

$$\Upsilon \approx \frac{5}{6} \frac{r_e^2 \gamma N_b}{\alpha \sigma_z (\sigma_x + \sigma_y)}, \tag{2.107}$$

where γ is the relativistic parameter of the emitting particle, while all the other quantities are related to the opposite beam.

Comparing eq. 2.105 with eq. 2.107 one can note that flat beams ($\sigma_y \ll \sigma_x$) allow to increase the luminosity while containing the beamstrahlung. At the LHeC the spot shape is round to match the proton beam, however the sizes are relatively large compared to what found in circular and linear $e^+ e^-$ colliders, therefore this effect is not particularly strong.

The average number of photons emitted by an electron crossing the proton beam is estimated as [18]:

$$n_\gamma \approx 2.54 \left[\frac{\alpha^2 \sigma_z}{r_e \gamma} \Upsilon \right] U_0(\Upsilon), \tag{2.108}$$

$$U_0(\Upsilon) \approx \frac{1}{(1 + \Upsilon^{2/3})^{1/2}}. \tag{2.109}$$

The average photon energy is [18]:

$$E_\gamma = \frac{4\sqrt{3}}{15} \Upsilon \frac{U_1(\Upsilon)}{U_0(\Upsilon)}, \tag{2.110}$$

$$U_1(\Upsilon) \approx \frac{1}{(1 + (1.5\Upsilon)^{2/3})^2}. \tag{2.111}$$

Finally the total emitted power is written as:

$$P = N_b n_\gamma E_\gamma f, \tag{2.112}$$

where f is the collision repetition rate.

For the nominal LHeC parameters (collected in Tab. 3.2, in Chapter 3) one obtains $n_\gamma \approx 0.5$, $E_\gamma \approx 0.4$ MeV. The beamstrahlung at the LHeC is an order of magnitude weaker than the radiation emitted into the detector integrated dipoles which provide head-on collisions [1]. Its impact needs to be taken into account for the technical design of the interaction region in terms of shielding and background, but is not particularly relevant for the beam dynamics.

2.5.5 Long range interactions

The encounters between two beams at large separations are called long range interactions. These kind of encounters take place, for instance, before and after an interaction point, where the two beams still share the same pipe. The long range interaction creates orbit distortion and additional tune spread, which particularly affects the particles at large amplitudes which, in many repeated crossings, can appear closer to the other beam.

It is interesting to note that the long range beam-beam force goes with $1/r$ (see Fig. 2.13) which correspond to the same field generated by a wire transporting an electric current. Therefore wire compensating systems are currently under study. A perfect compensation of the long range interaction will never be possible in a ring, unless the bunches are evenly spaced. If gaps are present in the bunch train (for instance for injection/extraction or ion/electron cloud cleaning) then the bunches coming before or after a gap, will miss some of the long range interactions. These bunches, called pacman bunches, require a different compensation compared to the ones in the centre of the batches, therefore an average setting is required.

At the LHC, with a bunch spacing of 25 ns one finds a parasitic interaction every 3.75 m. However parasitic encounters are not expected at the LHeC, where the electron beam is bent to achieve head on collisions by means of a detector-integrated dipoles. At the first parasitic encounter the two beams are already separated by $\sim 36\,\sigma_p$ [1]. The most delicate case in the LHeC is the off centre collision, which can establish a coherent motion of the beams. A feed forward system has been planned to stabilize the electron beam, while simulations of the proton beam showed a tolerable effect [54].

3 LHeC

3.1 Introduction

The LHeC study is a possible upgrade of the LHC that aims at delivering an electron beam for collisions with the existing hadronic beams, while the major LHC experiments, CMS and Atlas, pursue their physics programs. In the following sections we will discuss the possible options for the electron facility and investigate the beam dynamics of the energy recovery linac (ERL) design. The improvements in the design following the first end-to-end tracking will be presented. The multi-bunch tracking, including long-range wakefields in the multi-turn ERL will be covered. Finally the results of the studies performed for PERLE will be described.

3.1.1 Layout Considerations: Linac vs Ring

Studies performed by the High Energy Physics community shows that an electron beam energy of 60 GeV together with a luminosity of $1 \times 10^{34}\,\mathrm{cm}^{-2}\mathrm{s}^{-1}$ allows the ultimate application of the LHeC as a Higgs factory. These should be delivered with a realistic power budget within 100 MW.

It should be noted that such beam energy has already been exceeded during the LEP era, when, in the same tunnel now being used by the LHC, electron and positron beams of 104.5 GeV were ultimately achieved. Therefore a natural option would consist in fitting a new lepton ring in the existing LHC tunnel. Such machine allows to meet the key beam parameters with no major challenges except for the ones arising from the integration into the LHC site. Indeed such an implementation would require km long bypasses that have to be dug around the existing experimental caverns, and sections of the LHC, such as the RF and the dump kickers, need important interventions to accommodate the additional ring. Although part of the construction could be scheduled while operating the LHC, the installation would require at least several years of shutdown of the LHC.

An alternative design approach to the electron facility aims at an installation in a dedicated

tunnel, completely decoupled from the LHC with the only exception of the Interaction Region. Linac designs can be adapted from linear collider studies and fitted in few kilometres straight tunnel, however a linac would not be capable of delivering a significant number of Higgs events within the given power consumption budget of 100 MW. While linear colliders achieve high luminosity by taking advantages of small emittance and strong focussing of the flat leptonic beams, this path is excluded at the LHeC due to the round hadronic beam. The only alternative for boosting the luminosity at the LHeC is therefore to increase the average electron current.

High currents and, consequently, the luminosity goal, can be achieved with a linac adopting the energy recovery scheme in which the spent electron beam is decelerated in order to extract its energy and reuse it to accelerate a fresh beam. Although exotic schemes based on multiple beams have been envisioned, at the LHeC this is realized by bending the beam to re-injecting it into the linac on the decelerating phase.

From the beam dynamics point of view the main advantage of the ERL over a ring is that it allows to deliver a smaller emittance beam and to exploit it with a stronger beam-beam effect that would not be tolerable in a ring. Table 3.1 summarises a possible sets of parameters for collisions with the ultimate HL-LHC beam, a more conservative set is found in [54]. The computation of the luminosity does not take into account the hourglass effect and the pinch enhancement factor. It can be noted that with the linac, with no restriction on the electron tune shift, one can reach a higher luminosity even with a smaller beam current values, as compared to a ring-ring option where the tune shifts would probably already be unbearable.

Table 3.1: Summary of a possible set of ultimate parameters and performances of the LR and RR LHeC coupled with the HL-LHC beam

	ERL		27 km Ring	
	p	e^-	p	e^-
Beam Energy [GeV]	7000	60	7000	60
Bunch Spacing [ns]	25	25	25	25
Bunch Intensity (nucleons) [1×10^{10}]	17	0.4	17	2
Beam Current [mA]	1110	25	1110	100
RMS Bunch Length [mm]	75.5	0.6	75.5	6
Normalized RMS Emittance [μm]	2.5	50	2.5	$590_x/290_y$
IP Beta Function $\beta^*_{x/y}$ [m]	0.05	0.039	0.06	$0.04_x/0.08_y$
IP spot size [μm]	4.1	4.1	14.1	$14.2_x/12.2_y$
Beam-Beam tune shift	0.0002	0.76	0.00098	$0.065_x/0.097_y$
Luminosity [1×10^{33} cm^{-2} s^{-1}]	6.5		2.9	

Comparing the ERL with a similarly sized 9 km ring, we get even more striking results. Indeed such a ring would radiate three times more than the 27 km option. This results in a lower current to fit within the power constraints, but also in bigger emittances that would lead to a luminosity approximately a factor 10 lower.

In conclusion, although the ERL is based on a much less consolidated technology, it allows to deliver a higher luminosity compared to a ring. This is especially true if the two of them are similarly sized. Considering the technical difficulties of the integration of an electron ring into the LHC tunnel, the ERL has therefore been chosen as the baseline design for the LHeC.

In the next sections we will investigate the details of the ERL design (including extensions and refinements) and the performance studies performed by means of end-to-end and multi-bunch tracking simulations.

3.2 ERL Design

The ERL design for the LHeC electron facility is sketched in Fig. 3.1. The racetrack layout hosts two superconducting linacs on the straight sections and three recirculating arcs on each side. Its total length is 9 km: 1/3 of the LHC circumference. An integer fraction is required to guarantee that, in presence of an ion-cleaning gap in the electron beam, the proton bunches collide with electrons either always or never.

Each of the two linacs is about 1 km long and provides a total acceleration of 10 GeV. The injection energy has been chosen to be 500 MeV. In order to reach the collision energy of 60 GeV, the electrons are recirculated three times. Beams of different energies are directed into the corresponding recirculation arcs via beam spreaders/recombiners which introduce/remove vertical separation at each end of the linacs. Arc2 and Arc4 are equipped with bypasses that provide separation from the the detector.
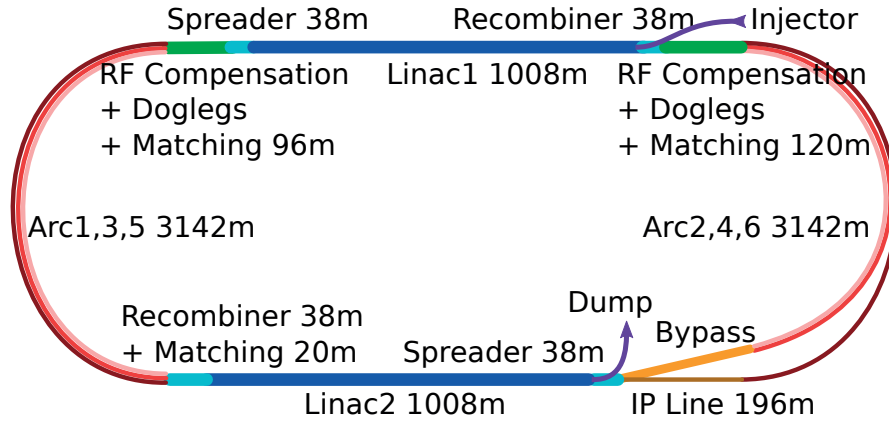
Figure 3.1: Scheme of the LHeC ERL-based electron facility

After the collision with the LHC proton or ion beam, the electron beam is delayed by half of the RF period and re-injected into the same linacs to be decelerated in three subsequent turns. Its energy is released into the RF and used to accelerate the fresh beam. This allows one to increase the beam current and luminosity while limiting the RF power consumption [1]. The beam parameters have recently been revised to reach a luminosity $> 1 \times 10^{34} \, \text{cm}^{-2} \, \text{s}^{-1}$, they are presented in Table 3.2. Such a high luminosity, 250 times the one previously achieved at

HERA [55], allows one to employ the LHeC as a Higgs Factory [56].

The number of recirculating turns follows from a cost estimation. The key effect is synchrotron radiation which leads to a scaling of the arc length with E^4 while the linac length scales with E. On the other hand the linac cost per meter is much higher than the one of the arc. For these reasons, aiming at a lower energy, one obtains smaller arcs and can save on the linac cost adding more recirculating turns, while at higher energies is better to reduce the number of turns increasing the length of the linac.

The operation of the ERL foresees continuous injection of bunches every 25 ns, matching the LHC beam. During the stable operation of the machine, bunches at all the possible turns coexist in the racetrack, leading to a six times higher beam current in the SRF cavities as the beam current at the Interaction Point. The bunches in the linacs appear in particular patterns depending on the lengths of the arcs, giving specific times of flight. Gaps in the electron train can be inserted to match the LHC filling pattern and to allow for ion cleaning [1].

Table 3.2: Fundamental Beam Parameters of the Baseline and Higgs Factory ERL.

	Baseline		Higgs Factory	
	e^-	p	e^-	p
Beam Energy [GeV]	60	7000	60	7000
Bunch Spacing [ns]	25 (50)	25 (50)	25 (50)	25 (50)
Bunch Intensity (nucleons) [1×10^{10}]	0.1 (0.2)	17	0.4 (0.8)	22 (35)
Beam Current [mA]	6.4	860	25.6	1110 (883)
RMS Bunch Length [mm]	0.6	75.5	0.6	75.5
Normalized RMS Emittance [μm]	50	3.75	50	2.5 (3.0)
IP Beta Function $\beta_{x,y}^*$ [m]	0.12	0.1	0.039	0.05
IP spot size [μm]	7.2	7.2	4.1	4.1
Hadron Beam-Beam Parameter	0.5×10^{-4} (1×10^{-4})		2×10^{-4} (4×10^{-4})	
Lepton Disruption Parameter D	6		23 (31)	
Crossing Angle	0		0	
Hourglass Reduction Factor	0.91		0.70 (0.73)	
Pinch Enhancement Factor	1.35		1.35	
CM Energy [GeV]	1300		1300	
Luminosity [1×10^{33} cm^{-2} s^{-1}]	1.3		16 (22)	

3.2.1 Linacs design, optics and optimisation

The two linacs are about 1 km long and they consist of 18 FODO cells. Following each quadrupole, two cryomodules are placed, each containing 8 cavities operating at 802 MHz, for a total of 576 cavities per linac.
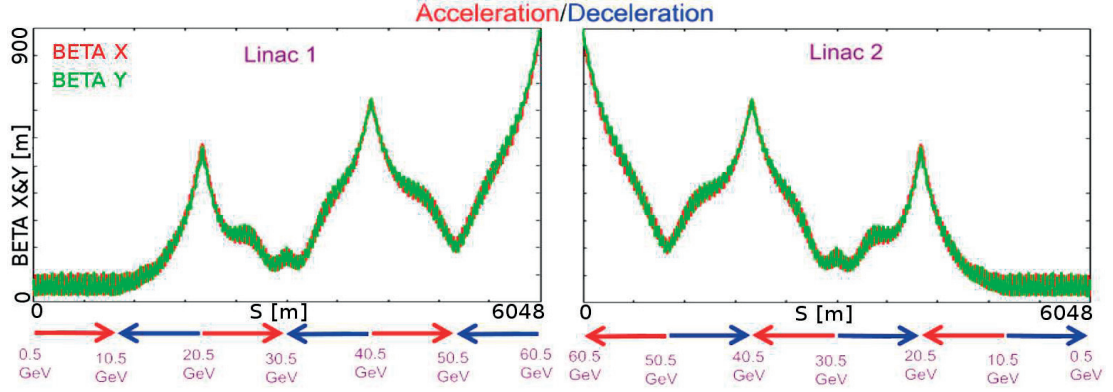
Figure 3.2: Optics functions in the linacs for the subsequent passages. The red/blue arrows indicates the accelerating/decelerating passages.

Optics constraints

When moving to the next linac, the Twiss functions must be preserved, with the only exception of the sign of $\beta' = -2\alpha$. This comes from the fact that, when decelerating, the beam keeps turning in the same direction, therefore any possible arc matching aiming at optimising the Twiss functions at each linac injection during the acceleration, would cause a mismatch during the deceleration. The optics of the two linacs are symmetric, the first being matched to the first accelerating passage and the second to the last decelerating one.

Optimisation criteria

The optimisation of the linacs optics aims at mitigating the impact of imperfections and collective effects such as wake-fields. These are driven by the parameter:

$$\left\langle \frac{\beta}{E} \right\rangle = \int_{\text{Acceleration}} \frac{\beta}{E} ds,$$

which was derived in Sec. 2.2.3.

At the LHeC one should also consider the interaction of bunches at different turns, resulting in the integrals:

$$I_{ij} = \int_{\text{Linac1,2}} \frac{\sqrt{\beta_i \beta_j}}{\sqrt{E_i E_j}} ds,$$

where the energy and the β functions need to be evaluated for the different turn numbers: i, j. One can then consider the superdiagonals (each superdiagonal is obtained for a certain n so that $i = j + n$) of the I matrix and build the merit function as:

$$F = \sqrt{\left(I_{11} + I_{22} + I_{33}\right)^2 + 2\left(I_{12} + I_{23}\right)^2 + 2\left(I_{13}\right)^2}.$$

Optimisation results

The free parameters for the optimisation are five: three of them come from the second order polynomial used to shape the strength profile of the quadrupoles along the linac, the remaining two are the initial β function and its derivative. Only one plane can be considered, the other being symmetric.

Running such optimisations three results were achieved:

1. With the constraints described above, the solution obtained minimizing F is almost identical to the one that considers only the trace of I.

2. The second order term in the quadrupolar strength profile becomes very small and only improves the total integral only by 1 %, therefore it can be discarded assuming a linear profile.

3. The result of this optimization is not far from the 130° FODO lattice already available (see Fig. 3.2) and matched to the arcs. For this reason we used that design for the initial investigation of the beam dynamics.

Substantial improvements have been obtained placing a quadrupole after every cryomodule instead of every two, as shown in Fig. 3.3. In this case the merit function is almost halved. As most of the contribution to the merit function comes from the very low energies, the additional quadrupoles may be inserted only in the initial/final part of Linac1/Linac2. This can be considered as a possible upgrade to improve the focussing and the stability of the highest beam currents of the Higgs Factory.

If the number of quadrupoles has to be preserved, one may still want to move some of them from the end of the Linac1, to the front of it, and symmetrically for Linac2. Although this is not very helpful in term of stability, the stronger focussing at low energies allows for a safer deceleration of the disrupted the beam.

3.2.2 Arcs

To accomplish the multi-turn recirculation, six arcs are fitted in a tunnel of 1 km radius. The lattice cell adopts a flexible momentum compaction layout that presents the very same footprint for each arc. This allows one to stack the magnets on top of each other or to combine them in a single design [57]. The dipole filling factor of the cell is 76 %, therefore the effective bending radius is 760 m.

The tuning of each arc takes into account the impact of synchrotron radiation at different energies. At the highest energy, it is crucial to minimize the emittance dilution, therefore the cells are tuned to contain the dispersion in the bending sections, as in a theoretical minimum emittance lattice. At the lowest energy it is possible to compensate for the bunch elongation
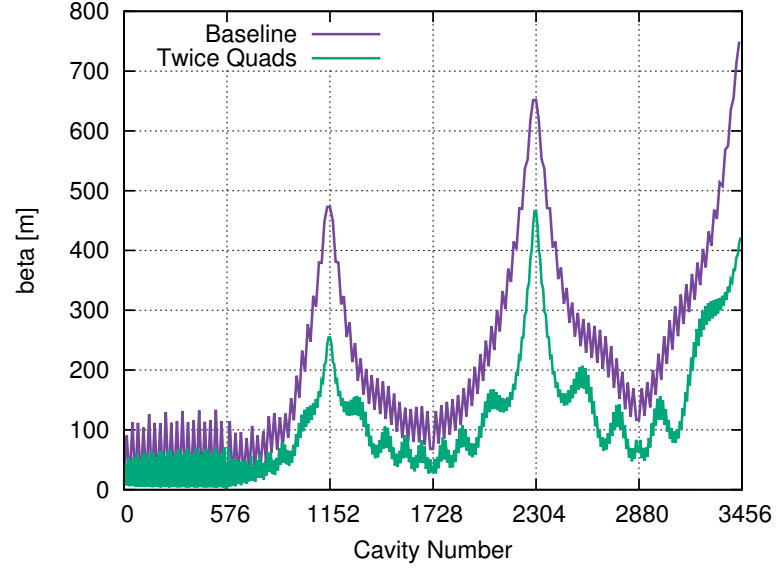
Figure 3.3: Evolution of the β function during the acceleration in the newly optimized linacs. The baseline lattice with a quadrupole every two cryomodules is compared to a proposal with twice the number of quadrupoles.

with a negative momentum compaction setup which, additionally, reduces the beam size. The intermediate energy arcs are tuned to a DBA-like lattice, offering a compromise between bunch lengthening and emittance dilution. Fig. 3.4 shows all the different cells.
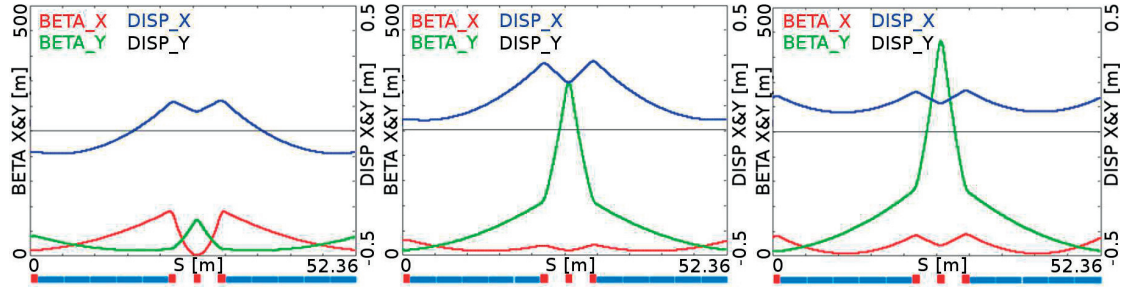
Figure 3.4: Cells for Arc1 and Arc2 (left), Arc3 and Arc4 (centre), Arc5 and Arc6 (right).

The strengths of the magnets along the arcs slightly decrease according to the energy lost by radiation.

The impact of the energy independent CSR have been estimated with the analytical formula described in Sec. 2.4. Each arc causes an energy loss of 1 MeV and introduces an energy spread of 7×10^{-5}. The CSR has not been included in tracking simulations as it is not expected to be the dominant effect.

3.2.3 Arcs based on Combined Function Magnets

Developments in the magnet technology allows one to obtain better and better field quality on bigger and bigger apertures. This can be exploited adopting a cell based combined magnet for the return arcs. In its ultimate realization the lattice is composed only by quadrupole magnets, properly displaced to provide the horizontal bending.

A peculiar property of this lattice is that periodic solutions over a wide range of energies (up to a factor 4 between the lowest and the highest one) are contained within few centimetres. This makes it a viable candidate for fast and compact rings, which can accelerate particles without varying the current in the magnets, as was successfully tested at EMMA [58]. From this application arises the alternative name: non-scaling, fixed-field, alternating gradient, or ns-FFAG, where non-scaling means that orbit at different energies have different shapes[1].

Another possible application of the FFAG lattice is as return arc of multi-pass ERLs. In this case the main advantage is the possibility to transport multiple beams at different energies with a single beam pipe. By adopting this design, the eRHIC plans have up to 16 different energies in the linac with only two return arcs [2].

In the context of the LHeC, the higher energies limit how much the beam can be bent, therefore a limited number of turns remains a priority. Nevertheless, the fact that all the magnets contribute to the bending, allows one to obtain filling factors up to 95 % (in the current design it is 76 %) resulting in a bigger effective bending radius, and therefore lowering the energy lost by synchrotron radiation.
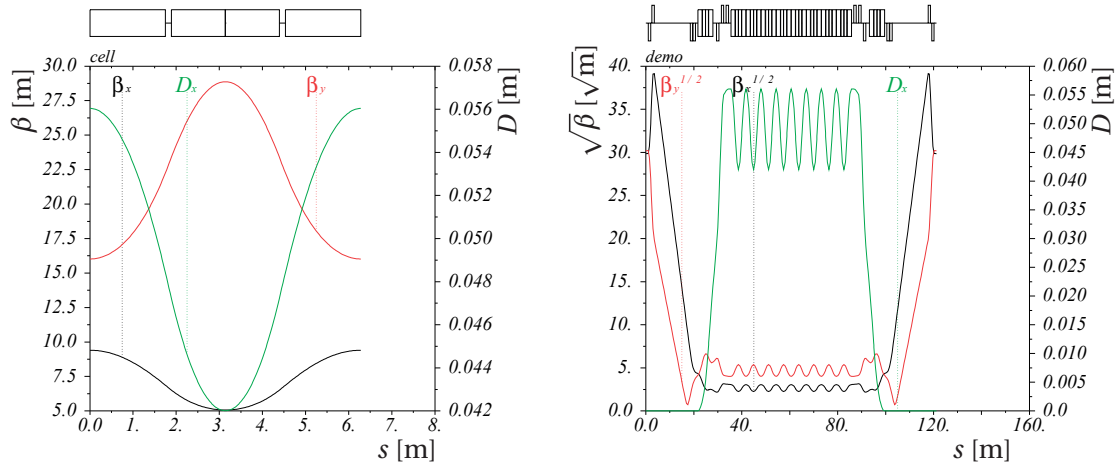
Figure 3.5: *left:* A lattice cell based on combined function magnets and *right:* a demonstrator of the drop-in design for Arc6.

A drop-in replacement for the LHeC Arc6, based on the combined function cell presented at the 2015 LHeC Workshop [59], was designed and tested. The arc is composed of a section that matches the optics functions from the linac and generates the required dispersion using one

---

[1]Note that scaling designs are also possible, but typically result in very big magnets.

bending cell. Additional 498 cells complete the horizontal bending. Figure 3.5 shows a lattice cell based on combined function magnets. In addition a demonstrator of the complete arc (it has much less cells in the periodic section to better show the optics) is presented.

Tracking was performed with PLACET2. It confirmed the reduction of the emitted radiation without pointing out any evident drawback on the performance. Further investigations are required to determine if multiple energies could fit within the same lattice.

3.2.4   Spreader and Recombiner

The spreaders are placed after each linac and they separate the bunches at different energies in order to route them to the corresponding arcs. The recombiners do just the opposite, merging the beams into the same trajectory before entering the next linac.
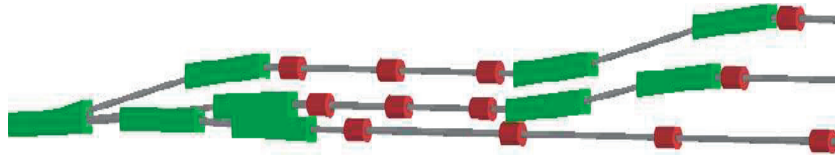
Figure 3.6: Layout of the vertical spreader in the CDR. The vertical separation is achieved in two steps.

The spreader design, shown in Fig. 3.6, consists of a vertical bending magnet that initiates the separation. The highest energy, at the bottom, is brought back to the horizontal plane with a chicane. The lower energies are captured with two-steps vertical bendings. The two-steps design simplifies the suppression of the vertical dispersion, but also induces a non negligible energy loss, especially for Arc4; moreover it raises the horizontal β function to very high values.

A new single-step design developed for Arc2 and Arc4 targets both drawbacks. The energy loss is reduced by a factor 5 and at the same time both the dispersion and the β functions are mitigated. A comparison of the baseline and proposed optics for Arc2 and Arc4 spreaders is shown in Fig. 3.7. All of them provide a final vertical separation of ~0.5 m between the three arcs.

The single step spreader starts with a dipole that integrates a small focussing quadrupolar component. This improves the separation of the beta functions and allows one to place a defocussing quadrupole few meters downstream to bring back the vertical dispersion. The following quadrupole triplet focuses the beam. The next quadrupole does not affect the dispersion as it is placed where it crosses the zero, it offers an extra degree of freedom to control the beta functions. The second half of the cell is almost symmetric. There are two reasons to brake the symmetry:

1. increasing the drift space after the first magnet to better separate the beamlines, while containing the total length,

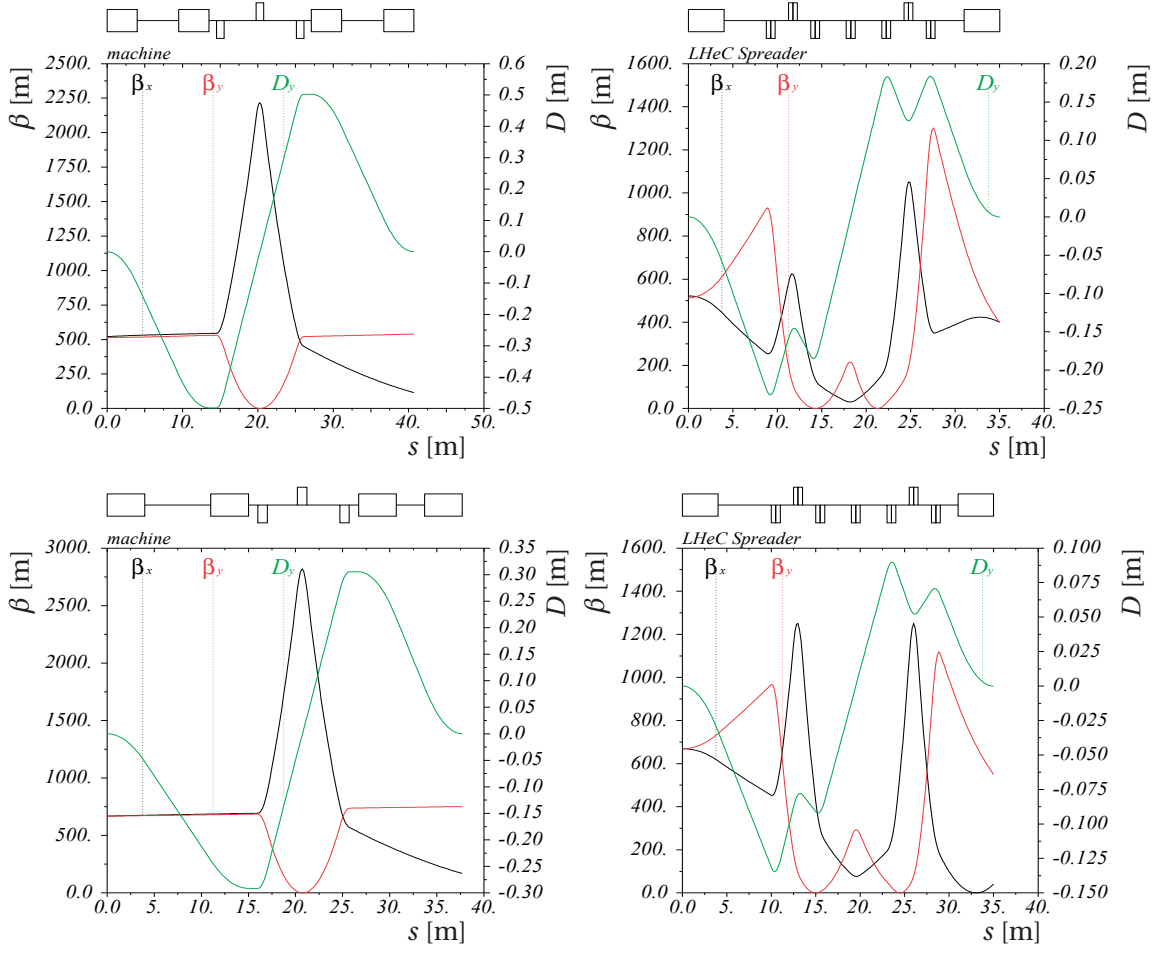Figure 3.7: Optics functions for the vertical spreaders. The top row is at 20 GeV, the bottom at 40 GeV. The left column shows the two-step design, the right one is the proposed single step design.

2. the outgoing beta functions can be made smaller than the incoming ones, easing the matching in the following section.

To avoid conflicts, care has been taken to longitudinally displace the quadrupoles of the two beamlines, as shown in Fig. 3.8. Small adjustments are expected and will follow the verification of the integrability of the systems with technical drawings. The maximum quadrupole gradient of 80 T/m cannot be reached with warm magnets, although is not too challenging to adopt superconducting technology since the cryogenics is readily available from the nearby linacs.

Figure 3.8: The magnets of Arc2 and Arc4 spreaders are interleaved. The angle between the two beamlines is not taken into account.

3.2.5 Bypasses

Recent studies investigated the possibility to install the LHeC detector inside the magnet originally built for the L3 experiment at LEP and now being employed by the ALICE experiment at the LHC. The outer radius of this magnet is 7.9 m [60]. The vertical separation provided by the spreader (see Sec. 3.2.4) is not sufficient for the 20 GeV and 40 GeV beams to avoid the detector and bypass lines are required.

Two designs have been investigated, both of them displacing Arc2 and Arc4 by 10 m with respect to the IP. The step design makes the displaced beams parallel to the colliding beam. The straight design avoid that and directly joins with the arcs. While the first is easier to implement, it also causes a bigger energy loss due to the extra bending. The straight design is more suitable to the LHeC operation and will be discussed in the following paragraphs.

Geometry of the straight bypass

The geometry scheme of the straight bypass is shown in Fig. 3.9. The bypass starts after the spreader and consists of the following components:

1. a minimal matching section (not shown);

2. a bending section that provides the separation with respect to the detector (point A);

3. a straight section (segment $\overline{AB'}$);

4. a modified dispersion suppressor (point B');

5. a junction consisting of seven special arc cells with increased bending strength, replacing ten standard arc cells (arc $\overline{B'C}$).

53

After the junction, at point C, Arc2 and Arc4 becomes again superimposed to Arc6.
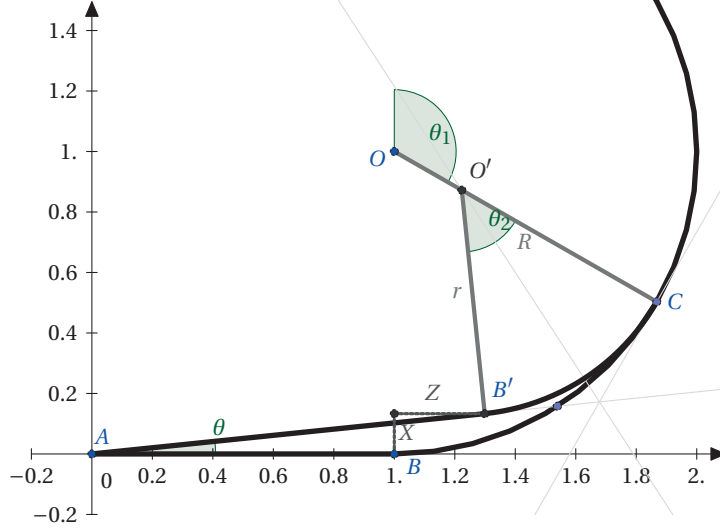
Figure 3.9: Scheme of the bypass geometry. The IP line, $\overline{AB}$, has been purposely stretched, being actually $\sim 1/5$ of the arc radius.

In order to evaluate the geometry we need to determine an expression for the junction radius r as function of the angles θ_1 and θ_2 and the position of the detector, as shown in Fig. 3.9. We start computing the quantities X and Z which determine the starting position of Arc2 and Arc4 (point B') with respect to the starting position of Arc6 (point B). These are obtained as:

$$
\begin{aligned}
X &= R + (R - r)\cos(\theta_1) + r\cos(\theta_1 + \theta_2); \\
Z &= (R - r)\sin(\theta_1) + r\sin(\theta_1 + \theta_2).
\end{aligned}
\tag{3.1}
$$

The detector is placed on the segment $\overline{AB}$. We call x_D the distance of the detector from point A, and z_D the corresponding separation of the bypass. The following relation must then hold:

$$
D \equiv \frac{x_D}{z_D} = \frac{X}{Z + \overline{AB}}.
\tag{3.2}
$$

Substituting the expressions from 3.1 into 3.2, we finally obtain an expression for r:

$$
r = \frac{D(R\sin(\theta_1) + \overline{AB}) - R(1 + \cos(\theta_1)}{\cos(\theta_1 + \theta_2) - \cos(\theta_1) - D(\sin(\theta_1 + \theta_2) - \sin(\theta_1))}.
\tag{3.3}
$$

At this point we can obtain the values of X and Z substituting 3.3 back into 3.1 and the computation of the length $\overline{AB'}$ follows.

Bypass tuning

Small adjustments have then to be done considering an integer number of cells and magnets, and the non-null radius of the bending section at point *A*. The optics of the full bypass is shown in Fig. 3.10, the specific components have been tuned as follows:

- *Matching:* A quadrupole doublet placed right after the spreader brings down the beta function. An exact matching is not required, indeed compactness is preferred to minimize the angle in the bending section.

- *Bending:* The bending section at point *A* provides the separation of Arc2 and Arc4 with respect to the detector which is assumed $z_D = 120$ m downstream. A separation of $x_D = 10$ m requires an angle of $\theta = 4.76°$. This is obtained using 10 bending magnets. The dispersion is suppressed with 3 quadrupole magnets distributed between the dipoles.

- *Straight Section:* The straight section $\overline{AB'}$ is approximately 300 m long. It transports the beam to the arcs and matches the Twiss functions. The current design employs two quadruplets of magnets at its extremes. A long section of approximately 250 m is magnet-free. This may help to minimise the detector separation and can be exploited by diagnostics and/or to adjust the beam time-of-flight for these specific arcs.

- *Junction:* The junction consists of a modified dispersion suppressor and seven special arc cells (with stronger dipoles) that replace ten standard cells at the beginning of Arc2 and Arc4. The dipoles in the suppressor and in the junction are tuned to obtain a total bending of 180° with a reduced radius. The quadrupolar strengths in the junction cells are the same as in the arc cells. This creates a little mismatch in the junction cells that is removed in the dispersion suppressor. In Arc2 the mismatch is more evident and it has been cured by adjusting the quadrupoles in the last junction cell and in the first regular cell.

3.2.6 Compensating RF

The synchrotron radiation in the arcs causes significant energy losses, especially in the incoherent part of the spectrum (see Tab. 3.4). If no countermeasures are adopted, the energy of the beam in the decelerating phase would be lower than one in the corresponding accelerating phase, precluding the transport in the same arcs. To prevent the issue, the energy lost has to be replenished into the beam, so that at the entrance of each arc the accelerating and decelerating beams have the same energy. This is achieved by means of dedicated RF cavities installed in the arcs. Their operating frequency is 1604 MHz, twice the one of the linacs. As schematised in Fig. 3.11, the use of second harmonic RF frequency, allows each section to restore the energy for both the accelerating and the decelerating beams.

An estimation of the parameter of these cavities and cryomodules is collected in Tab. 3.3. They have been extrapolated from the ILC cavity design, expecting that the higher frequency
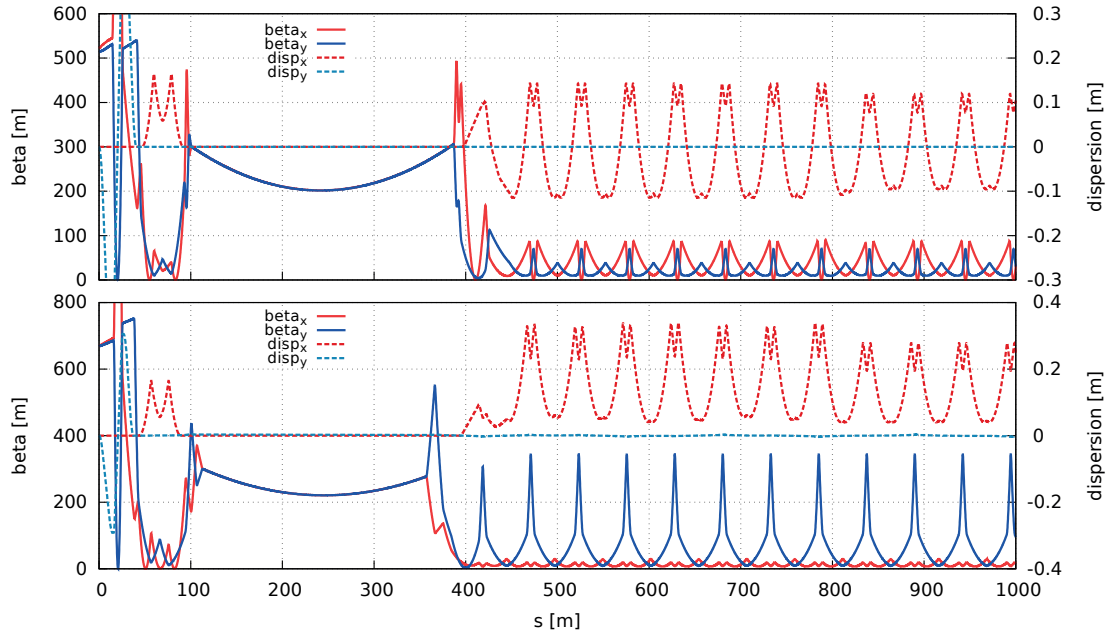
Figure 3.10: Beta functions and dispersion at the beginning of Arc2 (top) and Arc4 (bottom) with the detector bypass included. One can recognise the vertical spreader, the initial horizontal bending, the straight section, the modified dispersion suppressor, the seven junction cells, and four regular cells. The plot is produced with PLACET2 and Gnuplot.
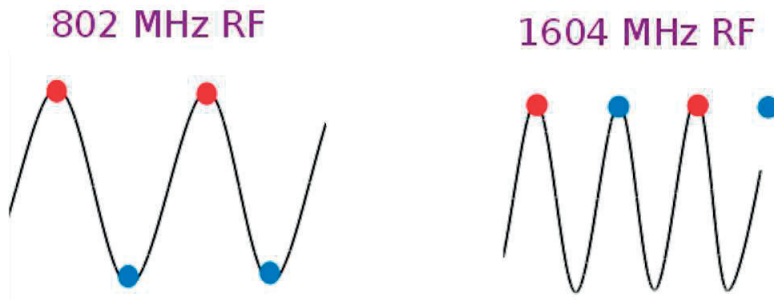
Figure 3.11: The second harmonic RF restores the energy loss both in the accelerating and decelerating passages.

Table 3.3: A tentative parameter list for the compensating RF cavities and cryomodules, extrapolated from the ILC design.

Frequency	1604 MHz
Gradient	30 MV/m
Design	9 cells
Cells length	841 mm
Structure length	<1 m
Cavity per cryomodule	6
Cryomodule length	~6 m
Cryomodule voltage	150 MV

Table 3.4: Energy loss, power dissipation and required number of cryomodules for each arc. The coherent, energy-independent radiation triggers an additional loss of about 1 MeV in each arc.

Arc	E [GeV]	ΔE [MeV]	P [MW]	Cryomodules
1	10.4	0.7	0.04	0
2	20.3	9.9	0.5	0
3	30.3	48.5	2.4	1
4	40.2	151	7.6	1
5	50.1	365	18.2	3
6	60.0	751	18.8	6
Total		1901	47.5	10

and the lower gradient allow for continuous operation. Although these cavities comes with stronger higher order modes, the reduced current that they see and their limited length are expected to be enough avoid beam stability issues. Table 3.4 shows the energy loss for each arc, together with the required number of cryomodules. The computation of the power dissipated takes into account the fact that Arc6 transports 25 mA of beam current while all the others 50 mA. The heat load from synchrotron radiation is 6 kW/m for both Arc6 and Arc5. This is a factor 3.5 higher with respect to LEP II, where the vacuum chamber was kept below 50 degrees with 79 m long cooling circuits [61]. Shorter cooling circuits allow one to dissipate more power and could be suited to the LHeC case.

The compensating cavities are placed on the Linac1 side of the racetrack; this saves space on the Linac2 side to better fit the IP line and the bypasses. They can be accommodated in low betas insertions between the spreader/recombiner and the dispersion suppressors of the arcs. With the current vertical separation of 0.5 m it will probably not be possible to stack the cryomodules on top of each other; therefore they will occupy 42 m on the Arc4/Arc6 side and 24 m on the Arc3/Arc5 side. As can be seen in Fig. 3.1, these lengths are easily fitted in the racetrack layout.

Each of the compensating cavities in Arc5 needs to transfer up to 1 MW to the beam. While a 1 MW CW klystron is already operating at the BNL ERL [62], the integration of six of them in the cryomodule will require a careful design.

As their total impedance is small compared to the one of the linacs and they only see a fraction of the linac current, they are not expected to significantly impact the beam stability.

3.2.7 Doglegs for path length adjustments

The total lengths of each recirculating arc need to be carefully tuned in order to obtain the right time-of-flight and the correct phase in the linacs. As the linacs are operated on crest, no phase-stability mechanism can take place; therefore errors in the beam time-of-flight, being additive from one turn to the next one, can have catastrophic effects. While gross adjustments of the lengths have to be included in the design in order to provide the correct bunch recombination pattern (this will be described in Sec. 3.5.2), fine tunings knobs are required to apply small corrections, both in the commissioning and during the operation.

The most straightforward way to allow for path-length adjustments is by means of four-bend chicanes that can be placed next to the RF compensating sections. Synchrotron radiation poses an upper limits to the bending angle in those chicanes, in particular for the highest energy beams. These can be computed from the formula for the energy loss:

$$U_0 = \frac{C_\gamma}{2\pi} E_0^4 I_2, \tag{3.4}$$

where the integral I_2 is computed over the length of the dipole L_d. The integration is trivial in case of a constant bending radius ρ:

$$I_2 = \int \frac{1}{\rho^2}\, \mathrm{d}s = \frac{L_d}{\rho^2} = \frac{\theta^2}{L_d}.$$

We obtain:

$$\theta = \frac{1}{E_0^2} \sqrt{\frac{2\pi U_0 L_d}{C_\gamma}}, \tag{3.5}$$

and from the angle we can get the path length variation:

$$\Delta L = L - l = l \left(\frac{1}{\cos\theta} - 1 \right), \tag{3.6}$$

where L indicates the path length at the maximum deviation angle, while l is the path length at zero angle.

Assuming $L_d = 1$ m, a maximum energy loss $U_0 = 1$ MeV in each of bending magnets (4 MeV for the whole chicane) and the length $l = 6$ m, we can compute the effect on the path-length of

the chicanes at different energies. These are summarised in Tab. 3.5, to be compared with the linac wavelength of 0.374 m.

Table 3.5: Maximum bending angle and path-length variation for a 6 m chicane at different energies.

Energy [GeV]	θ [rad]	ΔL [m]	B [T]
10	0.256	0.2023	2.14
20	0.064	0.0123	1.07
30	0.028	0.0024	0.71
40	0.016	0.0008	0.53
50	0.010	0.0003	0.43
60	0.007	0.0002	0.36

While at low energy the chicanes are practical and few of them allow one to tune the path length over a range exceeding the linac wavelength, at higher energy they are not very effective even in big numbers and pushing their strength one gets significant energy losses.

A possible solution for path length adjustments in Arc5 and Arc6 may consist in introducing a betatron oscillation in the beam orbit. This allows one to take advantage of the whole arc, thus the perturbation can be much smaller. The feasibility and the effectiveness of this scheme have not been investigated.

For Arc4 and Arc2 one can also take advantage of the bypass section to install one or more, eventually longer, chicanes.

3.3 End-to-End Tracking Simulations

The effects that are mostly expected to have an impact on the quality and the stability of the electron beam at the LHeC are:

- optics effects (bunch compression and elongation in the arcs, induced energy spread from the RF curvature),

- synchrotron radiation,

- beam-beam disruption,

- short and long-range wakefields,

- ion cloud,

- machine imperfections, phase and timing errors.

It should be noted that often it is not only important to study these effects separately, but also investigate their interplays. For instance the action amplification caused by the beam-beam interaction has an impact on the beam stability in presence of long-range wakefields.

To describe the machine layout and operation in a natural way the PLACET2 code [63] was developed and applied. The aforementioned effects have been studied in details with the only exception of the ion cloud and the imperfections: the first is a planned addition to PLACET2 while the second requires the development of effective correction schemes which goes beyond this study.

The simulation includes the two linacs and the six arcs, properly connected together, with the spreaders and matching sections. The synchrotron radiation is computed in the whole arcs excluding the spreaders-recombiners, as their current two-step design causes unacceptable energy losses. The computation of the beam-beam effect relies on GUINEA-PIG [64]. The second harmonic RF, required to replenish the energy lost by synchrotron radiation, is currently modelled as a thin element. The tuning of the arc lengths is not yet integrated into the design: for the time being, the time-of-flights have been adjusted with special elements that introduce the required delays.

Unless otherwise indicated the studies presented in the following sections use the Higgs Factory (or Hi Lumi) beam parameters summarised in Tab. 3.2.
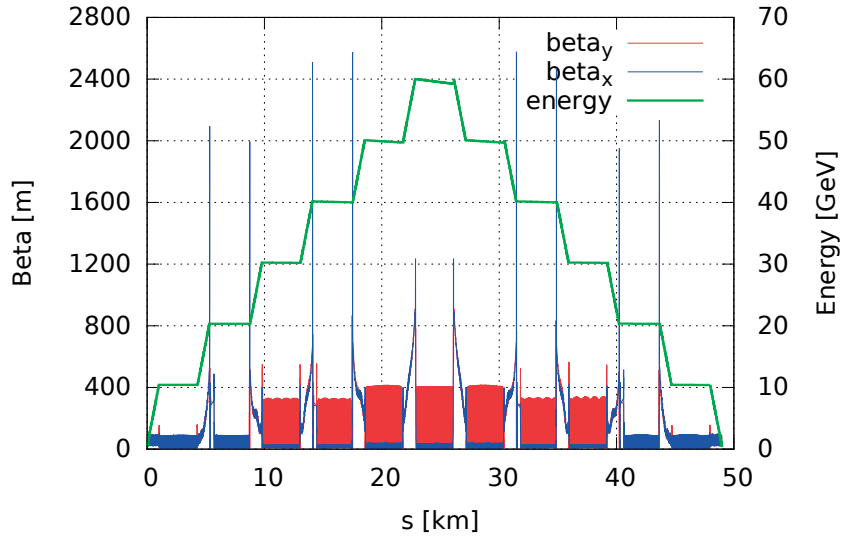

Figure 3.12: Beta functions and energy profile obtained following a bunch in the whole LHeC lattice.

3.4 Single-Bunch Tracking

The transport of a single bunch from the injector to the dump is the first step to validate the machine design and the simulation framework. Fig. 3.12 shows the Twiss parameters obtained following a bunch along its path from the injector to the dump. The linacs are easily identifiable by looking at the energy profile. In the arcs the energy stays almost constant, the only variation being caused by the synchrotron radiation. It is possible to note the different average values of the β functions in different arcs, deriving from their different tunings of the momentum compaction, as previously described. A small beta beating can be barely noted in the arcs: it is caused by the different model of the RF-focussing in the linacs between PLACET2 and OptiM [65], the program used for the matchings.

During the transport, the main degrading effects for the bunch quality are incoherent synchrotron radiation and short-range wake-fields, both are implemented in PLACET2. An approximation of the wake functions have been computed using the formulas presented in Sec. 2.1.2 and the cavity geometry described in [28]. Figure 3.13 shows that synchrotron radiation has a much bigger impact than wake-fields both on the emittance and on the induced energy spread. In particular in presence of radiation the wake-fields slightly improve the beam quality compensating the energy spread during the deceleration. This hints that further marginal improvements may be obtained with a fine tuning of the arc lengths, adjusting the phases at the linac injections.
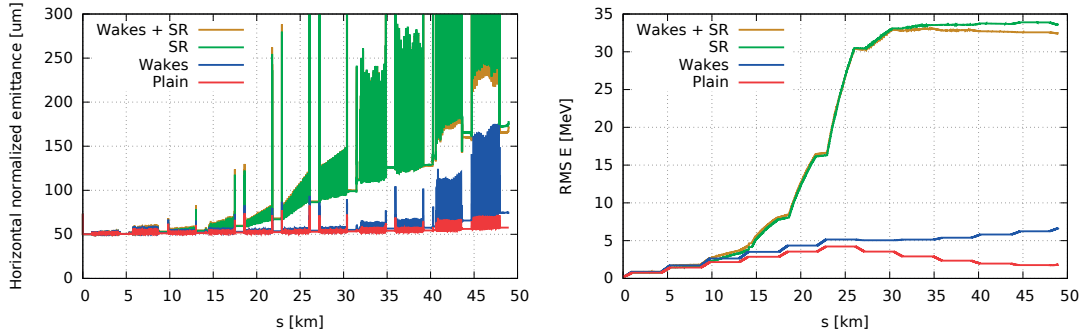
Figure 3.13: Horizontal emittance and Energy RMS of a bunch tracked from the injector to the dump with an initial horizontal displacement of 1 mm, required to excite the transverse short-range wakefields. The blow up caused by synchrotron radiation and wake-fields are compared. The emittance includes the contribution from the dispersion, thus its value in the arc is not significant.

The longitudinal phase space at the dump is shown in Fig. 3.14. The effect of the non isochronicity of the arcs is visible in the plane tracking, where the RF curvature induced during the acceleration is not totally compensated in the decelerating phase. The short-range wakefields have a visible, but small impact as a consequence of the big iris of the cavity design. When the synchrotron radiation is turned on, both these effects are masked. The bunch length remains well preserved in all the cases. The beam-beam effect does not have a significant

Figure 3.14: Longitudinal phase space at dump. The left plot shows the plain tracking (grey) and the short-range wakefield (violet). The right plot also adds the effect of synchrotron radiation.
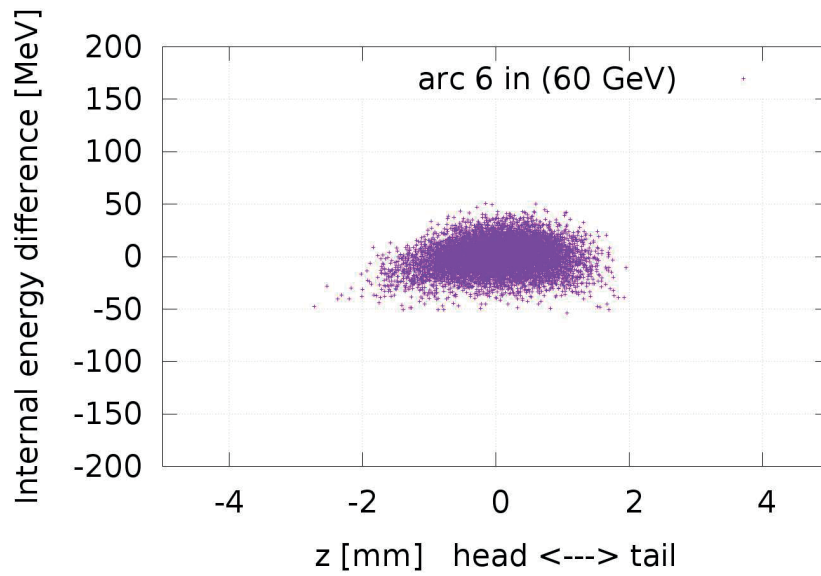
Figure 3.15: Longitudinal phase space at the IP. The zero of the vertical axis represents an energy of 60 GeV.

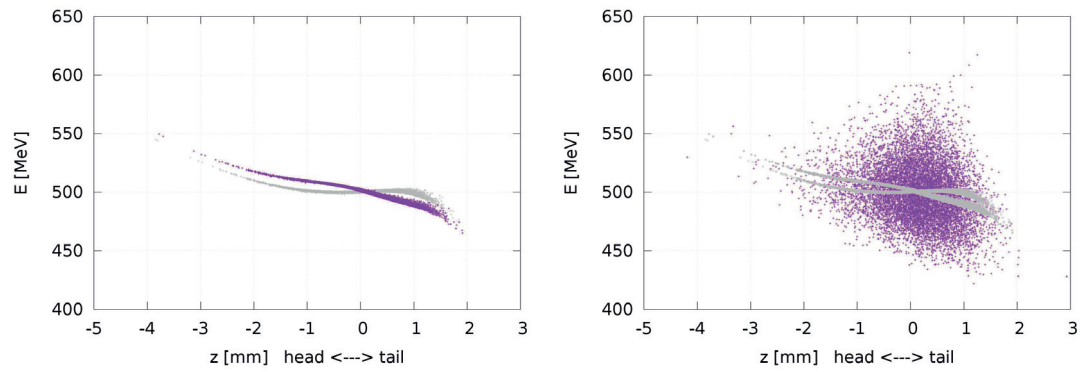impact on the longitudinal phase space. Figure 3.15 shows the bunch at the IP, a tolerable amount of RF curvature can be noted.
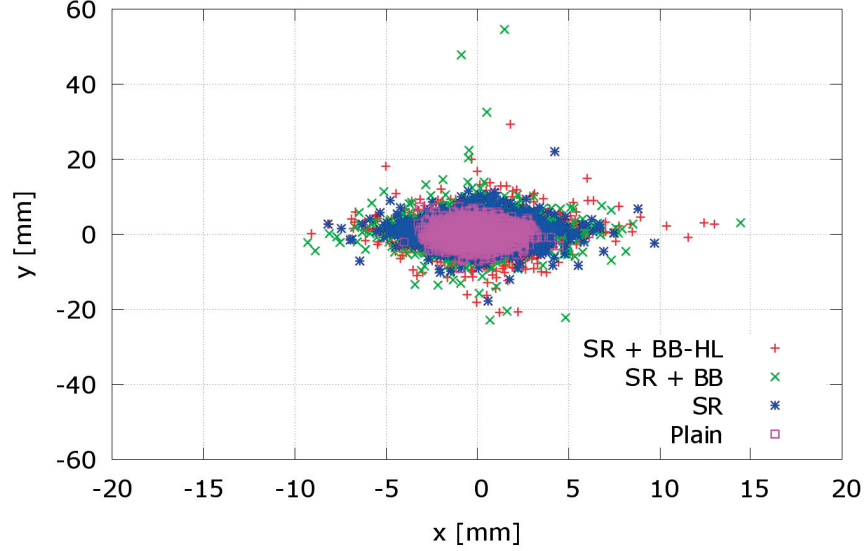
Figure 3.16: Beam transverse section at the end of the last linac, after the deceleration, including Synchrotron Radiation and Beam-Beam with standard and Higgs Factory (High Lumi) parameters. The beam contains 5000 macroparticles and the initial distribution is gaussian with no cuts.

The transverse emittance growth during the transport to the IP is acceptable. The impacts of beam-beam and synchrotron radiation (especially in Arc6) are evident in the transverse plane, but not detrimental to the deceleration. The beam envelope remains well within the aperture even at the end of the deceleration as shown in Fig. 3.16.

The beam parameters are summarized in Tab. 3.6 and Tab. 3.7 respectively at the IP and at the dump (after the deceleration).

Table 3.6: Initial beam parameters compared to the ones at the IP in presence of synchrotron radiation

	initial/CDR	IP
ε_x [μm]	50	57.4
ε_y [μm]	50	50.8
δ [%]	0.20	0.026
RMS x [μm]	7.20	7.66
RMS y [μm]	7.20	7.21
RMS z [mm]	0.600	0.601
RMS e [MeV]	1.00	15.4

It should be noted that the emittance blow up poses a lower limit to the injection/dump energy

Table 3.7: Beam parameters at the dump. The columns show the values for SR only, SR and Beam-Beam, SR and Beam-Beam with Higgs Factory (High-Lumi) parameters.

	Final SR	SR + BB	SR + BB-HL
ε_x [μm]	107	133	165
ε_y [μm]	87	125	158
δ [%]	5.9	5.9	5.9
RMS x [mm]	1.52	1.67	1.86
RMS x' [mrad]	0.08	0.09	0.10
RMS y [mm]	2.42	3.03	3.15
RMS y' [mrad]	0.07	0.09	0.09
RMS z [mm]	0.66	0.66	0.66
RMS e [MeV]	29.7	29.5	29.6

that is independent from the one due to the multi-bunch effects and can be more restrictive. Indeed further deceleration of the beam yields losses of the particles in the tails. The maximum current would then be limited by the long term energy deposition causing material activation, damage and eventually quenching. Furthermore the RF power requirements would increase for cavities where the losses start to take place as consequence of the degradation of the energy recovery process. Adding more quadrupole magnets in the linacs as proposed in Sec. 3.2.1 will allow one to relax this limit, helping to reduce the injector energy and power consumption. This could have have a profound impact on the overall machine cost and operation.

3.5 Multi-bunch Tracking

After the lattice validation tracking a single bunch, the more complex multi-bunch dynamics has been investigated. A major concern for the operation of the ERL facilities at high currents are long-range wakefields, in particular the ones related to transverse dipole modes that are easily excited in the cavities.

To proceed with this study the modes of the SPL cavity design were used. The SPL and the LHeC cavities are both 5-cell designs and their frequencies are similar: 720 MHz and 802 MHz. It is therefore reasonable to use the same modes, scaling their amplitudes with the cube of frequency. Table 3.8 collects the dipole modes considered. The *Q* values of all the modes are conservatively set to 1×10^5, which is the worst value encountered in the TESLA cavity.

The computation times have been reduced using single particle bunches, which is a conservative approach, as the tune spread is known to improve the threshold current [66]. To avoid spurious contributions from the finite numerical accuracy of the dipoles transfer maps, the arcs were substituted with matrices, preserving their lengths and the reflection of the beta functions. The full computation of the beam-beam effect has been substituted with an amplitude dependent kick, this is also a conservative approach as the electrons oscillates

Table 3.8: Summary of the dipole modes considered while investigating long-range wakefields.

| Mode #	f [GHz]	A [V/C/m^2]	Q	Mode #	f [GHz]	A [V/C/m^2]	Q
1	0.9151	9.323	1e5	14	1.675	4.160	1e5
2	0.9398	19.095	1e5	15	2.101	1.447	1e5
3	0.9664	8.201	1e5	16	2.220	1.427	1e5
4	1.003	5.799	1e5	17	2.267	1.377	1e5
5	1.014	13.426	1e5	18	2.331	2.212	1e5
6	1.020	4.659	1e5	19	2.338	11.918	1e5
7	1.378	1.111	1e5	20	2.345	5.621	1e5
8	1.393	20.346	1e5	21	2.526	1.886	1e5
9	1.408	1.477	1e5	22	2.592	1.045	1e5
10	1.409	23.274	1e5	23	2.592	1.069	1e5
11	1.607	8.186	1e5	24	2.693	1.256	1e5
12	1.666	1.393	1e5	25	2.696	1.347	1e5
13	1.670	1.261	1e5	26	2.838	4.350	1e5
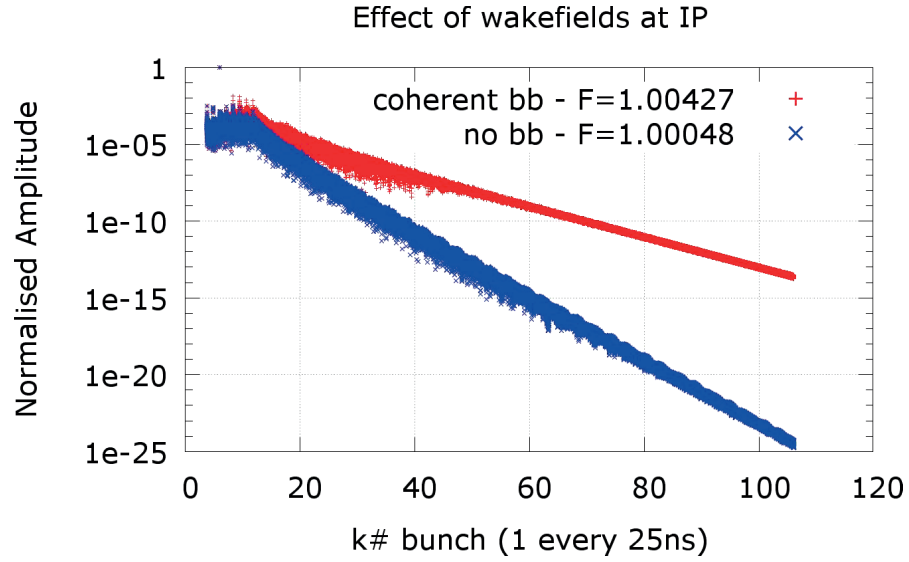
Figure 3.17: Normalised actions of the bunches at the IP. Only the bunch with action 1 carries an initial misalignment. All the other bunches are excited by LRW. Each bunch contains 4×10^9 electrons.
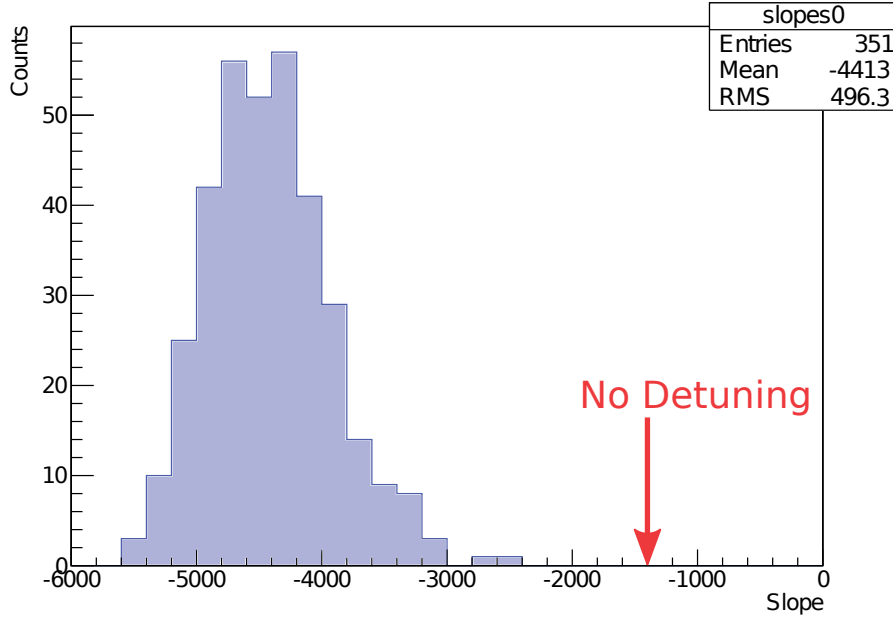
Figure 3.18: Distribution of the excitation slopes for many machines with the same detuning factor of 1×10^{-3}.

around the proton beam and the total kick that they receive is smaller.

The beam stability studies are performed filling completely the machine with approximately 6000 single-particle bunches carrying a vanishing action. One misaligned bunch is then injected followed by many bunches again with vanishing action. The perturbation introduced by the misaligned bunch is propagated to all the others, even to the ones injected before, as they turn together in the ERL. There are two important parameters: the slope of the tail, which determines if and how fast the perturbation is damped; and the F parameter that represents the total amplification of the beam action, defined as the squared sum of all the amplitudes [35]. As the process follows an exponential law, this sum is convergent and mostly driven by the bunches that are close to the exciting one.

The final result of this study is presented in Fig. 3.17. The plot shows the propagation of the excitation with the Higgs Factory beam parameters with and without the beam-beam amplification. It can be noted how the beam beam kick adds on top of the wakefields making the perturbation more persistent, although still not destructive. The beam actions are taken before the IP, this simplifies the normalisation with respect to the case in which the data is taken at the dump, as the amplification introduced by the beam beam kick has yet to be applied to the observed bunches. The plot was obtained considering a standard detuning factor of 1×10^{-3} and the optimal bunch pattern. Both of these will be explained in the following sections.

3.5.1 RF Cavity Detuning

The detuning consists in a variation of the frequencies of the modes from cavity to cavity. It occurs naturally, being caused by small imperfections in the cavity geometry originated in the fabrication process. The frequency spread is typically extracted from a gaussian distribution, whose normalised standard deviation is the detuning factor $D = \sigma_\omega / \omega$. The detuning causes a dephasing of the modes that therefore cannot build up in a coherent way.

As the frequency variation is random the detuning can have different impacts even for the same value of D, according to the exact frequency assigned to each cavity. However with a big number of cavities, as in the LHeC case, this effect tends to be mitigated and different distributions produce similar results. This is depicted in the histogram in Fig. 3.18 which collects the slopes of excitation tails (similar to the one shown in Fig. 3.17), for 351 different machines with the same detuning factor: $D = 1 \times 10^{-3}$. It can be seen that such detuning improves the beam stability by a factor 4 on average, increasing the margin on the threshold current.

3.5.2 Bunch Recombination Pattern

The choice of 802 MHz RF frequency leads to 19 empty buckets between two injections at 25 ns, that can host the bunches at higher turn numbers. The spreader and recombiner design, employing fixed-field dipoles, do not pose timing constraints. This gives us full control of the recombination pattern that can be selected by adjusting the length of the return arcs to the required integer number of wavelengths.

In order to avoid boosting short-range wakefields, the lengths of the arcs should be tuned preventing the recombination of different bunches in the same bucket, as would happen if the full turn length was an integer number of 20λ. One should also avoid to place the fresh bunches at the first turn right after the bunches at the sixth turn that have collected plenty of perturbations.

A good choice for the recombination pattern consists of almost equal spacing (compatibly with the RF) of the bunches in the RF buckets and a maximal separation between the bunches at the lowest energy that are more subjected to the kicks from the HOMs due to their lower rigidity. This is illustrated in Fig. Fig. 3.19.

Figure 3.20 shows two excitations obtained with the detuning factor set to zero. A recombination pattern that poses bunches at the first turn right after bunches at the sixth, makes the beam unstable, on the other hand stability is obtained for the pattern shown in Fig. 3.19.
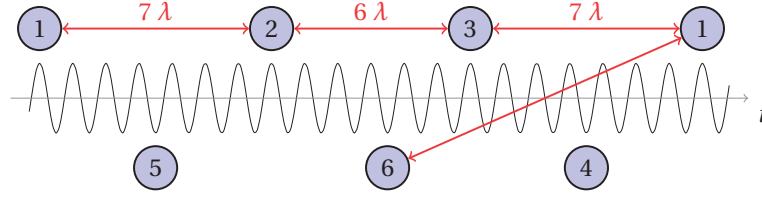
Figure 3.19: A possible recombination pattern that maximises the separation between the bunches at first and sixth turn.
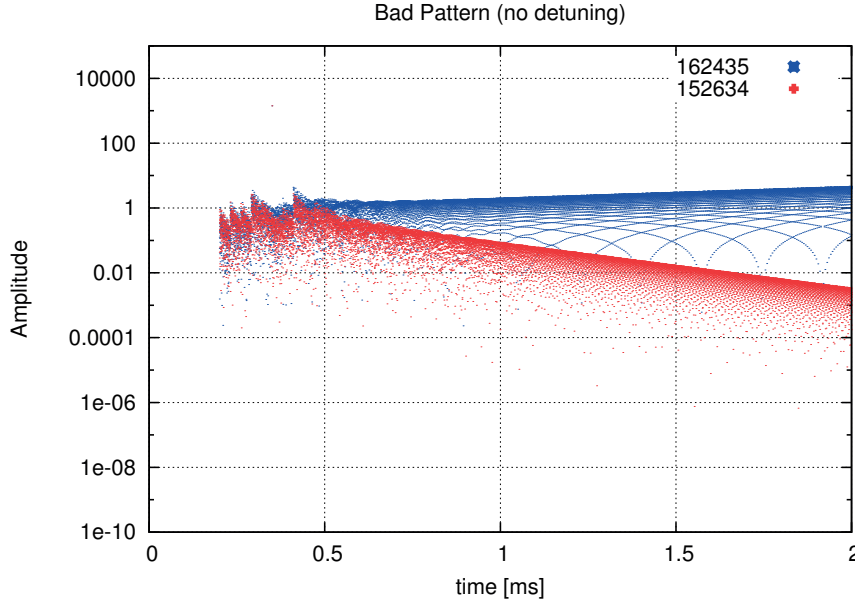
Figure 3.20: Excitation produced by two different recombination patterns.

3.5.3 Phase Advance in the IP line

A complete design of the IP line is not yet available in the full lattice. For this reason the final focus and the post IP section are implemented as matrices. The transformation matrix that allows one to match the twiss parameters from the Linac the IP is:

$$M = \begin{pmatrix} \sqrt{\frac{\beta_{IP}}{\beta_L}}(\cos\varphi + \alpha_L \sin\varphi) & \sqrt{\beta_{IP}\beta_L}\sin\varphi \\ \frac{\alpha_L - \alpha_{IP}}{\sqrt{\beta_{IP}\beta_L}}\cos\varphi - \frac{1+\alpha_{IP}\alpha_L}{\sqrt{\beta_{IP}\beta_L}}\sin\varphi & \sqrt{\frac{\beta_L}{\beta_{IP}}}(\cos\varphi - \alpha_{IP}\sin\varphi) \end{pmatrix}; \tag{3.7}$$

a similar matrix is used to go from the IP back to the Linac. The transformation contains a free parameter: the phase advance φ; which determines the mixing between angle and offset of the beam and generally has an impact on the stability in presence of long-range wakefields. In

the complex scenario of the LHeC this is not easily predicted and a parameter scan has been done. Figure 3.21 shows that the beam stability can be enhanced for specific values of the phase advance in the IP line, therefore the final focus optics should allow for a tuning of this parameter.
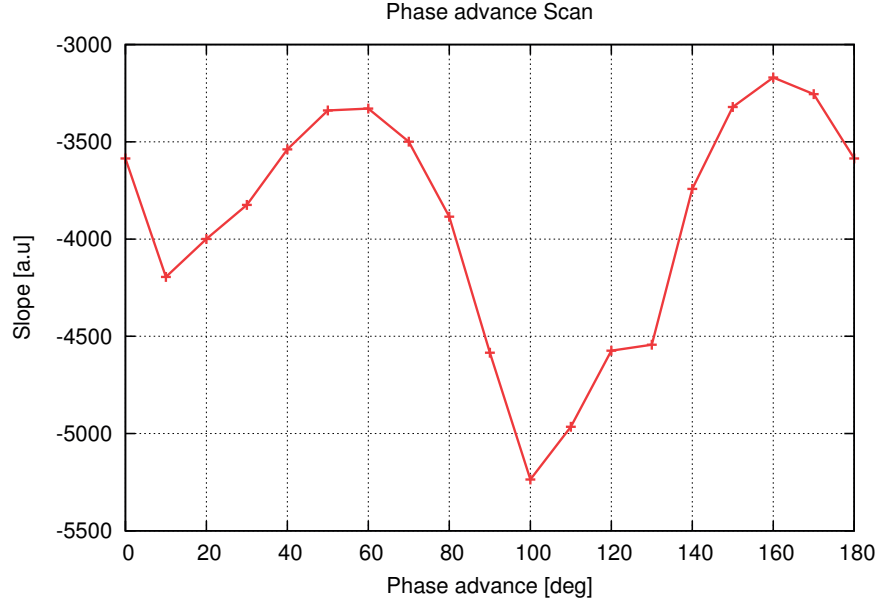

Figure 3.21: Slopes of the excitation obtained as function of the phase advances in the lines pre and post IP (both the phase advances are simultaneously set to the same value).

3.6 PERLE

PERLE stands for Powerful Energy Recovery Linac Experiments, the project was formerly known as LHeC Test Facility. Its main goals are to demonstrate the LHeC design choices including the multi-turn recirculation with energy recovery, the high-current and continuous-wave operation and to foster the development of superconducting RF at CERN in synergy with a number of internal and worldwide studies for future accelerators.

Its design, based on the one of the LHeC, is composed of two linacs in racetrack configuration, with three recirculating arcs on each side. Each linac is composed by two cryomodules, each hosting four cavities. Three stages have been planned for its completion, they are shown in Fig. 3.22. In the first stage, a single turn with only two cryomodules allows the initial RF testing and energy recovery. In the second stage the additional arcs are added, allowing the investigation of the multi-turn recirculation. In the final stage a second cryomodule is fitted in each linac, increasing the final energy up to 900 MeV.

The reduced size of the machine, whose footprint fits in a 15×45 m^2 rectangle (see Fig. 3.23), does not impede it to reach, at the final stage, a competitive set of beam parameters (collected

Stage 1 – 2 CMs, test installation – injector, cavities, beam dump.
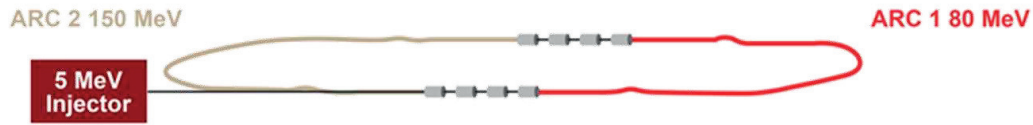
Stage 2 – 2 CMs, set up for energy recovery, 2...3 passes
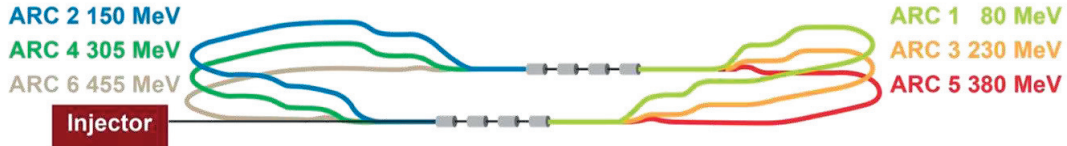
Stage 3 – 4 CMs, set up arcs for higher energies – reach up to 900 MeV
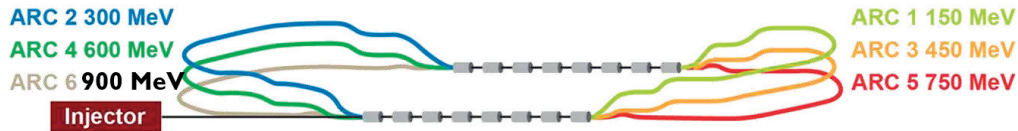
Figure 3.22: The three stages for the construction of PERLE.
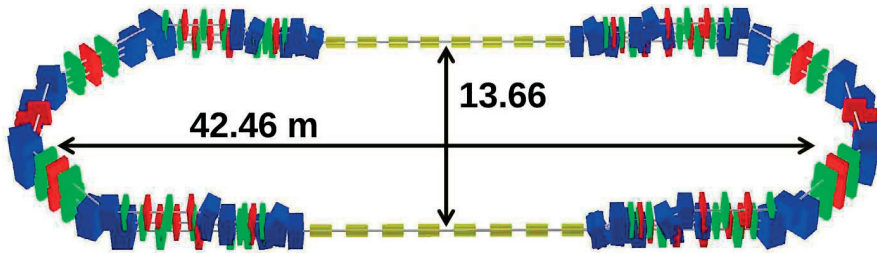
Figure 3.23: Scheme of PERLE, showing the two linacs and the three vertically stacked arcs on each side.

Table 3.9: Fundamental parameters of PERLE

Injection/Dump Energy	5 MeV
Maximum Energy	900 MeV
Normalised Emittance $\varepsilon_{x,y}$	<25 mmmrad
Bunch Length	0.6 mm
Average Beam Current	>10 mA
Bunch Spacing	25 ns
RF frequency	801.58 MHz
Duty Factor	CW

in Tab. 3.9) extending its applications much beyond the testing of the LHeC design and technology. A rich physics programme may come directly with the electron beam, or involving a photon beam obtained by Compton back scattering [11].

3.6.1 End-to-end tracking
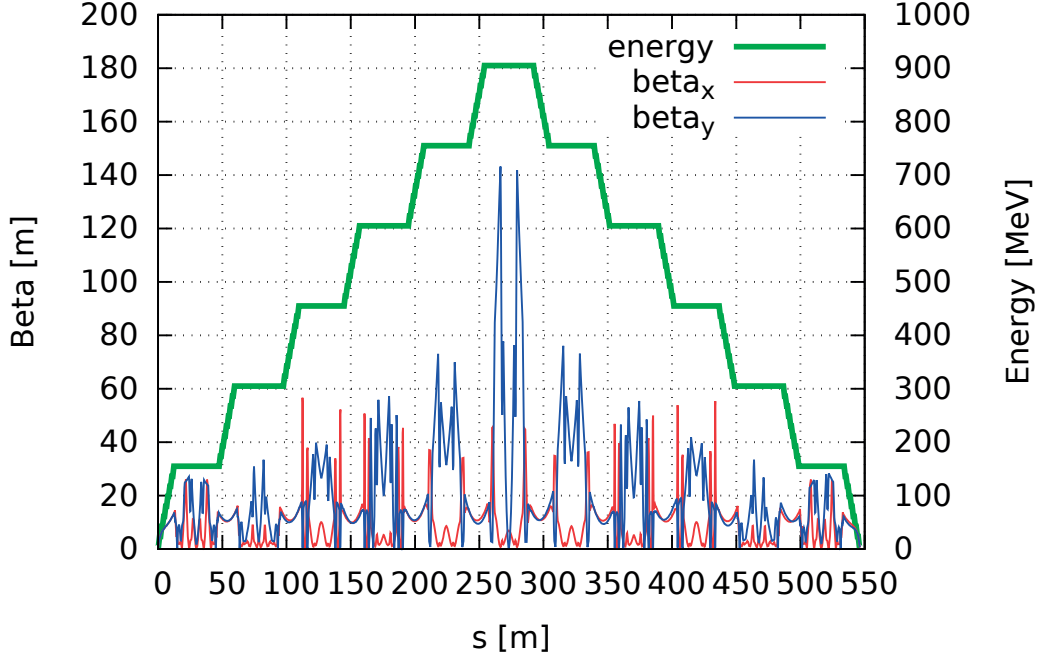
Figure 3.24: Energy and beta function of PERLE, tracked from the injector to the dump, for six turns into the racetrack.

The main contributions to the design of PERLE consist in the arc length matching (to adjust the beam recombination pattern), the end-to-end tracking simulations and the estimation of the BBU threshold current.

In contrast with the LHeC, at PERLE the incoherent synchrotron radiation is very limited due to the much lower energy. Nevertheless the coherent radiation could create issues as the lower beam energy would make it more sensitive to perturbations that are negligible in the LHeC case. Previous simulations of the beam dynamics in PERLE were performed with the tracking code elegant, unrolling the lattice. These studies allowed the evaluation of the impact of the CSR and established a set of beam parameters so that this effect is tolerable [67].

Additional end-to-end tracking simulations have been performed with PLACET2. The large energy gain compared to the beam energy especially in the first passage, requires a proper model of the RF focussing which was implemented and benchmarked against OptiM and elegant. The end-to-end optics obtained with PLACET2 tracking a bunch from the initial condition is shown in Fig. 3.24, the lattice is well matched and symmetric. The good linearity of the phase space was assessed. By calculating the RF phases according to the time-of-flight with PLACET2, issues with the length of the arcs were spotted and corrected, adjusting the on crest acceleration, regularising the spacing between the bunches in the linacs and improving the recombination patter in a similar way as described in Sec. 3.5.2.

3.6.2 Beam Break Up

The much shorter lattice compared to the one of the LHeC, reduces the impedance seen by the beam, but, on the other hand, the much lower energy can enhance beam instabilities. For these reasons studies of BBU were required and have been performed.

The procedure already described in Sec. 3.5 was used to verify the stability of the beam. In addition, as the number of elements in PERLE is much smaller compared to the LHeC, it has been possible to investigate the impact of long range wakefields with a different approach.

A long train of gaussian bunches is injected, each containing 5000 macro particles (as opposed to the LHeC case in which single-particle bunches were used). All the bunches are initially aligned. The excitation arises spontaneously from statistical fluctuation of the distributions of the particles inside the bunches (the same fluctuations that allows for Stochastic Cooling [68] in proton machines). Slightly above the threshold current the instability develops very slowly and the noise in the bunch position makes it hard to detect. Instead, looking at the amplitude of the modes inside a cavity it is possible to identify if one of them is increasing much before its effect becomes visible on the beam. The amplitude of all the 26 modes of one cavity is shown in Fig. 3.25. One can note that when the number of particles per bunch is increased from 10×10^9 to 12×10^9, one mode starts to build up.
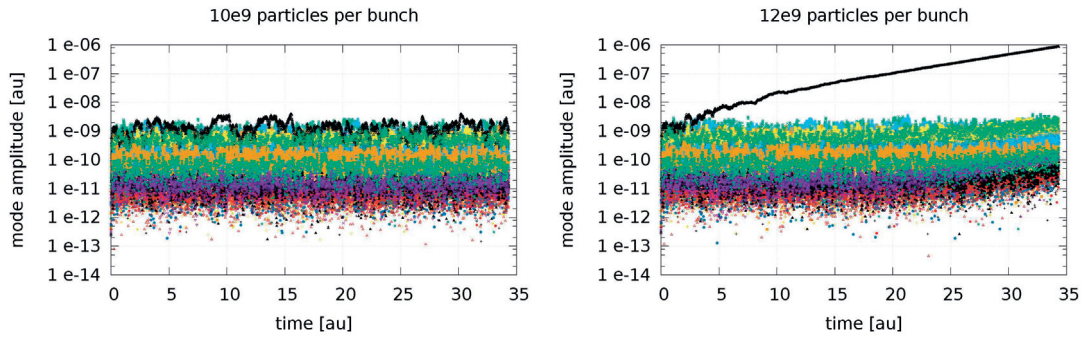
Figure 3.25: Amplitudes of all the 26 modes of one cavity, as many bunches go through it. The detuning is set to 1×10^{-3}.

Due to the fast acceleration from the very low injection energy of 5 MeV, the initial energy spread has only a minor effect on the threshold current. A marginal increase of the threshold current was observed raising the initial energy spread to improbable values. The introduction of additional energy spread from the RF, running the linac slightly off crest, may increase the threshold current in a more realistic way, although this is not required with the current beam parameters.

Detuning

As the number of cavities in PERLE is much smaller compared to the one of the LHeC, the detuning effect has more chances to distribute the frequencies in such a way that the build up of the modes is enhanced. This is particularly true if the detuning parameter is very small. A statistical analysis of the detuning effect for PERLE has been done applying the same technique described in Sec. 3.5.1. A train of single particle bunches, where a single one carried initial action, was tracked, collecting the actions of the bunches at the dump. The results, for different values of detuning, each randomised over 300 machines, are shown in Fig. 3.26. It can be seen how for a detuning of 1×10^{-4} there is a significant number of machines where the excitation is more sustained with respect to the case with no detuning at all. Moreover at PERLE few ill cases that are more prone to show instabilities, are present even with large detuning values such as 1×10^{-3}. However, most of the machines benefits from the detuning.

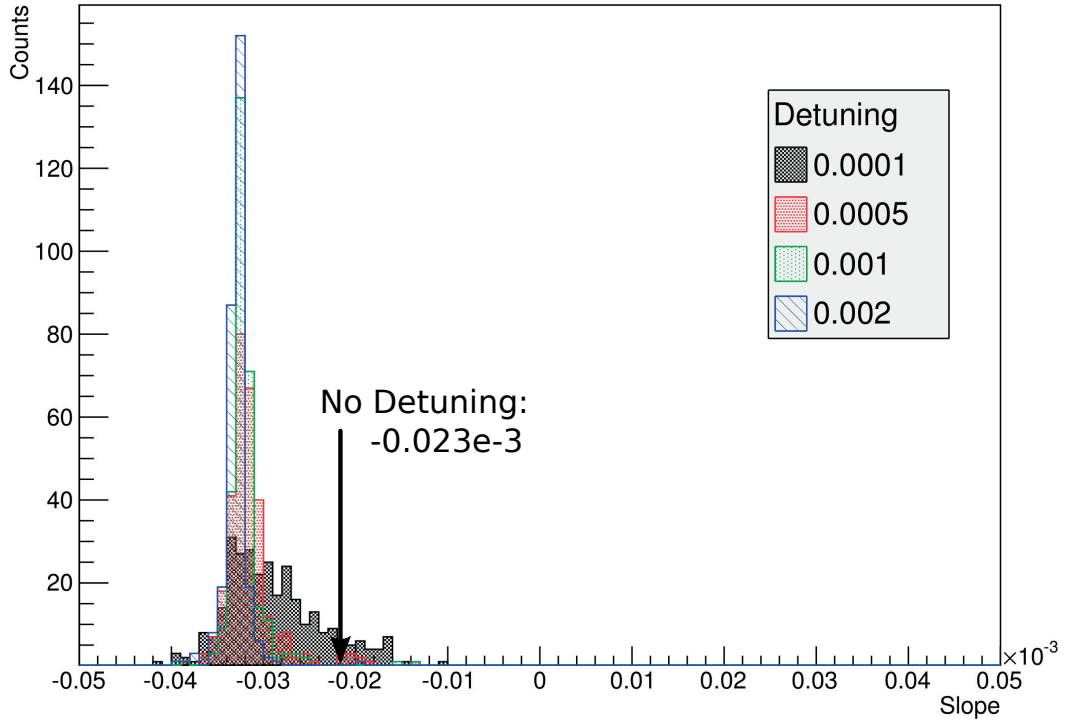Figure 3.26: Distribution of the slopes of the excitation for different values of detuning. Each of them contains 300 randomised machines.

3.7 Conclusions

The LHeC CDR lattice have been imported in PLACET2 and extensive tracking simulations have been performed, validating the ERL operation. The beam-dynamics investigations cover the incoherent synchrotron radiation, the beam-beam effect, and short- and long-range wakefields.

The simulations consist of two steps. Initially a single-bunch, multi-particle, end-to-end tracking was completed aiming at validating the preservation of beam quality at the IP and the feasibility of beam deceleration to the dump. In a second phase the simulation was extended to a multi-bunch tracking, taking into account the continuous operation of the machine and investigating its stability with respect to long-range wakefields coupled to the amplification from the beam-beam effect. The impact of the detuning of the RF cavities, the phase advance in the IP line and the bunch recombination pattern have been investigated.

Following these studies, a number of improvements have been made in the lattice. Beamline sections such as the spreader and recombiner have been redesigned to reduce the impact of the synchrotron radiation while better containing the beta functions. The first design of the detector bypass has been completed. Realistic parameter tables for the RF compensating sections have been compiled.

Concerning the investigated effects, the current design of the LHeC marginally meets all the performance parameters, even in the case of the high-luminosity Higgs Factory. Nevertheless strategies for possible further improvements (enhanced or rearranged focussing in the linacs, arcs based on combined function magnets) have been presented and PLACET2 can be improve to include more effects (like the ion cloud) in the simulation.

The beam dynamics studies have been extended to PERLE: a smaller scale ERL facility. Its design was finalized and its operation was validated.

3.8 Open issues

The complete validation of the LHeC design requires investigations of the ion cloud build up estimating the required gap in the bunch train. This should follow after the implementation of the ion cloud in PLACET2.

The integration of the IP line should be completed, verifying the impact of the additional chromaticity to the transport to the dump.

Tolerances in terms of the field quality, phase stability and alignment should be explored, together with effective correction and feedback schemes, including an optimization of the placement of monitors and kickers.

The path length adjustment with dedicated chicanes have been proven ineffective for the highest energies. A possible solution consists in introducing orbit oscillations in the arcs. The impact and effectiveness remain to be verified.

4 CTF3

CLIC is a study for an e^+e^- collider at the energy frontier based on high-gradient, normal-conducting, accelerating structures [15]. The acceleration of the colliding beams requires very short and intense pulses of RF power which are extracted from a high-current Drive Beam running parallel with the main linac. The Drive Beam is shaped in the Drive Beam Complex where beam recirculation is employed to repeatedly fold a bunch train. This recombination process compresses the bunch train, increasing the bunch frequency and pushing the average current to more than 100 A. The details of why this is required and how this is made possible have been discussed in Sec. 1.2.1.

CTF3 [69], the third CLIC Test Facility, currently operating at CERN, has demonstrated the three fundamental concepts of the CLIC Drive Beam: fully-loaded acceleration [70], beam recombination [71] and power extraction and transfer to the main beam [72]. As shown in Fig. 4.1, CTF3 closely resembles the CLIC Drive Beam, being composed of a linac, a delay loop, a combiner ring and two decelerator modules. A probe beam, generated by the CALIFES accelerator [73], receives the power from the Drive Beam which is decelerated in the experimental area (CLEX).

Comparing the CLIC Drive Beam with CTF3 we find an energy 15 times higher, more than 3 times higher current beams in longer pulses, a recombination factor of 24 instead of 8 and a much more pushed deceleration. It is clear that, although the working principles have been proved experimentally, detailed simulations of the beam dynamics are required to validate the extrapolation from the CTF3 design. This was a further motivation, that adds to the ERL simulations (see Chapter 3), for the development of the PLACET2 tracking code. Although the application of PLACET2 to the CLIC Drive Beam have only been initiated, it has been extensively validated at CTF3 with focus on the Combiner Ring.

The next sections will introduce the CTF3 Combiner Ring Layout and its model in PLACET2. We will see how PLACET2 is capable of reproducing the long-range wakefield instability induced by the RF deflectors. Finally the results of the experimental measure of the Combiner Ring length will be presented, including motivation, methodology and data analysis.

Figure 4.1: Layout of CTF3.

4.1 The CTF3 Combiner Ring

The CTF3 Combiner Ring (CR) is shown in Fig. 4.2. It has two long-straight sections and two short-straight sections connected by four isochronous arcs. One long straight section

beam energy	150 MeV
ring length	$\sim$ 84 m
pulse length	140 ns $\approx$ 42 m
bunch frequency	3 to 15 GHz
bunch charge	2.33 nC
pulse current	up to $\sim$ 30 A
norm emittance	150 μm
energy spread	0.5 %
bunch length	5 mm

Figure 4.2: Magnets layout and main parameters of the CTF3 Combiner Ring.

hosts the two RF deflectors that make the injection possible; a kicker is located in the long straight section on the opposite site allowing the extraction of the recombined train. One of the short straights accommodates the wiggler magnet which is used for length tunings; while the second short straight is currently empty (the possibility to install an RF cavity to ease the ring setup and diagnostics was considered [74], but it has never been the case). The arcs are composed of three dipole magnets, with two quadrupole triplets placed in between. The tuning of the triplets is such that the dispersion has a negative value at the central dipole, therefore suppressing the R_{56}. Three sextupoles families are installed in the ring, they were originally tuned to cancel the second-order momentum compaction T_{566} while containing the chromaticities. Indeed a good chromatic correction reduces the impact of orbit oscillations on the isochronicity [74].

4.1.1 PLACET2 Model

The PLACET2 Model of the CR has been adapted from the MAD-X model broadly available on the CERN SVN repository *ctfmod*. Although the agreement between PLACET2 and MAD-X is excellent, many discrepancies may exist between the model and the real machine. A possible source of issues are the dipole magnets which were initially designed for the LEP-EPA ring [75] and are now operated with a bigger bending angle than originally foreseen. Fringe fields, quadrupolar and sextupolar components were measured [76] and are included in the model,
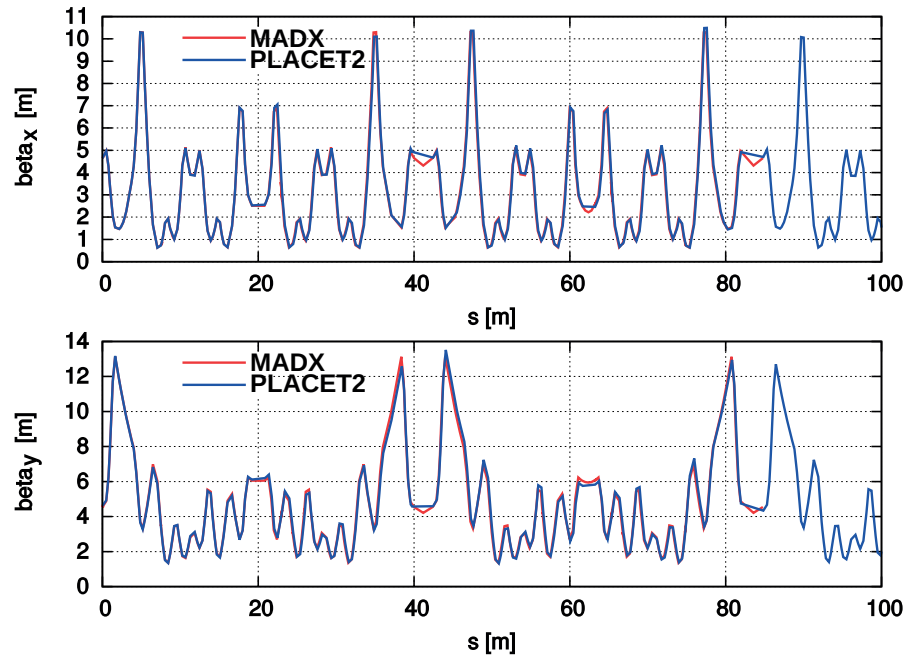

Figure 4.3: Comparison between the horizontal and vertical β functions of the CTF3 CR obtained with MAD-X and PLACET2. Small local discrepancies are just caused by missing data.

but extensive beam-based measures have never been performed. The wiggler magnet, whose only purpose is to vary the ring length, is an additional source of uncertainty as, for simplicity and following the MAD-X, it was replaced with a drift which ignores any focussing and energy dependent effect.

The Twiss functions of the CR are shown in Fig. 4.3, a single turn completing at about 84 m. Figure 4.4 presents the horizontal orbit and dispersion for three turns and a half, obtained with PLACET2. Each of the M-shaped structures in the dispersion function represents one arc (four of them complete one turn). The horizontal orbit profile starts with an injection offset of ~14 mm at the septum magnet. The beam is immediately kicked on the closed orbit by the first RF deflector. The time-of-flight is such that a 90° phase shift of the RF deflectors is introduced at each turn. Indeed at the end of the first turn the beam reaches the RF-deflectors on the zero-crossing phase and no effect on the orbit can be seen. In the second turn the deflectors create an orbit bump opposite to the septum. At the third turn the phase is again on the zero crossing. Half turn later the beam is extracted on the opposite side of the ring. This scheme allows to obtain a factor-four-recombined beam, as shown in Fig. 1.5.

The small amount of dispersion that leaks from the injection could be removed by better matching the dispersion and its derivative in the injection transfer line. The bump at the second turn however is more dramatic, leaking a conspicuous amount of dispersion. This is a known issue of orbit bumps generated with only two kickers: there exists no linear optics system to be placed in between the two kickers that can simultaneously close the orbit and the dispersion [77]. In the CLIC combiner rings sextupole magnets are employed to solve the issue.

4.2 Vertical Instability caused by the RF Deflectors

In this section we will consolidate both the PLACET2 models of both long-range wakefield and the Combiner Ring, reproducing the beam dynamics results presented in [32].

4.2.1 Historical introduction

During the commissioning of the combiner ring, an unforeseen vertical instability appeared. It was characterised by a remarkable amplitude and phase stability from pulse to pulse; a measured oscillation frequency shifted by 48 MHz with respect to the RF frequency; a dependence on the train length and on the bunch charges. The resulting operability of the combiner ring was limited to short trains and low charge. This was a hindrance to the path towards the recombined beam and its deceleration, jeopardising the CTF3 programme.

The typical aspect of the instability as seen with a BPM is shown in Fig. 4.5. A beam of 420 bunches was filling approximately half of the ring. It can be seen that at subsequent turns, the beam vertical orbit becomes wider and wider, while the current is rapidly reduced. The
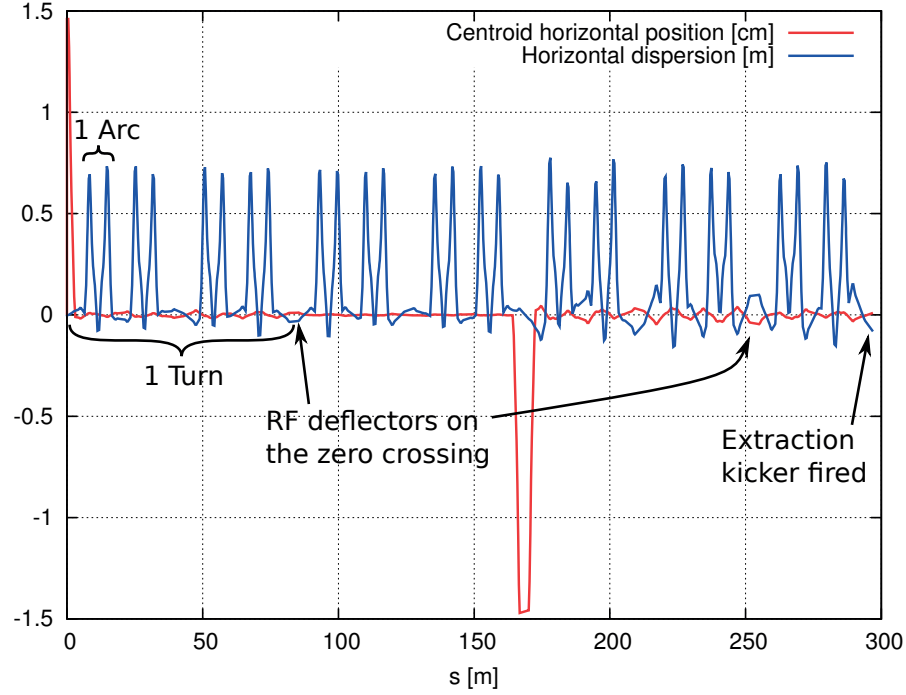
Figure 4.4: Horizontal Orbit and Dispersion for 3.5 turns in the CR. The phases of the RF deflectors are automatically computed by PLACET2 according to the beam time of flight.

phenomenology of the instability, and in particular its frequency, was a strong hint that a possible source were long-range wakefields caused by the RF deflectors. Indeed the CTF3 RF deflectors have two rods that prevent the rotation of the polarization of the horizontal deflecting mode. The dimension and position of the rods shift the frequency of the vertical mode by 45.8 MHz with respect to the bunch frequency. It turned out that this frequency separation, did not impede the beam from deposing power in the vertical mode characterized by a particularly high shunt impedance (see Tab. 4.1). This was made worse by the fact that the power deposed in that mode could not be extracted by the RF couplers which are oriented horizontally.

Table 4.1: Parameters of the offending mode in the original CTF3 RF deflectors

Frequency	3.0443 GHz
Impedance	1.6 MΩ
Q-value	11 500

The vertical instability was later suppressed with an improved design of the RF deflectors. The rods are now closer to the centre to improve the frequency separation of the vertical modes and the deposed power is extracted by means of antennas, dumping the vertical modes on resistive loads. Although it might have been possible to excite an instability disconnecting the loads from the antennas, it would not have been easy to reproduce it with simulations, as such
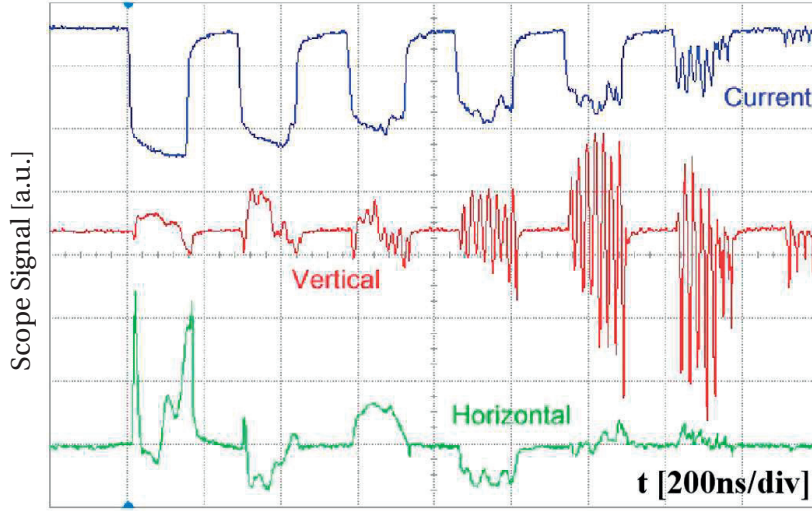
Figure 4.5: Signals from a BPM visualised on an oscilloscope while the instability develops. The beam was filling half of the ring. The vertical position of the beam is excited after a few turns, disrupting the beam.

operation of the new deflectors was never foreseen and neither studied. For this reason we focussed on reproducing the available data collected with the old deflector setup.

4.2.2 Comparison of the results

The data available from the ring commissioning and in particular the simulations published by Alesini [32] were considered. These were performed with a dedicated tracking code which was also used to asses the design of the new deflectors. It takes as input simple optics parameters such as the Twiss values at the deflectors, the phase advances between them (see Fig. 4.6) and the properties of the offending mode and of the beam (bunch charge, number and spacing).
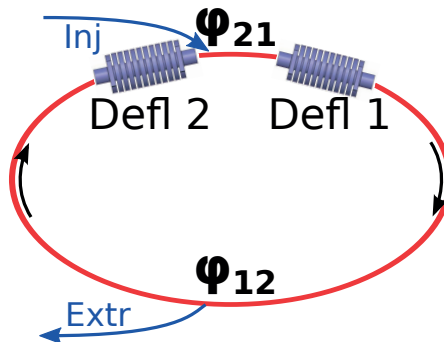

Figure 4.6: Scheme of the CTF3 combiner ring clarifying the positioning of the deflectors and the related phase advances.
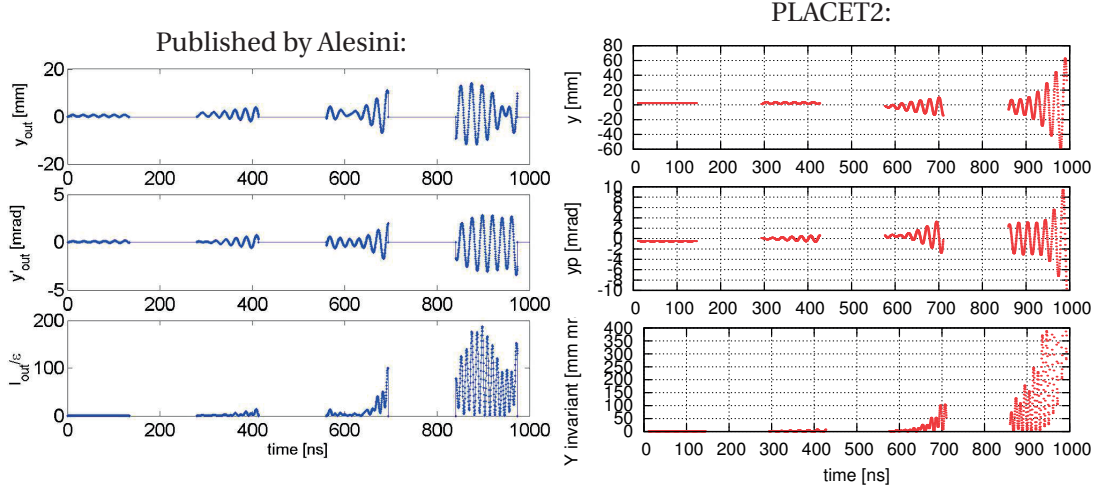
Figure 4.7: First comparison of the development of the vertical instability giving a phase space blow-up. No perfect agreement is expected as the optics parameters used by Alesini do not match the ones in the current model of the CR.

A preliminary investigation aimed at reproducing the instable beam with PLACET2. The mode in Tab. 4.1 was added in the two deflectors and the beam was setup as described by Alesini [32] and summarised in Tab. 4.2. The optics at the deflectors could have been adjusted to the values used by Alesini, for instance by adding extra matrices in the model, however this was not reputed necessary. Indeed, although it is not possible to make a one-to-one comparison, the beam behaviour is very well reproduced in PLACET2 with the beam blow up developing in four turns, as shown in Fig. 4.7.

Table 4.2: Beam parameters used to investigate the vertical instability.

Beam energy	100 MeV
Bunch charge	2.33 nC
Bunch frequency	3 GHz
Bunch number	400
Turn number	4
Train offset at first deflector	1 mm

A more detailed study targeted the dependency of the instability on the phase advances φ_{12} and φ_{21} (see Fig. 4.6). It should be noted that the bump closure requires a horizontal phase advance $\varphi_{x,21}$ multiple of $(2n+1)\pi$, however the instability takes place in the vertical plane, where there are no constraints to the phase advances.

In order to match and scan the phase advances, matrices of the same form of eq. 3.7 were used. Single particle bunches were tracked. The final Courant-Snyder invariant was averaged

over all the bunches in the train:

$$J_y = \langle \gamma y^2 + 2\alpha y y' + \beta y'^2 \rangle, \tag{4.1}$$

and normalised with respect to the initial one. In Fig. 4.8 the results of the phase scans with the full ring model are compared with the one obtained by Alesini [32], showing a remarkable agreement of the two independent studies. The vertical phase advance φ_{21} currently in the machine is 70°, the influence of φ_{12} in this case is shown in Fig. 4.9. One can note that, although maxima and minima still exists, in this case the amplification always remains well above 100. The new deflector design was therefore required to operate the machine.
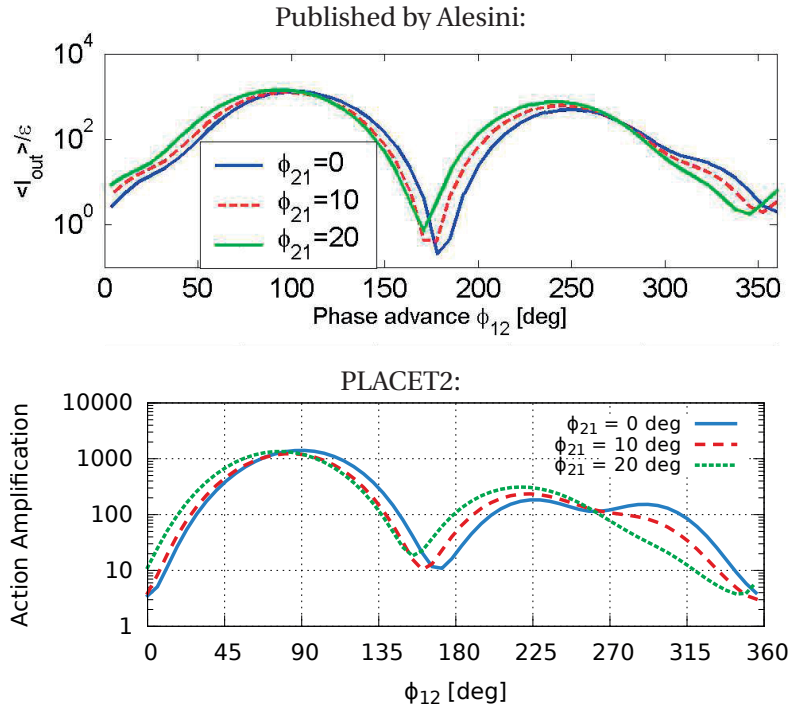
Figure 4.8: Action amplification caused by long range wakefields in the deflectors, as function of the phase advances between them. The results simulated and published by Alesini while investigating the instability [32] (top) are compared with the ones obtained with PLACET2 (bottom).

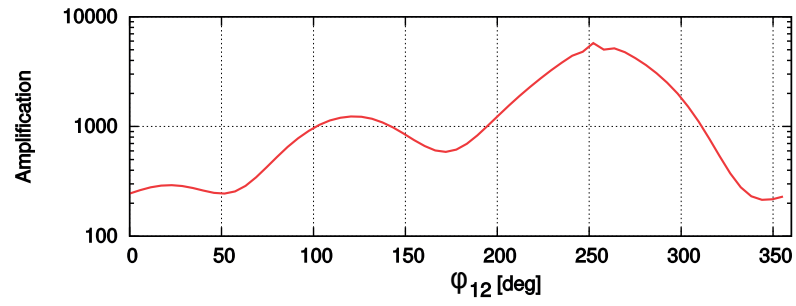Figure 4.9: Action amplification caused by long range wakefields in the deflectors for $\varphi_{12} = 70°$ (as naturally in the ring) obtained with PLACET2.

4.3 Orbit length measure at the CTF3 Combiner Ring

4.3.1 Motivation

The length of the CTF3 Combiner Ring (CR) plays a critical role in determining the quality of the combined train of bunches. Errors in the ring length cause a phase error which impacts on the efficiency of the energy transfer from the drive beam to the main beam.

At CTF3 the length of the CR can be tuned in the range of few centimetres employing a wiggler magnet. Here we want to investigate the impact of an optics detuning on the length of the ring. In particular we want to assess the possibility to obtain a ring shorter than the one with the wiggler off. As all the dipole magnets in the ring are connected in series, they can only be adjusted at the same time. This limits the margin of intervention, nevertheless acting on the dipole currents in conjunction with the quadrupole currents it is possible to find machine configurations that effectively alter the length of the ring. In particular the ring can be shortened in two ways:

- increasing the strengths of the dipole magnets *and* reducing the strengths quadrupole magnets;

- reducing the strengths of the dipole magnets *and* increasing the strengths quadrupole magnets.

The first approach uses the dipole to shrink the orbit and at the same time relaxes the quadrupoles to avoid excessive oscillations due to the mismatch. The second approach is characteristic of the arcs lattice. Each one of them contains three dipole magnets. When a particle travels through the first relaxed dipole, it moves outwards, the stronger quadrupole triplet then focuses it back inward at the central dipole, where it cuts the path by a substantial amount.

Both of the approaches have been verified with PLACET2 and are presented in Fig. 4.10. A positive horizontal offset means that the beam moves outwards, while the longitudinal position becomes negative when the beam anticipates with respect to the ideal orbit. The strongest variations of the longitudinal position take place in correspondence of the dipole magnets, according to the beam offset.

4.3.2 Methodology

In order to perform a beam-based measure of the ring length, the beam was kept circulating for approximately 100 turns. This particular operation scheme is achieved adjusting the timing of the RF pulse to the first RF deflector so that after the initial kick, the deflector does not receive any power and does not affect the beam at the subsequent turns. At the same time the activation of the extraction kicker is delayed with respect to the normal machine operation.
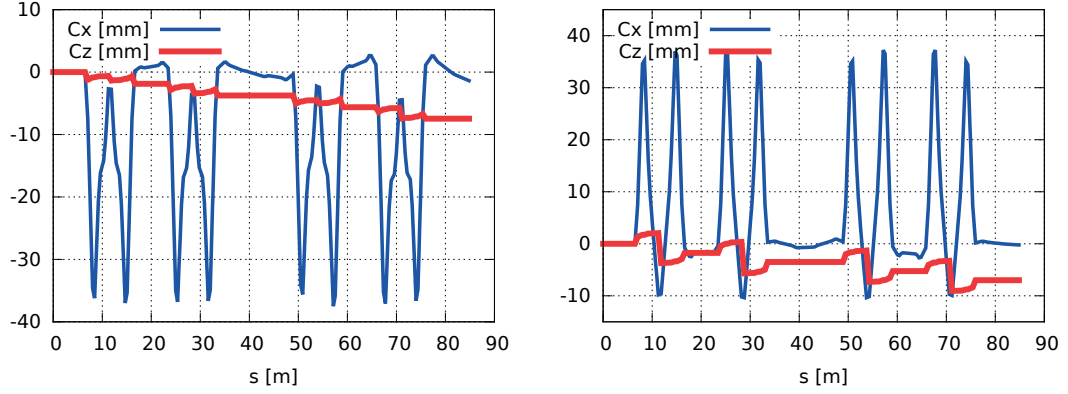
Figure 4.10: Bunch centroid horizontal and longitudinal positions when quadrupoles are relaxed and dipoles are strengthened (left) and when dipoles are relaxed and quadrupoles are strengthened (right).

The ideal beam for this measure consists of a 3 GHz beam from the gun, bypassing the delay loop and therefore being less perturbed. Multiple train lengths were tested: from 140 ns, filling half of the ring, to an almost completely filled ring; without noticing remarkable variations. Good transmission and orbit closure in the CR are routinely achieved over four beam turns. However no tools are in place to optimise the long term storage in the ring and we had to accept some beam degradation.

The time resolution of the BPMs installed in the ring is not enough to distinguish the different bunches in the train, therefore the BPMs return a flat signal when the beam passes through, interleaved with no signal when the beam is on the opposite side of the ring as shown in Fig. 4.11. A Fourier Transform, eventually improved with a NAFF[1] algorithm [78], of a BPM signal gives the revolution frequency in a straightforward way. However the limited time resolution and number of turns, impact on the accuracy of the ring length extracted in this way, preventing the observation of variations at the centimetre scale and below.

4.3.3   BPR

To improve the accuracy of the measure, a phase monitor, or BPR, is used instead of a BPM. BPRs allow a much more accurate determination of length variations (but not of the absolute length), requiring a more elaborate data analysis. A BPR consists of a button pick-up which multiplies the beam-induced signal by an internal reference sine function, in our case f_{ref} =3 GHz. The resulting signal is shown in Fig. 4.11.

The BPRs are routinely used to monitor the spacing of the bunches along a train. Indeed it is possible to adjust the phase of the internal reference so that the head of the train arrives

---

[1]The Numerical Analysis of Fundamental Frequencies consists in improving the position of the peak frequencies, identified for instance by an FFT, by finding the local maxima of the Fourier integral.
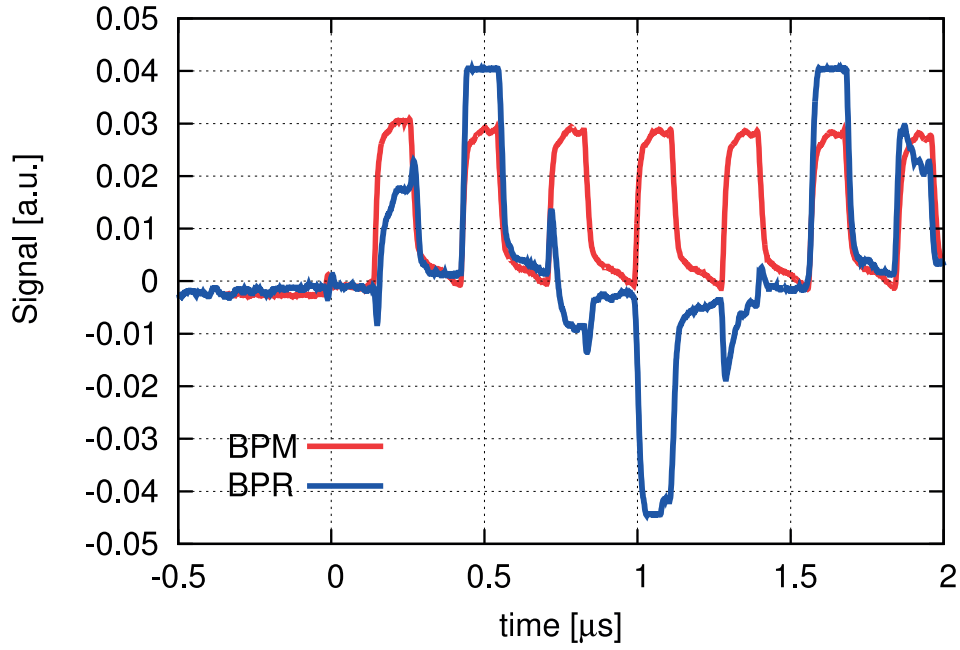
Figure 4.11: Sample of signals from a BPM and from a BPR. The beam fills half of the ring and 7 turns are shown. While the BPM signal presents a periodic structures, the BPR one is modulated according to the beam phase.
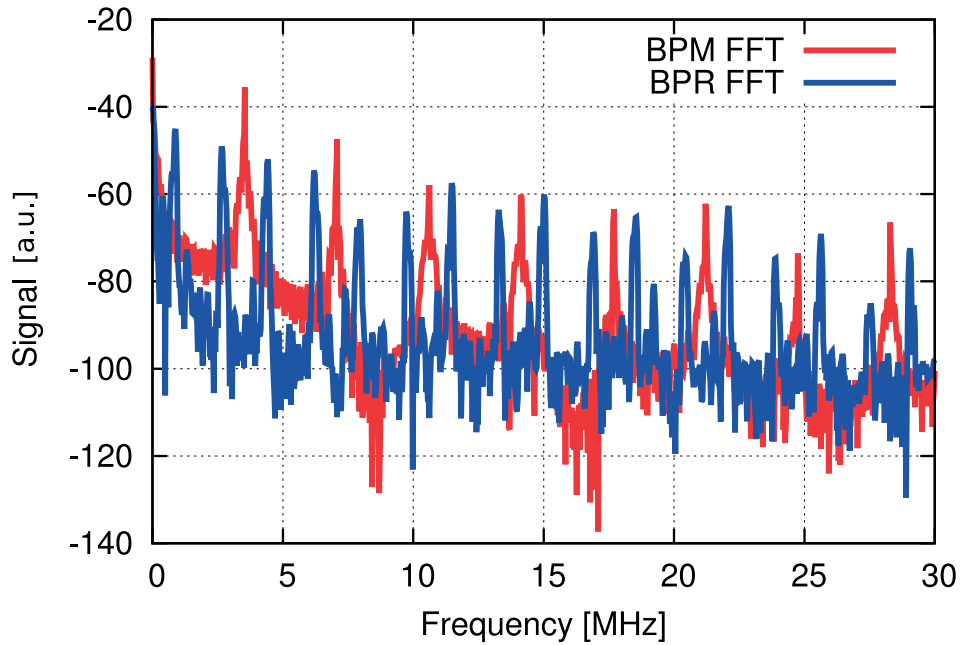

Figure 4.12: FFTs of both the BPM and the BPR signals. The first shows the revolution frequency and its harmonics. The second presents the sidebands whose positions depend on the phase slippage with respect to the internal 3 GHz carrier.

on one of its zeros. While a perfect train in such condition would be invisible to the BPR, cumulative errors in the bunch spacing become clearly visible, although, as for the BPMs, single bunches are not resolved.

Tuning the BPR phase so that the first bunch hits a maximum of the reference, the output signal is similar to the one of a BPM, given that the beam time of flight is a multiple of the BPR frequency. For different times of flight a modulation is introduced in the output signal. In the frequency domain the revolution frequency, f_{rev}, and its harmonics split into sidebands (shown in Fig. 4.12) whose distance, d_s, depends on the phase slippage and is connected to the fractional length, L_f, of the ring:

$$L_f = \pm \frac{d_s}{2 f_{rev}} \frac{c}{f_{ref}}. \tag{4.2}$$

When the phase slippage is 180° the sidebands cross themselves at intermediate points with respect to the harmonics of the revolution frequency (see Fig. 4.13). In general the separation of the sidebands becomes smaller when we move towards an integer value of the fractional length, but since we can approach it both from above (decreasing the length) and from below (increasing the length), the sign of the expression is not immediately clear if the starting point is not know a priori. In our case the minus sign has been determined using the wiggler magnet which gives an unequivocal contribution to the length of the ring.

The measure has been done collecting the signal of the BPR with an oscilloscope and saving the trace. Although the oscilloscope had to be operated manually, it offered much more samples than the available ADCs, allowing to acquire the signal for long times while keeping a high sampling frequency.

BPR simulation with PLACET2

Initially the simulated length of the ring was extracted from the centroid position of the tracked bunch. Later improvements included the reconstruction of the BPR signal. The BPR in PLACET2 slices the beam longitudinally. The charge value in each slice is multiplied by the reference sinusoidal function, obtaining the ideal signal. If a time resolution is specified, the ideal signal is convoluted with a normalised gaussian[2] having σ equal to the resolution. The signal may then extend in time and overlap with the one coming from other bunches, making them indistinguishable. A sampling time, or frequency, can also be introduced.

Figure 4.14 shows the simulated effect of the BPR time resolution. The bunch train is composed of 20, 5 mm long bunches, followed by 1, 1 mm bunch and finally 20, 5 mm bunches on the opposite phase at 3 GHz. All the bunches have the same charge. The first BPR has a resolution of 20 ps, it resolves single bunches and it also notes that the central bunch is shorter. The

---

[2]In case of time dependent signals, convolutions with a gaussian lead to causality violation, an exponential decay function may be more suitable.
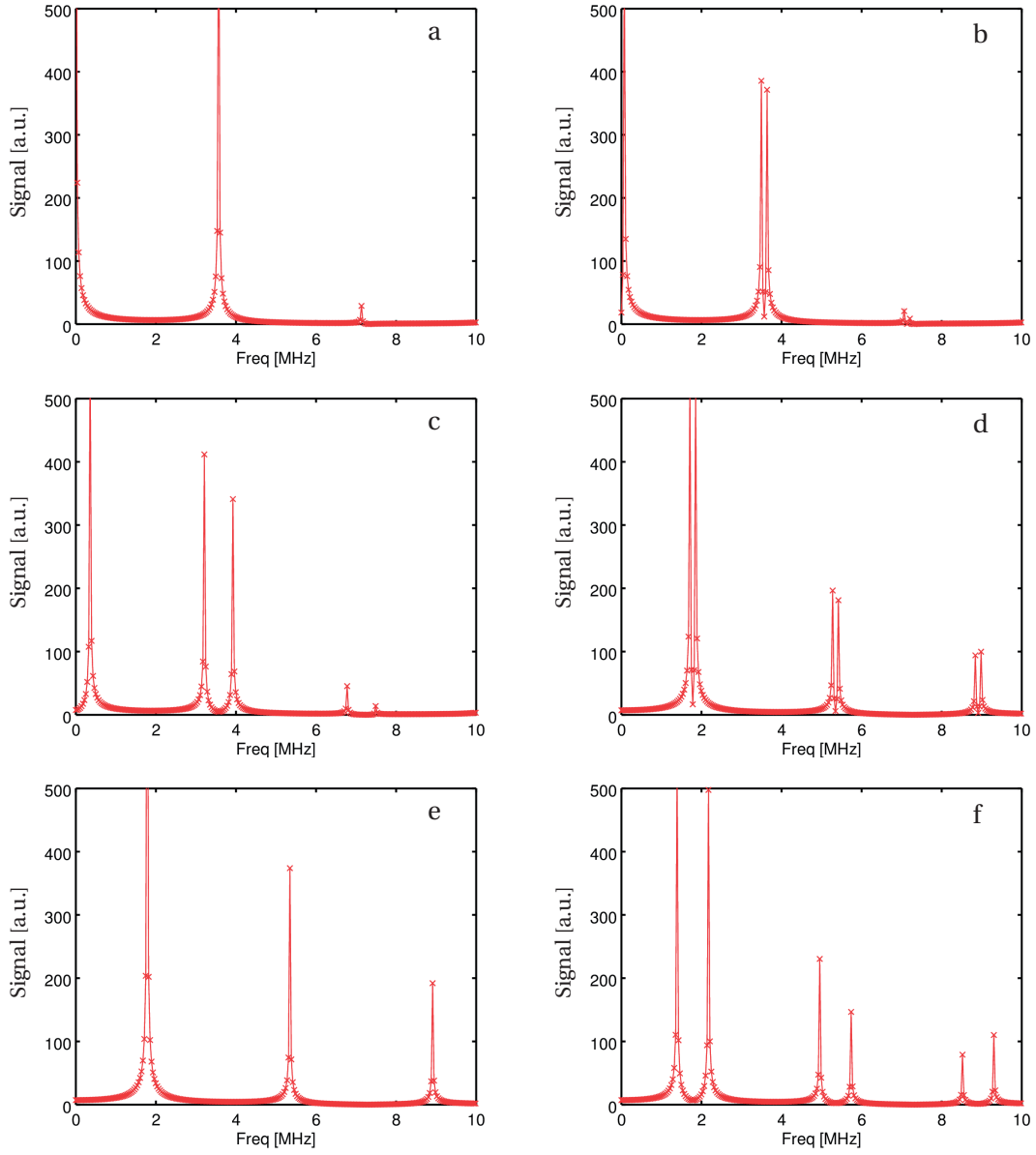
Figure 4.13: Simulated frequency spectra showing the sidebands response to variations of length of the ring. With a null fractional length only the revolution frequency is visible (a). When the length is increased the sidebands appear (b) and separate (c). They approach (d) and cross each other for a phase slippage of π (e), and they continue (f).

resolution of the second BPR is 1 ns, more similar to the ones at CTF3, therefore it only sees the average bunch phases. The sampling time is the same as the resolution. Samples of the signal are identified by the small crosses.
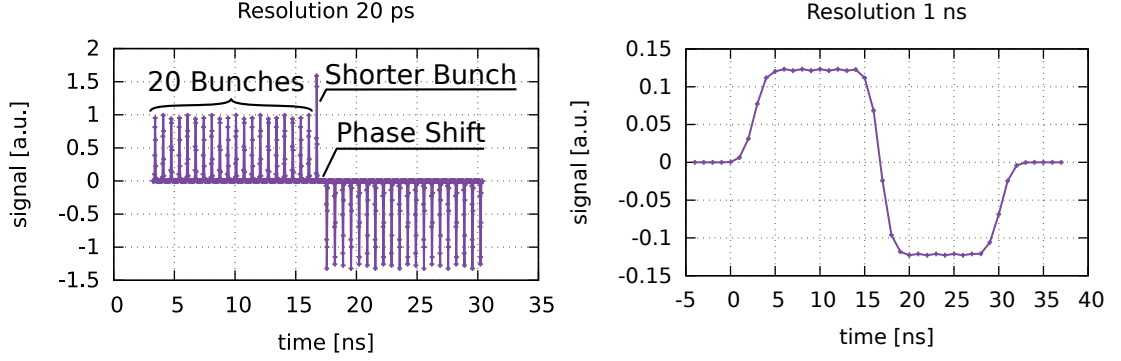

Figure 4.14: Test signals being simulated by the PLACET2 implementation of two BPRs with different time resolutions.

It should be noted that the output of a simulated BPR element can be analysed applying the same program (see Sec. 4.3.4) used for the real data, helping to spot bugs and potentially improving the agreement.

4.3.4 Spectrum Analysis

The traces saved with the oscilloscope are CSV files containing a header (including some general information such as the number of samples, the date, the units, ...) and two columns, each row being a sample of the signal.

As many traces were acquired a small C++ program based on the GSL library was written to completely automatise the analysis of the raw data. The program reads the data from all the files passed on the command line. It then applies the FFT and the logarithm, to better evidence the peaks over the background. The background is fitted with a moving average filter on a big number of samples, which completely cuts out the peaks.

The expected variation of the length are of the order of millimetres, much smaller than the 10 cm wavelength at 3 Ghz, therefore the sidebands preserve their approximate positions. This allows to fill out a list of the expected peak positions. The actual peak frequencies are searched in intervals centred around each point of the list. When the maxima are found, if they are enough separated from the background, the peak positions are refined fitting a parabola over few neighbouring samples, otherwise they are discarded.

At this point the sidebands are reconstructed, discarding the peaks with a missing companion. The distances between the available sidebands are computed. The best estimation is obtained discarding the values outside $\pm 2\sigma$ before averaging them and using σ as uncertainty estimate.

A very similar procedure can be used also to extract the revolution frequency, dividing the average values of each sideband by the harmonic number and proceeding as before to get the best estimation and its error. However the sensitivity is not enough to discriminate the extremely tiny variations[3] in the revolution frequency, therefore it can be set to the nominal value, eliminating a source of uncertainty, at the price of introducing a tiny systematic error.

Finally the fractional length is obtained applying eq. 4.2 and propagating the error.

When the code is fed with multiple files it outputs a table where the length is coupled with the value of the ring property being scanned, extracted from the raw file names. When only a single file is given the analysed spectrum as shown in Fig. 4.15 is plotted on the fly by means of gnuplot-iostream [79], making therefore easy to check if the program has been correctly tuned to operate both on the best looking spectra and on the weakest ones.
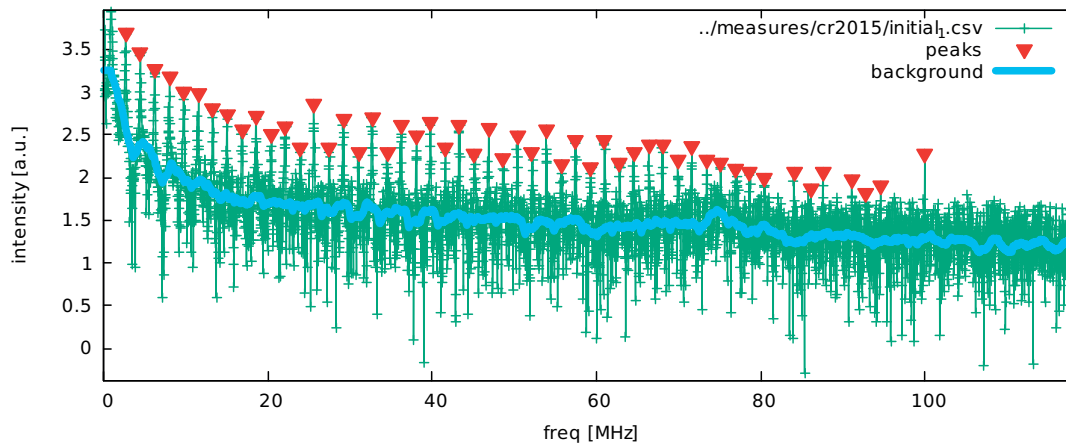
Figure 4.15: Spectrum analysed with the C++ program. The red triangles show the peaks identified. The algorithm discards the peaks too close to the background and the missing sidebands.

4.3.5 Impact of Beam Losses

Beam losses are never desired at any accelerator, however partial, distributed losses are tolerated at CTF3 for small period of time; as the low energy (~150 MeV) and repetition rate (1 Hz) do not pose concerns neither for machine protection, nor for radiation protection. With the extreme optics detuning and mismatch considered, part of the beam is sometimes lost. When this happens the centroid may move longitudinally (see Fig. 4.16), introducing a systematic error. It is therefore important to understand how losses take place and include them in the simulation. Two mechanism leading to beam losses have been identified: injection of a beam partially outside the energy acceptance of the machine and betatron mismatch blowing up the beam at the injection/extraction septa. The two causes are easy distinguished:

---

[3]of the order of $1\,\text{mm}/84\,\text{m} \approx 0.001\,\%$

while the losses produced by the first are immediate (most of them take place already in the first arc), the betatron mismatch induces much slower losses which extend over multiple turns. Figure 4.17 shows a case in which both loss mechanisms are present.
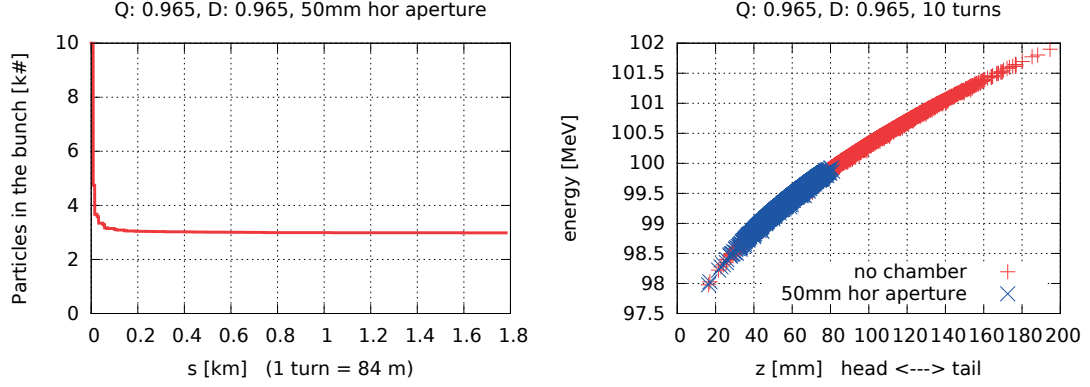
Figure 4.16: Beam losses when both dipoles and quadrupoles have a reduced strength. The high energy part of the beam falls outside the ring energy acceptance and is lost. When this happens the centroid moves forward.
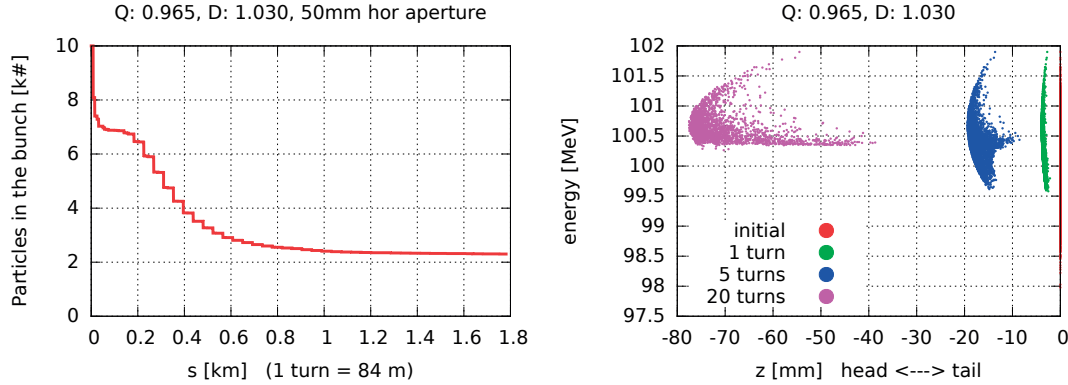
Figure 4.17: Beam losses when dipoles are stronger and quadrupoles weaker. Fast losses of particles outside the machine energy acceptance still take place, but in addition slow losses caused by the betatron mismatch at septa are present.

In PLACET2 physical apertures have been added to the quadrupoles in the arcs and to the injection/extraction septa. The actual beam pipe of the CTF3 arcs is rectangular, the dimensions are $90{\times}37 \, mm^2$. In the simulation a chamber of $50{\times}37 \, mm^2$ has been used, while the septa are placed at 10 mm from the beam. The smaller aperture compensates for the orbit errors coming from element misalignments whose actual values can not be included in the model. A careful tuning of the apertures (especially the one at the injection septum), together with the beam energy spread, can lead to a very good agreement of the simulated transmission with the intensity signal from a BPM, see for instance Fig. 4.18. However it has not been possible to

find a single tuning matching all the loss profiles acquired with different optics scalings. An average configuration was used.

Q: 102.4%, D: 97.6%
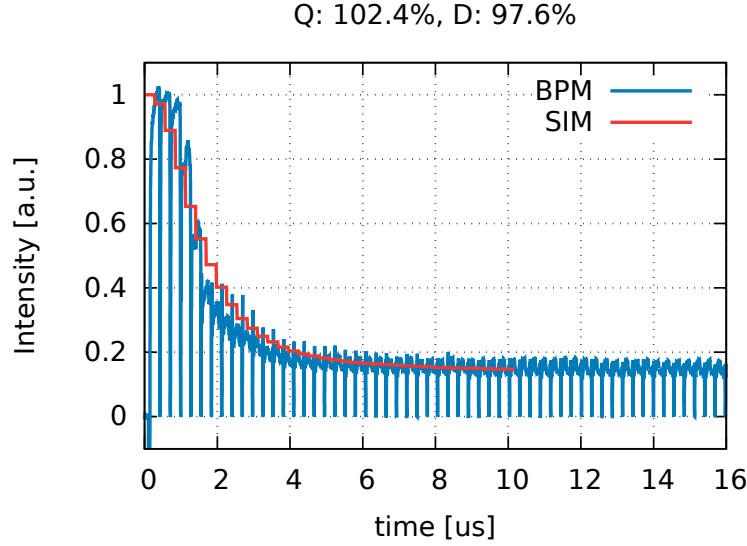
Figure 4.18: Measured losses over multiple turns in the Combiner Ring with scaled optics: Quadrupoles at 102.4%, Dipoles at 97.6%. The ring is almost full and the gaps in the BPM signal (blue line) can be used to identify subsequent turns. The red line represent the total number of particles in one bunch tracked with PLACET2.

4.3.6 Wiggler

The wiggler magnet is installed in one of the short straight sections of the ring and allows for length tuning. Increasing the current of the wiggler magnet causes beam oscillations and extends its time of flight. As the effect of the wiggler is straightforward, scanning it allows to validate the setup and the analysis, determining the sign of eq. 4.2 (minus in our case).

The results of the measures of the length dependency on the wiggler are presented in Fig. 4.19, superimposed to the ones in [80]. The two sets of data have a distance of several years, with many machine shut downs and realignment campaigns in between. The difficulty to reach the length required for a combination factor 4 was observed by the operators in a previous run and is confirmed by the new measure. This further justifies the investigation of the possibility to reduce the ring length acting on the optics.

4.3.7 Optics Scan

While scanning the strengths of the dipole and quadrupole magnets, the wiggler was kept at the nominal value in order to take advantage of its focussing effect to improve the transmission. The values of the fractional length of the Combiner Ring are collected in Fig. 4.20. Going from
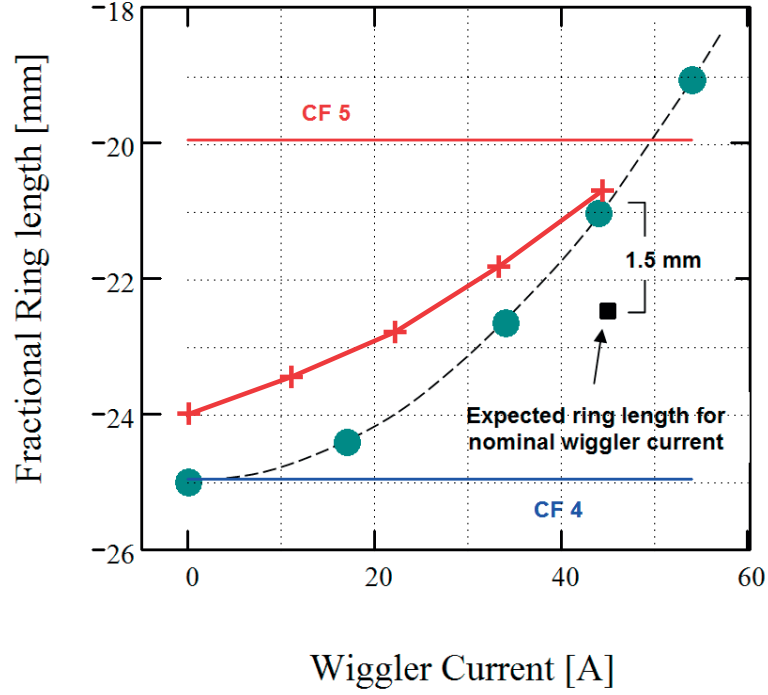
Figure 4.19: Effect of the wiggler current on the ring length. The red crosses are the new measurements, the blue dots are found in [80].

top to bottom one can see the ideal length, obtained from final longitudinal coordinate of the tracked bunch, the length reconstructed from the simulated BPR signals, and finally the measured data.

One can clearly see that the Combiner Ring is shortened as expected when one of the magnet families is relaxed and the other one is strengthened (see also Fig. 4.10). A more surprising result is the almost total absence of response to conjunct scaling of both the families, which mimics an energy mismatch. Indeed, while the optics cancels the T_{56} terms of the transport matrix, making the ring isochronous at the first order, with all the sextupole magnets switched off (as was the case during the measure, although some residual magnetization of the iron core could have been present) a relevant second order effect is expected. The contribution from the T_{566} are evident not only in the simulated plots in Fig. 4.20, but also in the phase space of the tracked bunches and is mentioned in the original design of the ring [74] as shown in Fig. 4.21.

Additional measures have been taken varying the beam energy in order to measure the T_{566}, but even those did not show the expected trends. As of today a main cause has not been identified yet.
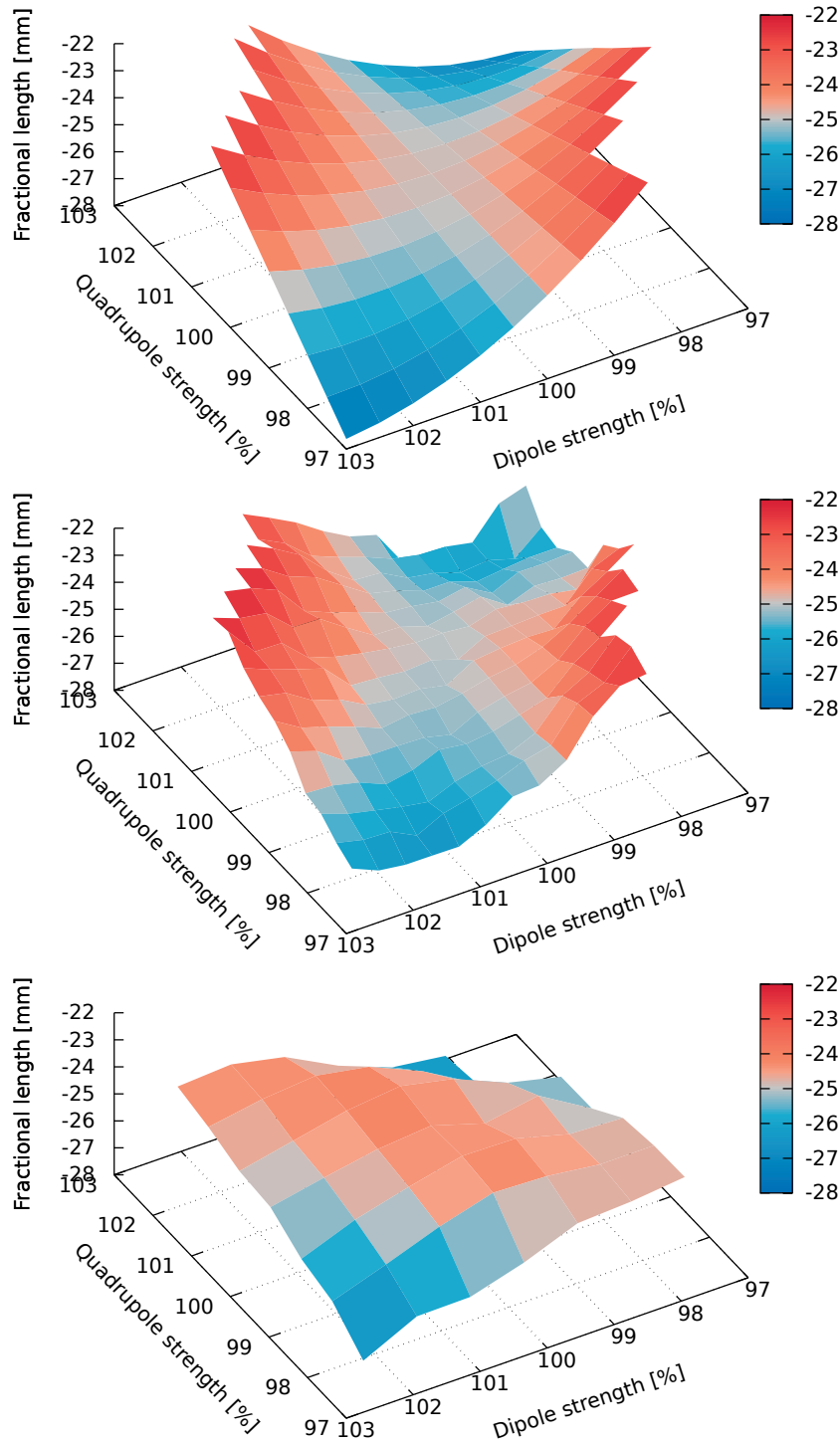
Figure 4.20: Surface plots of the ring length as function of the strengths of all quadrupoles and all dipoles in the ring. The top plot is obtained from the centroid of a tracked bunch, the middle plot is constructed from the simulated BPR signal, the bottom plot shows the data measured on the machine
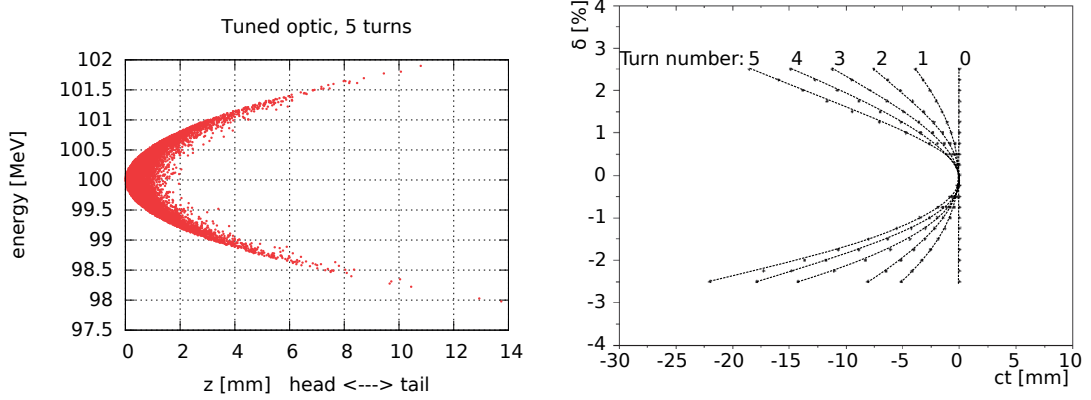
Figure 4.21: Effect of the second order momentum compaction T_{566} simulated tracking a bunch with PLACET2 (left) and from the design reports of the CR (right). The horizontal axis is inverted.

4.4 Conclusions

The work at CTF3 articulated in two phases. Initially the state-of-the-art model of the Combiner Ring was imported in PLACET2, reproducing the MAD-X observables. The automatic handling of time dependencies allowed to simulate the injection and the different bumps at subsequent turns according to the phases of the RF deflectors, evidencing the generation of spurious dispersion routinely observed in the ring. Additional studies related to a multi-bunch instability, that appeared during the first commissioning of the ring, were performed and are in agreement with previous investigations. This enforces the results obtained for the LHeC.

The second phase focussed on experimental measures on the Combiner Ring. A setup composed of a phase monitor, an oscilloscope and an analysis program, was put in place to measure the beam time of flight in the ring, therefore extracting its length. The effectiveness of the setup was confirmed by measuring the ring lengthening caused by the wiggler magnet. The possibility to further reduce the ring length by means of optics detuning was investigated and confirmed. However, this comes with strong optics distortions and often causes partial beam losses. Shall this feature be incorporated in the CLIC design, care should be taken in order to properly size the vacuum chamber and avoiding to power all the dipoles in series, therefore allowing the implementation of more effective schemes.

While the ring shortening comes with a crossing of the dipole and quadrupole strengths (one is increased and the other is decreased), a conjunct scaling is expected to produce a ring lengthening following from the second order momentum compaction, T_{566}. While this was reported in the design documents and was predicted by PLACET2, it was not observed in the machine even with a dedicated search by varying the beam energy. After much effort spent in trying to identify possible causes without finding a definitive solution, the decision to stop the investigation was taken [81].

5 PLACET2

The complexity of both the topology and the operation of recirculating machines makes traditional tracking codes like MAD [82] or elegant [83] unsuitable. Their description of the machine as a sequence of elements and/or the adoption of a rigid definition of the beam does not allow to describe a recirculating machine in a natural way. Single-bunch simulations can still be pursued unrolling the lattice, however the evaluation of multi-bunch effects, which may be critical, is not feasible. Other studies, like the introduction of lattice imperfections, can be difficult.

The BMAD library [84], developed at Cornell University, offers a powerful set of C++ functions which have been used to simulate the beam break up for the Cornell ERL [85]. No conceptual hindrance seems to exist in the extension of these simulation to other lattice topologies, like the one of the CLIC Drive Beam, nevertheless this has never been attempted [86]. Instead, we decided instead to take advantage of the experience maturated with the development, maintenance and operation of the PLACET tracking code [87] to approach the problem.

The original PLACET code was written by Daniel Schulte in the late nineties. PLACET easily deals with high energy machines composed of hundreds of thousands of elements, being very efficient both in memory management and in computation. It was not only used to perform many of the beam dynamics studies and optimizations for CLIC and ILC, but it was also successfully tested on machines like FACET (SLAC), ATF2 (KEK) and FERMI (ELETTRA Sincrotrone Trieste). It allowed many critical studies such as Beam Based Alignments [88], ground motion and feedback systems [89], allowing to contain the emittance dilution during the acceleration and transport of the beam.

The new version PLACET2 introduces new concepts which allow to set up realistic simulations of recirculating machines and of their operation. A new tracking core has been entirely written from scratch in the latest C++ standards. Efforts are being taken to implement the same physics effects handled by PLACET and more. In the next sections we will give an overview of the newly developed concepts and up-to-date code functionalities that provide to our users a powerful tool to tackle these rising challenges in accelerator physics.

5.1 Overview of the Features and Functionalities

PLACET2 is a tracking code for ultra relativistic particles developed with a wide spectrum of machines in mind, such as ERLs like the LHeC [1], but also peculiar lattices like the CLIC Drive Beam Complex [15]. The lattice description, the setup of the beam, the tracking and the retrieval of information are handled in a simple, but realistic way.

PLACET2 offers a great tunability of the trade-off between speed and accuracy. On one hand the beam can be represented using multiple models, on the other hand the lattice is implemented in an innovative way that allows to split the body of thick elements in order to insert the desired physical effects at the required computational precision.

PLACET2 tracks many bunches simultaneously in recirculating lattices. The bunches enter each beamline in the correct time sequence, even in presence of beam spreading and recombination. This makes it possible to compute multi-bunch effects.

The most common accelerator components are implemented in PLACET2, including time dependent ones. They can be misaligned and have apertures, with the possibility to track losses. Physical effects currently include the synchrotron radiation, long and short-range wakefields, while CSR and ion cloud are planned additions.

With a bunch-based beam structure, the beam properties can be computed and/or reconstructed in any location of the simulated machine, according to the bunches that reach that spot. Moreover it is possible to set up a bunch to collect its parameters such as orbit and Twiss, along its whole path in the machine.

Although PLACET2 is entirely written in C++, a TCL scripting interface similar to the one of PLACET is provided using SWIG [90]. Recently a minimal Octave interface has been added following the mechanism developed for PLACET [91]. Through the Octave interface a number of optimizations can be performed leveraging the Octave builtin functions.

5.2 Conventions

PLACET2 maintains the original PLACET conventions, adopting a standard set of coordinates: (x, x', y, y', E, z), in the co-moving reference frame, where:

$$x' \equiv \frac{\mathrm{d}x}{\mathrm{d}s} = \frac{P_x}{P_z} \approx \frac{P_x}{P_0} = p_x, \tag{5.1}$$

$$y' \equiv \frac{\mathrm{d}y}{\mathrm{d}s} = \frac{P_y}{P_z} \approx \frac{P_y}{P_0} = p_y. \tag{5.2}$$

E is the total energy. The longitudinal axis z is oriented toward the tail of the bunch, therefore the head has typically a negative z. The coordinate $s = ct$ is commonly used to describe the bunch position along the lattice, it refers to an ideal particle travelling with speed of light on

the ideal trajectory, therefore particles performing betatron oscillation will slowly lag behind, drifting toward positive z.

The units generally follows the International System, except where High Energy Physics units are more convenient, eg. the energy is generally expressed in eV or GeV.

5.3 Components of PLACET2

PLACET2 adopts an intuitive way to describe a machine based on traditional concepts, but with expanded capabilities and new elements such as injectors, dumps and joints, which allows to simulate the recirculation. The next sections will introduce the main components of PLACET2.

Beam

PLACET2 represents the beam as a collection of bunches. Bunches can be routed independently through multiple beamlines, and their temporal sequence is preserved where the beamlines join. PLACET2 is designed to support many bunch models: e.g. the single particle and the many particle models are already implemented. Each particular bunch model can be treated differently in various situations: for instance the synchrotron radiation for the many-particles bunch is a stochastic process, while the average energy loss is applied with the single-particle bunch. Each bunch has an internal timer which is used for the synchronisation of the tracking, but also to update time-dependent elements (phase, damping, ...).

Machine

The machine is the core concept of PLACET2. It is the collection of beamlines, injectors, dumps and joints plus the methods to create and manage all of them. An important component of the machine is its internal timer, necessary to synchronise the tracking. The creation of a machine is always the first step in a PLACET2 script.

Beamlines

Beamlines are standard, linear sequences of elements. PLACET2 supports the creation of many beamlines, each of them is defined appending the elements after each other. Elements can be added specifying their properties in line (like in PLACET), or being copied from previously defined models (like in MAD). To improve the interoperability, beamlines can be constructed from the MAD Twiss table. Girders are supported. The extremities of each beamline must be connected through joints to an injector, to a dump and/or to other beamlines.

Injectors

Injectors are special elements that allow to define the list of bunches to be tracked. The creation of an injector is very similar to the one of a beamline, where bunches plays the role of elements. Bunches can be appended one after each other specifying their properties, including their time distance from the previous. If many equal bunches are to be tracked, the injector can automate the copy with memory efficient routines. During the tracking, the injectors release bunches as time goes.

Dumps

Dumps are very simple elements that terminate a line. When a bunch reaches a dump, it is destroyed. Dumps can be instrumented to collect the required properties from the bunches that reaches them, including the particle distributions.

Joints and Links

Beamlines, injectors and dumps (in short: jointables) are connected together using joints and links. Joints are placed where at least one connection is required. Links are internal objects of the joint and are used to describe the possible connections between the jointables attached to it. Each link connects two jointables together (one on the left and one on the right side) allowing to specify a routing criterion and the patching[1], when required. When a bunch reaches a joint, the links between its origin and the possible destinations are searched; if more are found, the one that minimize the merit function is selected. PLACET2 provides some powerful methods that make the creations of links a trivial task and automatise the management of joints.
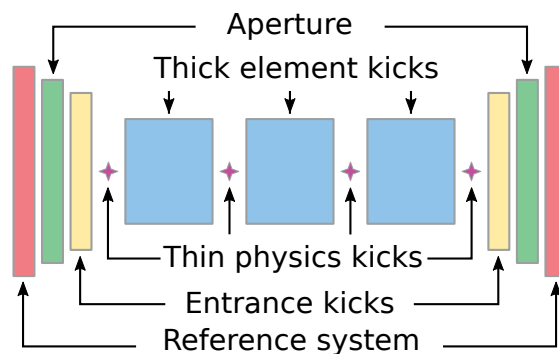
5.4   Element Structure

Figure 5.1: Sliced structure of the element

---

[1]The patch is the change of frame of reference when moving from a beamline to the next one.

PLACET2 models the elements as shown in Fig. 5.1. Each element can be setup by the user so that when a bunch is tracked, a number of kicks are applied. The first transformation takes into account the misalignment, modifying the reference frame. The tracking through the aperture follows, allowing to keep track of losses. The last kick before entering the core calculates the fringe-fields effect. When the bunch leaves the element, these kicks are applied in reversed order.

The thick core can be sliced. The slices are typically regular, but can develop on many levels: one can start slicing an element in two, to apply a wakefield kick in the middle, and then further slice each half to apply for instance a multipole kick at an high level of accuracy. Although this approach does not generate higher-order symplectic integrators, it allows to control very well the trade off between speed and accuracy while adding the physics effects in each element. With the relatively short distance travelled by the particles between the injector and the dump, the symplecticity is often not required. This is especially true when physics effects that are by nature not symplectic (like radiation or wakefields) are included.

Each element increments the bunch internal timer, by its length divided by the speed of light. In this way the bunch timer is always kept updated and time dependent elements can read the time from it. When computing the phase of a time dependent element there are three quantities involved:

1. the global phase, extracted from the bunch time,

2. the internal phase, given by the particle positions within the bunch,

3. the external phase, which is the phase of the element at $t = 0$ and is given by the user.

The global phase allows to take into account the beam time of flight, but can also make the setup of a long linac very tedious, as the external phase of each cavity needs to be specified according to its position down into the beamline. To circumvent this PLACET2 sets by default the global phase to zero when the first bunch arrives, so that the machine description is greatly simplified, while bunch-to-bunch phase errors are still taken into account. It is also possible to ignore the global phase.

The bunch timer must allow to accurately determine the global phase even in presence of frequencies up to 12 GHz or more. This requires precisions down to 1×10^{-15} s and even less. On the other hand, when simulating the continuous injection in a CW machine, one may reach time scales of 1×10^{-3} s magnitude and even more. This extremely wide range makes the common double precision not suitable. In fact, PLACET2 uses 320 bits floating point variables provided by the GMP library [92] to store the bunch time.

5.5 Linking beamlines

We consider as an example a multi-pass linac which is travelled by bunches at different energies. At the end of the linac a dipole magnet separates the bunches according to their energies, routing them to two different beamlines. As shown in Fig. 5.2 there are more ways to model this in PLACET2.

In Fig. 5.2*a* the dipole is placed in the linac beamline (*bl1*), the bunches can then be routed according to their positions after the dipole. In this case, when creating the two links, it will be necessary to specify the patching: a change of reference frame when moving from *bl1* to *bl2* or *bl3*.

In Fig. 5.2*b* the linac is terminated before the dipole and two copies of the dipole are placed in the downstream beamlines. In this case the links can use the bunch energy as the criterion to select *bl2* or *bl3* and no patching is needed.

The second method is simpler and improves the numerical stability. Indeed using two separated dipoles the particles remain centred, while with a single dipole they gain a macroscopic offset which provokes a loss of precision. On the other hand the first method allows to better handle imperfections and time dependencies, as in the case of an RF-deflector instead of a static dipole.
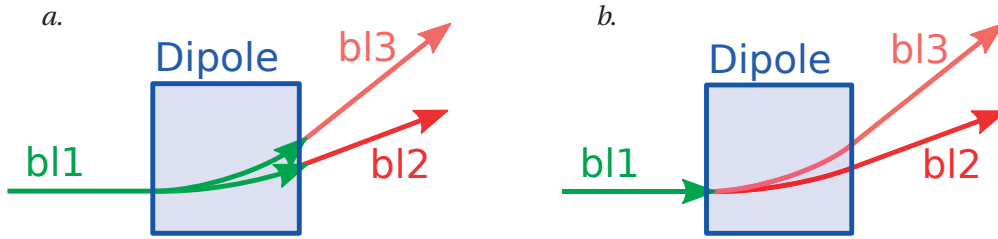
Figure 5.2: Two different approaches to beamline connections.

5.6 Machine operation and synchronisation

The first step when running the machine consists in setting the machine timer and communicate its value to all the joints. Each joint searches for bunches in the beamlines or injectors attached to it. The candidate bunches: the ones whose timer is smaller than the machine timer, are sorted according to their internal timers. The joint then retrieves the first bunch from its original beamline or injector and searches for the possible links. If more are found, the routing criteria are evaluated and the bunch is sent through the link whose merit function has returned the smaller value. If the link is connected to a dump, the bunch is destroyed, otherwise if it is connected to a beamline the bunch is tracked through all the elements, waiting at the subsequent joint. The joint then moves to the next bunch, its work terminates when all the bunches have a time bigger than the machine one. A simplified flow chart showing the fundamental logic of the joint is shown in Fig. 5.3.

Figure 5.3: Simplified flow chart showing the advancing procedure for one joint.

Figure 5.4: Simplified flow chart showing the machine run procedure.

When no more joints have bunches to route, the machine timer can be incremented, iterating the joint procedure until all the bunches have left the machine or a certain time has been reached, as shown in Fig. 5.4

The key ingredient to preserve the bunch time sequence everywhere in the machine is to keep the step of the machine timer smaller than the time taken to travel the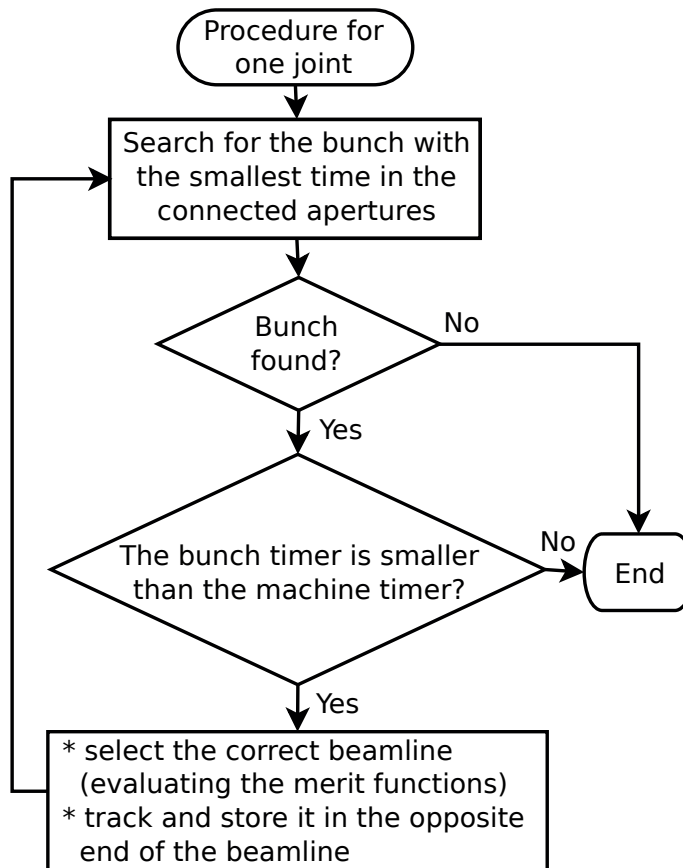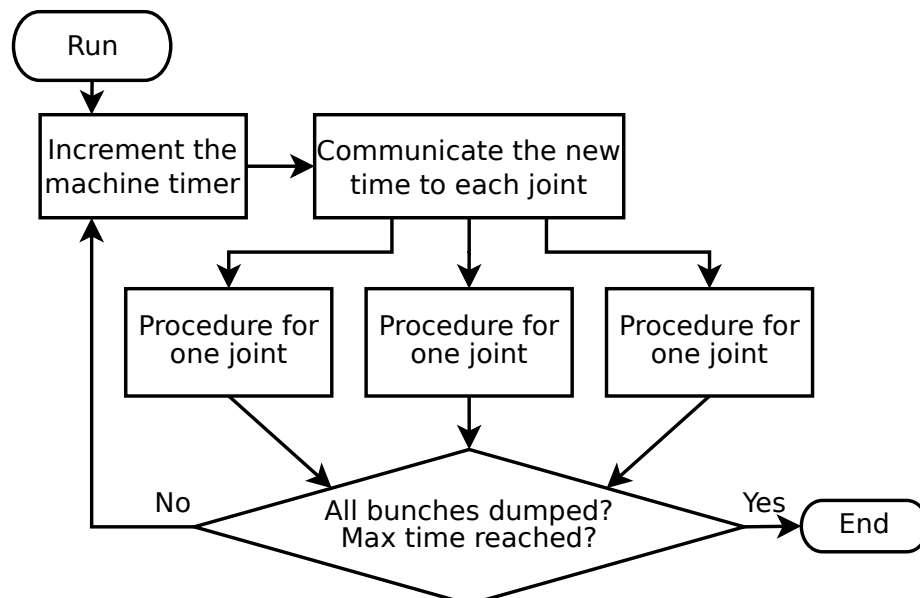 shortest beamline. Given that the tracking in each beamline is an independent task, PLACET2 runs the tracking in parallel over different beamlines, taking advantages of multicore CPUs.

5.7   A simple example

Figure 5.5 shows a simple machine that has two joints (the red rectangles). Two bunches with a small time separation are sitting in the injector. *(a)*: the first bunch is routed to the longer beamline and goes straight down ending up in future; the second joint cannot advance it yet. *(b)*: the second bunch goes to the shorter beamline arriving at the second joint with a timer smaller than the one of the first bunch. *(c)*: the second joint routes to the dump bunch 2 first and then bunch 1 *(d)*.

The following minimal listing shows how to describe a simple machine like the one in Fig. 5.5:

```
1   Machine my_mac
2
3   my_mac new_injector my_inj
4   BunchSingle −energy 1.0 −time_before_next 10e−9
5   BunchSingle −energy 1.0
6
7   my_mac new_beamline my_bl_long
8    Drift −length 10
9   my_mac new_beamline my_bl_short
10   Drift −length 1
11
12  my_mac new_dump my_dmp
13
14  my_mac link −in my_inj −out my_bl_long  −cmd {[bunch time_s] > 5e−9}
15  my_mac link −in my_inj −out my_bl_short −cmd {[bunch time_s] < 5e−9}
16  my_mac link −in my_bl_long  −out my_dmp
17  my_mac link −in my_bl_short −out my_dmp
18
19  my_mac run
```

The program starts creating a machine. An injector is then added and two bunches are inserted with a time separation of 10 ns. Two beamlines are created and a drift is added in both of them: the first 10 m long and the second 1 m long. A dump is created. The lines 14 to 17 connect the machine with links. The firsts two of them attach the injector to the beamlines, the bunch time is used as routing criterion. The seconds connect the beamlines to the dump, note that
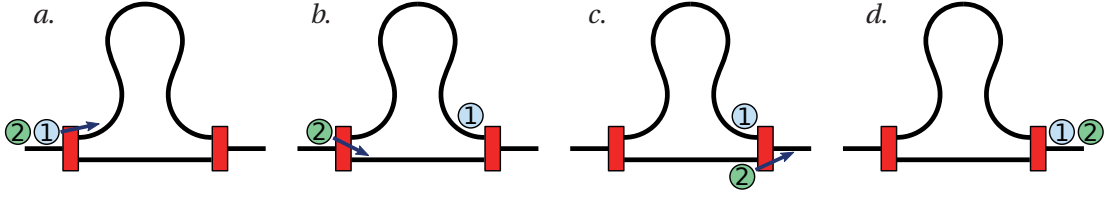
Figure 5.5: Operation of a simple machine.

in this case there is no need for routing criteria. Finally the machine is run.

This example can be run by PLACET2 as it is. The dump prints a message when a bunch reaches it, showing that bunch 2 arrives before bunch 1.

One should note that the creation of joints is hidden to the user, who only has to specify the links. The program performs automatic logic and topological checks adding the links to existing joints or creating new ones.

A small caveat is that in case of multiple possible outgoing links, the one which evaluate the criterion to the *smaller* value is selected. This is a good choice when the criteria are distances with respect to a set of values, for example:

```
1  −cmd { abs([bunch energy] − 10) }
2  −cmd { abs([bunch energy] − 20) }
```

but can be confusing in the above example. Indeed the first bunch reaches the first joint with zero time and the boolean expression on line 14 is evaluated to false or 0, while the expression on line 15 is true or 1. As $0 < 1$ the bunch is routed to the first, longer beamline. The second bunch reaches the first joint with a time of 10 ns (the distance set at the injector), therefore is routed to the second beamline.

Note that the two beamlines contain two drifts of different lengths and would not join themselves. Topological checks at the required tolerance can be performed, but only results in warning messages. This is a crucial point as it allows to perform simulations even with first cut lattices, yet to be refined.

5.8   Topological limitations

Backtracking a beamline, as would be required by a dogbone RLA [14], has been taken into account, but is deliberately inhibited. The main issue here is the handling of the case in which bunches are simultaneously injected from both the ends of the beamline. Even ignoring parasitic interactions, one has still to synchronise the bunches from the two sides, tracking them in the correct time sequence in each element.

Another limitation comes when bunches are superimposed. Although this does not cause

problems to PLACET2, the bunches are kept separated, therefore collective effects are not computed on the whole particle ensemble. The bunch merging has also been considered, in this case the major difficulty comes when the bunch needs to be split again. This requires some classification techniques to re-group the particles in separated bunches.

As the studies conducted up to now did not require these advanced features, they are currently not implemented.

5.9 Adding kicks

The procedure for including additional kicks articulates through the following steps:

1. Write a class "kick_something" providing the header and the source files, following the examples of the existing ones;

2. Add an include statement in the file "kick_all.hh";

3. Add the tracking member functions in the file "tracker.cc";

4. Add the target file in "Makefile.objs" for compilation.

Shall the kick be available to the user for declaration and insertion in any element through the TCL interface, then it needs to be declared in the "kick_factory.hh" header and in the "element.i" SWIG file.

All these steps (except for the first one) are completed in a bunch of seconds, following the syntax already in place for the existing kicks.

5.10 Availability

PLACET2 is currently available as a branch of PLACET on the *clicsw* CERN SVN repository. The compilation and installation process is identical to the one of PLACET, with the usual procedure: configure, make, make install. After the installation, the "bin" folder contains the PLACET2 executable, in addition to the PLACET one.

PLACET2 has been successfully compiled and run on ArchLinux and UbuntuLinux.

5.10.1 Required libraries

For the tracking core:

- GNU Scientific Library, GSL: for many statistical and mathematical functions;

- GNU Multiple Parallel Library, GMP: for the extended floating point precision of the bunch timer;

- Boost Program Options: to parse arguments and flags when building many objects.

For the interfaces:

- Tcl/Tk

- Octave

5.11 Conclusions

The development of the logic necessary to describe and simulate recirculating lattices led to a novel version of PLACET. PLACET2 has been written from scratch integrating a number of novel concepts. The code was designed for computational efficiency but trying to keep it as simple as possible; therefore facilitating the addition of bunch models, accelerator components and physics effect. Nevertheless it is extremely versatile, being capable of handling arbitrary complex topologies such as multi-pass ERLs or the CLIC Drive Beam Complex. It can perform multi-bunch tracking closely mimicking the operation of the real machine.

Being the fundamental tool for these doctoral studies, PLACET2 has already been applied to many projects (LHeC, PERLE, CTF3 and, ongoing, CLIC). It has been extensively validated against other codes such as MAD-X, OPTIM, elegant and experimental measures at the CTF3 Combiner Ring, proving itself to be consistent, effective and powerful.

6 Conclusions

In this thesis we considered beam dynamic issues related with modern designs of recirculating machines, with focus on the LHeC project and on the CTF3 Combiner Ring. These two designs both operate with high currents, which make them prone to show instabilities and require careful studies of the beam dynamics.

A number of collective effects, such as wakefields, radiation and beam-beam, have been taken into account. The study of multi-bunch effects is particularly challenging in recirculating lattices as the temporal sequence of the bunch train is often modified within the pulse. This required the development of a dedicated tracking code, capable of tracking each bunch independently across multiple beamlines. PLACET2, the new version of PLACET, has been written from scratch. All the common accelerator components have been implemented, together with the aforementioned collective effects and the logic necessary to describe and run a generic recirculating machine.

PLACET2 has been applied to the LHeC ERL design, allowing to establish the transport of the beam from the injector to the dump. This has been achieved with the first end-to-end simulation and came with improvements in the lattice, such as the redesign of the spreading sections and interventions on the path-length-adjusting chicanes. Furthermore the lattice have been expanded, including a design of the detector bypass. The effect of multi-bunch wakefields has been extensively studied together with the coupling with the beam-beam, the final conclusion being that the current set of parameters does not induce beam instabilities. The infrastructure to extend these studies to other effects, such as the ion-cloud, has been prepared. These investigations were extended to the design of PERLE: the CERN ERL Facility, helping to finalize its design.

An experimental validation of the code was obtained at CTF3, where the beam-dynamics in the Combiner Ring was investigated. The state-of-the-art model of the ring, imported in PLACET2, allowed to reproduce and extend the results from the MAD-X simulations and the studies of a multi-bunch instabilities that appeared during the first commissioning. By means of a phase monitor, a measure of the ring length and its response to optics scaling

was obtained. This verified the possibility to make the ring shorter, in agreement with the simulations.

The main outcomes of this thesis are:

- The determination of the feasibility of the LHeC project with respect to the considered beam dynamics effects (radiation, wakefields and beam-beam), with a consistent advance of its design and the identification of additional possibilities for further improvements.

- The beam dynamic studies and measures performed at the CTF3 combiner ring, aimed at explore alternative ways to control the ring length: a crucial parameter for the operation of the drive beam complex.

- The delivery of PLACET2, an innovative and complete tool for beam dynamics investigations at recirculating machines. PLACET2 is a flexible and easily extendable parallel code which allows to describe and simulate the operation of recirculating lattices, with multiple beam models and a number of physics effects already implemented.

A An exact, planar, geometrical solution of the SBEND

In this appendix an exact, planar, geometrical solution of the sector bending magnet (SBEND) is presented. It can be useful for benchmarking and educational purposes. A uniform magnetic field is present between the x-axis and the ray t, as illustrated in Fig. A.1. The ideal particle, red trace, enters the dipole perpendicular to the x-axis, has a bending radius of $\rho = |OD|$, is bent exactly by θ and leaves the dipole perpendicularly to the ray t. A real particle, blue trace, can behave much differently. It can have an initial offset with respect to the ideal entrance position: $x = \overline{DA}$, it can have an entrance angle x' and the energy can as well be mismatched so that the bending radius is different $r = \overline{BA}$. For this particle a geometrical solution of the final angle and position and as well the path length, has been developed.

The parameters used to describe the dipole are:

- Ideal bending angle = θ,

- Ideal bending radius = ρ,

- reference energy = E_0.

The parameters of the particle are:

- Energy = E,
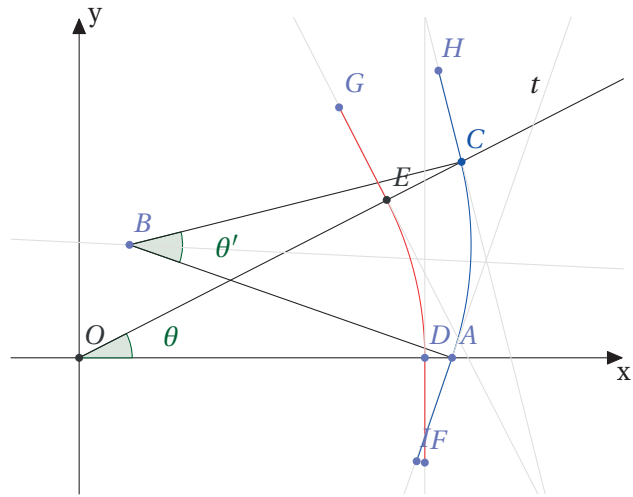
- Displacement = x,

- Entering angle = x'.

Figure A.1: Scheme of two traces in a sector bending magnet. The red trace shows the path of the ideal particle, while the blue trace represents a particle with both launching and energy errors.

Note that in this case x' represents an actual angle, in contrast with the PLACET2 definitions (see Sec. 5.2).

The bending radius can be computed as: $r = \frac{E}{E_0}\rho$ and the coordinates of the point B are then obtained as:

$$B_x = \rho + x - r\cos x'; \quad B_y = r\sin x'\,\mathrm{sign}\,\theta. \tag{A.1}$$

Note that the vertical coordinate of B is corrected with the sign of θ.

The exit point C lays on the ray t, so its coordinates can be parametrised with the help of the unit vector: $\hat{u} = (\cos\theta, \sin\theta)$ and a positive parameter m, so that $C \equiv m\hat{u}$.

To determine the parameter m we compute the segment $\overline{BC}$ and we impose its length to r:

$$|BC|^2 = |m\hat{u} - B|^2 = (m\,u_x - B_x)^2 + (m\,u_y - B_y)^2 = r^2 \tag{A.2}$$

The last equivalence can be rewritten as a standard second order equation in m:

$$\overbrace{(u_x^2 + u_y^2)}^{a=1}m^2 - 2\overbrace{(u_x B_x + u_y B_y)}^{b}m + \overbrace{B_x^2 + By^2 - r^2}^{c} = 0, \tag{A.3}$$

which is solved by:

$$m = b + \sqrt{b^2 - c}. \tag{A.4}$$

We have discarded the smallest (and eventually negative) solution. A negative $b^2 - c$ parameter implies that the particle cannot exit the dipole from the outgoing face, this typically happens if the energy is too small.

The coordinates of the point C are then: $C = (C_x, C_y) = (mu_x, mu_y)$, the next computations follow easily:

- $|OC| = \sqrt{C_x^2 + C_y^2}$;

- $|AC| = \sqrt{(\rho + x - C_x)^2 + C_y^2}$;

- $l = 2\,r\,\mathrm{asin}(|AC|/2r)$;

- $x_f = (|OC| - \rho)\,\mathrm{sign}\,\theta$.

Finally the exit angle x'_f is obtained from the vector product:

$$x'_f = \mathrm{asin}\,\frac{\overrightarrow{BC} \times \overrightarrow{OC}}{|BC||OC|} = \mathrm{asin}\,\frac{\overrightarrow{BC} \times \hat{u}}{|BC|} = \mathrm{asin}\,\frac{(C_x - B_x)u_y - (C_y - B_y)u_x}{r}. \tag{A.5}$$

B Modelling of the RF Focussing

Transverse focussing effects in RF cavities become important when the energy gain is relevant compared to the initial energy. The RF focussing originates from the radial field components which naturally arises from the varying $E_z(s, t)$ seen by a particle. A miscalculation may introduce important optics mismatch.

A transport matrix including the RF focussing was derived by Chambers and later generalized by Rosenzweig and Serafini (RS) [93]. However, that matrix is not easily separated in a number of kicks. This is a strong requirement in PLACET2, as it allows to insert physics kicks (such as wakefields) into the body of the cavity.

To overcome this limitation the *end fields* approach was followed. End fields in PLACET are added before and after the body of the cavities, improving their modelling. The key idea, following [29], is to compute the flux of the electric field across the surface of a cylinder whose axis is oriented in the longitudinal direction, with one face into the cavity and the other outside. Neglecting the charge inside the cylinder and applying the Gauss Law, the flux across the lateral surface, $\Phi_\perp$, summed to the flux across the face inside the cavity, $\Phi_\parallel$, must be zero:

$$\Phi_\perp + \Phi_\parallel = \int_{s_1}^{s_2} G_\perp 2\pi r \, \mathrm{d}s + G\pi r^2 = 0. \tag{B.1}$$

This can be used in the computation of the transverse kick at the entrance:

$$\Delta x' = \frac{1}{E} \int_{s_1}^{s_2} eG_\perp 2\pi r \, \mathrm{d}s = -\frac{eG\pi r^2}{2\pi r E} = -\frac{eG}{2E} x = -\frac{\delta}{2L} x, \tag{B.2}$$

Where the relative energy gain $\delta = eV/E$ has been introduced. The same kick is applied at the exit, with the energy increased:

$$M_{\mathrm{cav}} = \begin{pmatrix} 1 & 0 \\ -\frac{\delta}{2L(\delta+1)} & 1 \end{pmatrix} \begin{pmatrix} 1 & L\frac{\ln(\delta+1)}{\delta} \\ 0 & -\frac{1}{\delta+1} \end{pmatrix} \begin{pmatrix} 1 & 0 \\ -\frac{\delta}{2L} & 1 \end{pmatrix}. \tag{B.3}$$

Appendix B. Modelling of the RF Focussing

Although this approach is good when the energy gain is small compared to the beam energy, it is inaccurate when high accelerating gradients are applied to low energy beams. An example is PERLE, where the first cavity accelerates the beam from 5 MeV to more than 20 MeV, giving a crucial contribution to the optics. Nevertheless the accuracy can easily be increased slicing the cavity longitudinally and applying the end fields to each slice. This allows one to take into account the energy gain into the cavity, according to the actual profile of the accelerating gradient. For a π-mode cavity $G \propto \cos^2(s)$, one cosine arising from the time evolution and the second from the spatial profile.

A comparison between the end fields, the sliced cavity and the RS methods, is shown in Fig. B.1 for a π-mode cavity with $L = 0.5$ m, $G = 5$ MV/m. It can be noted how the sliced cavity and the RS models agree for electron beam energies >5 MeV (note that the RS model itself applies in the ultra-relativistic approximation), while the end fields model remains separated.
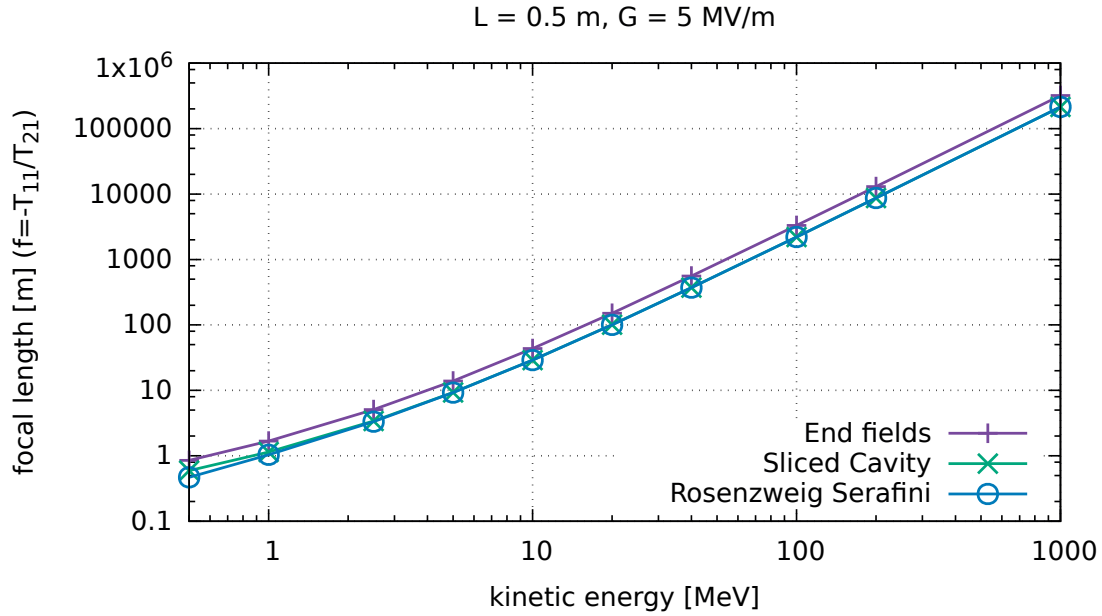

Figure B.1: Comparison of the RF focussing resulting from different models of a π-mode cavity. The horizontal axis shows the energy of the incoming beam, while the vertical axis is the focal length, computed as the ratio between the T_{11} and T_{21} terms of the transport matrix.

Bibliography

[1] J. A. Fernandez *et al.*, "A Large Hadron Electron Collider at CERN: Report on the Physics and Design Concepts for Machine and Detector," *Journal of Physics G: Nuclear and Particle Physics*, vol. 39, no. 7, p. 075001, 2012.

[2] E. C. Aschenauer *et al.*, "eRHIC Design Study: An Electron-Ion Collider at BNL," 2014.

[3] S. A. Bogacz, J. Ellis, L. Lusito, D. Schulte, T. Takahashi, M. Velasco, M. Zanetti, and F. Zimmermann, "SAPPHiRE: a Small Gamma-Gamma Higgs Factory," 2012.

[4] R. Abela *et al.*, "The European X-Ray Free-Electron Laser. Technical design report," 2007.

[5] G. Neil *et al.*, "The JLab high power ERL light source," *Nuclear Instruments and Methods in Physics Research Section A: Accelerators, Spectrometers, Detectors and Associated Equipment*, vol. 557, no. 1, pp. 9 – 15, 2006.

[6] N. Vinokurov *et al.*, "Novosibirsk free electron laser facility: Two-orbit ERL with two FELs," in *Proceedings of the IPAC10*, (Kioto, Japan), 2010. WEOARA03.

[7] T. Atkinson, A. Bondarenko, A. Matveenko, and Y. Petenev, "Conceptual Design Report for a multi-turn Energy Recovery Linac-based Synchrotron Light Facility (Femto-Science Factory)," 2015.

[8] R. R. Hajima, N. Nishimori, N. Sei, M. Shimada, and N. Nakamura, "Simulations of XFELO for the KEK ERL," in *Proceedings of FEL12*, (Nara, Japan), 2012. WEPD30.

[9] H. R. Weller, M. W. Ahmed, H. Gao, W. Tornow, Y. K. Wu, M. Gai, and R. Miskimen, "Research opportunities at the upgraded HIγS facility," *Progress in Particle and Nuclear Physics*, vol. 62, no. 1, pp. 257 – 303, 2009.

[10] O. Adriani *et al.*, "Technical Design Report EuroGammaS proposal for the ELI-NP Gamma beam System," 2014.

[11] B. Auchmann, A. Bogacz, C. Bracco, O. Brüning, R. Calaga, V. Cassou, K.and Chetvertkova, E. Cormier, E. Daly, D. Douglas, K. Durpaz, B. Goddard, J. Henry, E. Jensen, M. Klein, P. Kostka, F. Marhauser, A. Martens, A. Milanese, Y. Peinaud, D. Pellegrini, N. Pietralla, Y. Pupkov, A. Valloni, G. Willering, D. Wollmann, and F. Zomer, "PERLE: Powerful Energy Recovery Linac Experiments - Conceptual Design Report," *To be published*, 2015.

Bibliography

[12] R. Kazimi, "Simultaneous four-hall operation for 12 GeV CEBAF," 2013. THPFI091.

[13] S. Aulenbacher, "Design and simulation of the internal gas-target for MAGIX," diploma thesis, Institut für Kernphysik, Johannes Gutenberg-Universität, Mainz, 2014.

[14] S. Bogacz, G. Krafft, V. Morozov, Y. Roblin, K. Beard, *et al.*, "Electron model of a dogbone rpl with multi-pass arcs," in *Proceedings of LINAC2012*, (Tel-Aviv, Israel), 2010. MOPB014.

[15] M. Aicheler, P. Burrows, M. Draper, T. Garvey, P. Lebrun, K. Peach, N. Phinney, H. Schmickler, D. Schulte, *et al.*, "A Multi-TeV Linear Collider Based on CLIC Technology," 2012.

[16] A. Abada *et al.*, "The International Linear Collider Technical Design Report, Volume 3.II: Accelerator Baseline Design," *ILC-Report-2013-040. http://www. linearcollider. org/ILC/Publications/Technical-Design-Report*, 2013.

[17] A. Grudiev, S. Calatroni, and W. Wuensch, "New local field quantity describing the high gradient limit of accelerating structures," *Phys. Rev. ST Accel. Beams*, vol. 12, p. 102001, Oct 2009.

[18] A. Chao and M. Tigner, eds., *Handbook of Accelerator Physics and Engineering*. World Scientific, 2006. 3rd Printing.

[19] W. K. H. Panofsky and W. A. Wenzel, "Some considerations concerning the transverse deflection of charged particles in radio-frequency fields," *Review of Scientific Instruments*, vol. 27, no. 11, pp. 967–967, 1956.

[20] P. B. Wilson, "Introduction to wakefields and wake potentials." SLAC-PUB-4547, 1989.

[21] A. S. Corporation, "Hfss: High frequency structure simulator."

[22] W. Bruns, "GdfidL: a finite difference program with reduced memory and CPU usage," in *Proceedings of the 1997 Particle Accelerator Conference*, vol. 2, pp. 2651–2653 vol.2, May 1997.

[23] H. Zha, A. Latina, A. Grudiev, G. De Michele, W. Wuensch, D. Schulte, and E. Adli, "Beam-based measurements of long range transverse wakefields in clic main linac accelerating structure," in *Proceedings of the IPAC15*, (Richmond VA, USA), 2015. TUPTY056.

[24] R. L. Gluckstern, "Longitudinal impedance of a periodic structure at high frequency," *Phys. Rev. D*, vol. 39, pp. 2780–2783, May 1989.

[25] K. Yokoya and K. Bane, "The longitudinal high-frequency impedance of a periodic accelerating structure," in *Particle Accelerator Conference, 1999. Proceedings of the 1999*, vol. 3, pp. 1725–1727 vol.3, 1999.

[26] A. V. Fedotov, R. L. Gluckstern, and M. Venturini, "Transverse impedance of a periodic array of cavities," *Phys. Rev. ST Accel. Beams*, vol. 2, p. 064401, Jun 1999.

[27] K. Bane, "Short-range dipole wakefields in accelerating structures for the NLC." SLAC-PUB-9663, 2003.

[28] R. Calaga, "A design for an 802 mhz erl cavity." CERN-ACC-NOTE-2015-0015, 2015.

[29] D. Schulte, "Main linac basics," in *International Accelerator School for Linear Colliders*, (Whistler, BC, Canada), 2015.

[30] V. E. Balakin, A. V. Novokhatsky, and V. P. Smirnov, "VLEPP: TRANSVERSE BEAM DYNAMICS," *Conf. Proc.*, vol. C830811, pp. 119–120, 1983.

[31] T. O. Raubenheimer, "Estimates of emittance dilution and stability in high-energy linear accelerators," *Phys. Rev. ST Accel. Beams*, vol. 3, p. 121002, Dec 2000.

[32] D. Alesini, C. Biscari, A. Ghigo, F. Marcellini, and R. Corsini, "Beam instability induced by RF deflectors in the combiner ring of the CLIC test facility and mitigation by damped deflecting structures," *Phys. Rev. ST Accel. Beams*, vol. 14, p. 022001, Feb 2011.

[33] J. Plouin, S. Chel, and G. Devanz, "Spl cavity design by cea-saclay," in *3rd SPL Collaboration Meeting*, pp. 11–13, 2009.

[34] P. Wilson, *Study of beam blow-up in electron linacs.* 1963.

[35] D. Schulte, "Multi-bunch calculations in the CLIC main linac," in *Proceedings of the PAC09*, (Vancouver, BC, Canada), 2009. FR5RFP055.

[36] G. H. Hoffstaetter and I. V. Bazarov, "Beam-breakup instability theory for energy recovery linacs," *Phys. Rev. ST Accel. Beams*, vol. 7, p. 054401, May 2004.

[37] D. Alesini and A. Gallo, "Effects of the beam loading in the rf deflectors of the CLIC test facility CTF3 combiner ring," *Phys. Rev. ST Accel. Beams*, vol. 7, p. 034403, Apr 2004.

[38] A. Smirnov, "Group velocity effect on resonant, long-range wake-fields in slow wave structures," *Nuclear Instruments and Methods in Physics Research Section A: Accelerators, Spectrometers, Detectors and Associated Equipment*, vol. 480, no. 2–3, pp. 387 – 397, 2002.

[39] E. Adli, *A Study of the Beam Physics in the CLIC Drive Beam Decelerator.* PhD thesis, University of Oslo, Norway, 2009.

[40] K. Oide, "Synchrotron-radiation limit on the focusing of electron beams," *Phys. Rev. Lett.*, vol. 61, pp. 1713–1715, Oct 1988.

[41] J. D. Jackson, *Classical electrodynamics.* New York, NY: Wiley, 3rd ed. ed., 1999.

[42] A. Hofmann, *The Physics of Synchrotron Radiation.* Cambridge Monographs on Particle Physics, Nuclear Physics and Cosmology, Cambridge University Press, 2004.

[43] A. Wolsky, "Low-emittance storage rings," in *Proceedings of the Advanced CERN Accelerator School* (W. Herr, ed.), (Trondheim, Norway), 2013.

Bibliography

[44] M. Sands, *The physics of electron storage rings: an introduction.* SLAC-121 UC-28, 1970.

[45] R. Feynman, R. Leighton, and M. Sands, *The Feynman Lectures on Physics.* Addison-Wesley, second ed., 1963.

[46] T. Dohlus, M Limberg and P. Emma, "Bunch Compression for Linac-based FELs," in *ICFA Beam Dynamics Newsletter, No. 38* (I. S. Ko, ed.), 2005.

[47] E. L. Saldin, E. A. Schneidmiller, and M. Yurkov, "On the coherent radiation of an electron bunch moving in an arc of a circle," *Nuclear Instruments and Methods in Physics Research Section A: Accelerators, Spectrometers, Detectors and Associated Equipment*, vol. 398, no. 2, pp. 373–394, 1997.

[48] G. Stupakov and P. Emma, "CSR wake for a short magnet in ultrarelativistic limit," in *Proceedings of EPAC*, (Paris, France), p. 1479, 2002.

[49] C. Mayes, *Energy recovery linear accelerator lattice design & coherent synchrotron radiation.* PhD thesis, Cornell University, 2009.

[50] Y. S. Derbenev, J. Rossbach, E. L. Saldin, and V. D. Shiltsev, "Microbunch radiated tail-head interaction," *Tesla FEL 95-05*, September 1995.

[51] J. Arthur *et al.*, "Linac coherent light source (LCLS) conceptual design report," *SLAC-R-593*, April 2002.

[52] W. Herr and T. Pieloni, "Beam-beam effects," in *Proceedings of the Advanced CERN Accelerator School* (W. Herr, ed.), (Trondheim, Norway), 2013.

[53] R. Hollebeek, "Disruption limits for linear colliders," *Nuclear Instruments and Methods*, vol. 184, no. 2, pp. 333 – 347, 1981.

[54] O. Brüenig *et al.*, "Development of an ERL based TeV energy ep and eA Collider at CERN," in *ICFA Beam Dynamics Newsletter, No. 68* (J. Wang, ed.), 2015.

[55] F. Willeke, "HERA hits new heights," *CERN Courier*, vol. 45, Mar 2005.

[56] F. Zimmerman, O. Brüening, and M. Klein, "The LHeC as a higgs boson factory," in *Proceedings of the IPAC13*, (Richmond VA, USA), 2013. MOPWO054.

[57] A. Milanese, "Warm magnets for LHeC / test facility arcs." Talk at the LHeC workshop, 2014. https://indico.cern.ch/event/278903/session/6/contribution/41.

[58] S. Machida *et al.*, "Acceleration in the linear non-scaling fixed-field alternating-gradient accelerator EMMA," *Nat Phys*, vol. 8, pp. 243–247, Mar 2012.

[59] D. Trbojevic, "ERL designs based on FFAG arcs (eRHIC, LHeC, Cornell)." Talk at the LHeC workshop, 2015. https://indico.cern.ch/event/356714/session/12/contribution/114.

118

[60] F. Wittgenstein, A. Hervé, M. Feldmann, D. Luckey, and I. Vetlitsky, "Construction of the L3 magnet," in *11th International Conference on Magnet Technology (MT-11)* (T. Sekiguchi and S. Shimamoto, eds.), pp. 130–135, Springer Netherlands, 1990.

[61] O. Grobner, "Vacuum performance," in *Proceedings 3rd Workshop on LEP Performance* (J. Pole, ed.), (Chamonix, France), 1993.

[62] A. Zaltsman and R. Lambiase, "High power rf systems for the bnl erl project," in *Proceedings of the PAC11*, (New York, NY, USA), 2011. TUP125.

[63] D. Pellegrini, A. Latina, and D. Schulte, "PLACET2: a Novel Code for Beam Dynamics in Recirculating Machines," in *Proceedings of the IPAC15*, (Richmond VA, USA), 2015. MOPJE068.

[64] D. Schulte, "Beam-beam simulations with GUINEA-PIG," in *Proceedings of the ICAP98*, (Monterey CA, USA), 1998.

[65] V. Lebedev, "OptiM - Computer code for linear and non-linear optics calculations." http://pbar.fnal.gov/organizationalchart/lebedev/OptiM/optim.htm, 2014.

[66] V. N. Litvinenko, "Chromaticity of the lattice and beam stability in energy recovery linacs," *Phys. Rev. ST Accel. Beams*, vol. 15, p. 074401, Jul 2012.

[67] A. Valloni, "Test facility lattice design." Talk at the LHeC Meeting, 2014. https://indico.cern.ch/event/344046/.

[68] D. Möhl, G. Petrucci, L. Thorndahl, and S. van der Meer, "Physics and technique of stochastic cooling," *Physics Reports*, vol. 58, no. 2, pp. 73 – 102, 1980.

[69] G. Geschonke and A. Ghigo, "CTF3 Design Report," Tech. Rep. CERN-PS-2002-008-RF. CTF-3-NOTE-2002-047. LNF-2002-008-IR, CERN, Geneva, May 2002.

[70] R. Corsini *et al.*, "First full beam loading operation with the CTF3 linac," in *Proceedings of the EPAC04*, (Lucerne, Switzerland), 2004. MOOCH02.

[71] P. Skowronski, S. Bettoni, R. Corsini, A. Dabrowski, S. Doebert, A. Dubrovskiy, F. Tecker, R. Ruber, C. Biscari, and W. Farabolini, "Progress towards the CLIC feasibility demonstration in CTF3," in *Proceedings of the EPAC04*, (Kyoto, Japan), 2010. WEPE027.

[72] R. Ruber, V. Ziemann, T. Ekelöf, A. Palaia, W. Farabolini, and R. Corsini, "The CTF3 two-beam test stand," *Nuclear Instruments and Methods in Physics Research Section A: Accelerators, Spectrometers, Detectors and Associated Equipment*, vol. 729, pp. 546 – 553, 2013.

[73] J. N. Quirante, R. Corsini, A. Grudiev, T. Lefevre, S. Mazzoni, R. Pan, F. Tecker, W. Farabolini, F. Peauger, D. Gamba, *et al.*, "Califes: A multi-purpose electron beam for accelerator technology tests," in *Proceedings of the LINAC14*, (Geneva, Switzerland), 2014. MOPP030.

Bibliography

[74] C. Biscari, "Combiner Ring Lattice," Tech. Rep. CTFF3-002, INFN-LNF, Frascati, Rome, Apr 2001.

[75] J. Delahaye and A. Krusche, "The lattice design of the LEP electron positron accumulator (EPA)," *Nuclear Science, IEEE Transactions on*, vol. 30, pp. 2050–2052, Aug 1983.

[76] R. Chritin, "Mesures magnétiques complémentaires de l'aimant principal prototype EPA," Tech. Rep. SL-Note-2000-031-MS, CERN, Geneva, Apr 2000.

[77] R. Apsimon and J. Esberg, "Proof of the nonexistence of a linear solution for the CR2 injection region of the CLIC drive beam," Tech. Rep. CERN-OPEN-2014-045. CLIC-Note-1035, CERN, Geneva, Aug 2014.

[78] J. Laskar, "Frequency analysis for multi-dimensional systems. Global dynamics and diffusion," *Physica D: Nonlinear Phenomena*, vol. 67, no. 1–3, pp. 257 – 281, 1993.

[79] D. Stahlke, "gnuplot-iostream." https://github.com/dstahlke/gnuplot-iostream, 2015.

[80] R. Corsini, S. Bettoni, S. Doebert, P. Skowronski, F. Tecker, C. Biscari, A. Ghigo, and Y. C. Chao, "Experimental studies on drive beam generation in CTF3," in *Proceedings of the EPAC08*, (Genoa, Italy), 2008. MOPP010.

[81] R. Corsini. private communication.

[82] H. Grote, F. Schmidt, L. Deniau, and G. Roy, "The MAD-X Program: User's Reference Manual." http://mad.web.cern.ch/mad/.

[83] M. Borland, "elegant: A flexible SDDS-compliant code for accelerator simulation," *Advanced Photon Source LS*, vol. 287, September 2000.

[84] D. Sagan, "Bmad: A relativistic charged particle simulation library," *Nuclear Instruments and Methods in Physics Research Section A: Accelerators, Spectrometers, Detectors and Associated Equipment*, vol. 558, no. 1, pp. 356 – 359, 2006.

[85] J. Crittenden, G. Hoffstaetter, M. Liepe, C. Mayes, and D. Sagan, "Recent progress on beam-breakup calculations for the Cornell x-ray ERL," in *Proceedings of the 2009 Particle Accelerator Conference*, 2009.

[86] D. Sagan. private communication.

[87] A. Latina, Y. Levinsen, D. Schulte, and J. Snuverink, "Evolution of the Tracking Code PLACET," in *Proceedings of IPAC13*, (Shanghai, China), 2013. MOPWO053.

[88] A. Latina, J. Pfingstner, D. Schulte, E. Adli, F. J. Decker, and N. Lipkowitz, "Experimental demonstration of a global dispersion-free steering correction at the new linac test facility at SLAC," *Phys. Rev. ST Accel. Beams*, vol. 17, p. 042803, Apr 2014.

[89] J. Pfingstner, *Mitigation of ground motion effects via feedback systems in the Compact Linear Collider*. PhD thesis, Vienna, Tech. U., 2013.

[90] D. M. Beazley, "Automated scientific software scripting with swig," *Future Gener. Comput. Syst.*, vol. 19, pp. 599–609, July 2003.

[91] A. Latina, E. Adli, H. Burkhardt, G. Rumolo, D. Schulte, R. Tomas, and Y. Renier, "Recent improvements in the tracking code PLACET," 2008. TUPP094.

[92] T. Granlund and the GMP development team, *GNU MP: The GNU Multiple Precision Arithmetic Library*, 6.0.0 ed., 2015. http://gmplib.org/.

[93] J. Rosenzweig and L. Serafini, "Transverse particle motion in radio-frequency linear accelerators," *Phys. Rev. E*, vol. 49, pp. 1599–1602, Feb 1994.

Dario Pellegrini

Personal Data

Place and Date of Birth:	Italy | 30 May 1988
Address:	Route de Segny 461b, Prevessin-Moens 01280, France
Phone:	+39 329 3446187
email:	pellegrini.dario@gmail.com

Summary

I'm a young, passionate physicist with a great interest for particle accelerator machines. I enjoy designing them and study their operation with detailed computer simulations. The main machines to which I contributed are LHeC, PERLE, CTF3 and SuperB. I am not only productive with many popular accelerator codes (MADX, elegant, OptiM) but I am the main developer of the PLACET2 code, which allows for multi-bunch tracking in recirculating machines. I am also familiar with experimental measures, instruments, basic electronics and I have some control-room experience. I like to think outside the box, pursuit a global view and come up with my own solutions, but at the same time I take the assigned tasks very seriously. I would like to improve my general knowledge of accelerator physics and possibly follow the construction of an innovative machine from the early design, to the commissioning and operation phases.

Professional Experience

Apr 2016   Fellowship in Accelerator Physics, **CERN**, Switzerland
Beam-Beam effect investigations in the weak-strong regime for the LHC, HL-LHC and FCC.

Education

Apr 2016   Ph.D. in Accelerator Physics at **EPFL**, Switzerland
Thesis: "Beam Dynamics Studies in Recirculating Machines"
Thesis developed at **CERN** with the CERN Doctoral Program Grant.
Advisors: Prof. L. Rivkin, Dr. A. Latina

Sep 2012   Master Degree in Experimental Physics at **Padova University**, Italy
Thesis: "Beam dynamics studies and optimization of the SuperB Injection System"
Thesis developed at **INFN-LNF** with the INFN grant for near-graduate students.
Advisors: Prof. R. Stroili, Dr. S. Guiducci \| 106/110

Jun 2010   Bachelor Degree in Physics at **Padova University**, Italy
Thesis: "Performance of the DANTE detector coupled to the γ-ray array AGATA"
Thesis developed at **INFN-LNL**.
Advisors: Prof. S. Lunardi, Dr. J. J. Valiente \| 101/110

Jul 2007   **Liceo Scientifico-Tecnologico "B. Castelli"**, Brescia, Italy \| 97/100.

International Schools

Completed with outstanding results where applicable.

Nov 2015   International Accelerator School for Linear Colliders, Whistler (BC), Canada.
Course C: XFEL Physics and Technology.

Jan 2015	USPAS, Old Dominion University, Hampton (VA), USA "Special Topics in Accelerator Physics" | S. Y. Lee, et al.
Aug 2013	Advanced CAS, Trondheim, Norway. RF Laboratory.
Jun 2013	USPAS, Colorado State University, Fort Collins (CO), USA "Design of Electron Storage and Damping Rings" | A. Wolski and D. Newton. "Linear Accelerator Design for Free Electron Lasers" | S. Di Mitri and M. Venturini.
Nov 2012	International Accelerator School for Linear Colliders, Indoore, India. Course A: Accelerator Physics.
Sep 2010	Euroschool on Exotic Beams, Santiago De Compostela, Spain.

Stages

Feb 2015	Spent a week at JLab, Newport News (VA), USA Improvement of the LHeC lattice design in collaboration with A. Bogacz.
Jul-Aug 2011	Summer Student at GSI, Darmstadt, Germany Developed a GEANT4 simulation of an hybrid detector for γ-rays.
Aug 2009	Two Weeks Summer Stage at INFN-LNL In vacuum testing of the DANTE detector for heavy ions.

Teaching

Jan 2016	JUAS (Joint University Accelerator School) Assistance for the MADX and Transverse Beam Dynamics courses.
Oct-Dec 2014	"Introduction to Accelerator Physics" EPFL course by Prof. Rivkin Helped with the MADX tutorial sessions and supporting the students.
Jan 2014	JUAS (Joint University Accelerator School) Assistance for the MADX and Transverse Beam Dynamics courses.

Languages

English:	Fluent
Italian:	Mother tongue
French:	Basic Knowledge

Particle Accelerators Related Skills

- Modelling of accelerator components and physics effects such as wakefields and radiation.

- Beam dynamic simulations, estimations of beam quality and stability in presence of single particle, collective and multi-bunch effects.

- Linear optics design and matching, basic techniques for correction of chromatism and non linearities, lattice optimisation.

- Orbit correction techniques (1:1, global steering, dispersion and wakefields-free steering).

- Tracking code development and maintenance, coding of fast numerical algorithms.

Computer Skills

Advanced Knowledge:	C/C++ (STL, Boost, GSL, GMP), GNU/Linux, LaTeX, Gnuplot
Intermediate Knowledge:	Matlab/Octave, TCL, Python, Bash, ROOT, GEANT4, Excel, Word, PowerPoint
Accelerator codes:	PLACET2 [1], PLACET, MADX, ELEGANT, OptiM

Familiar with the assembly of common hardware, GNU/Linux installation and configuration both desktop and server oriented.

Complementary Skills

Excellent communication skills. Ability to carry out small hand works. Maintenance, assembly and cleaning of detectors and vacuum systems. Experience with the usage of machine tools and programming of CNC machines.

Publications and Contributions

2016   *"Status of PLACET2"*, **Invited Talk** at CLIC Workshop

2015   *"Beam Dynamics Driven Design of the LHeC Energy Recovery Linac"*, D. Pellegrini, A. Bogacz, A. Latina, D. Schulte, Phys. Rev. ST Accel. Beams 18, 121004 (2015)
"CERN ERL Facility CDR", many authors, to be published
"Development of an ERL based TeV energy ep and eA Collider at CERN", O. Brüning *et al.*, ICFA Beam Dynamics Newsletter No. 68.
"Progress on the Large Hadron electron Collider", O. Brüning *et al.*, EPS-HEP2015 Vienna, Austria.
"Single and Multi-bunch End-to-end Tracking in the LHeC", D. Pellegrini, A. Bogacz, A. Latina, D. Schulte, IPAC'15, Richmond VA, USA, MOPJE066
"Applications of PLACET2 to the CTF3 Combiner Ring", D. Pellegrini, D. Gamba, A. Latina, R. Corsini, IPAC'15, Richmond VA, USA, MOPJE067
"PLACET2: A Novel Code for Beam Dynamics in Recirculating Machines", D. Pellegrini, A. Latina, D. Schulte, IPAC'15, Richmond VA, USA, MOPJE068
"Multi-bunch Tracking in Recirculating Machines", **Invited Seminar** at JLab
"Wakefield effects in LHeC ERL", **Invited Talk** at LHeC Workshop
"CERN SC RF and ERL Test Facility Plans", **Plenary Talk** at ERL'15, substituting A. Valloni
"LHeC ERL Design and Beam-Dynamics Issues", **Invited Talk** at ERL'15, shared with A. Bogacz

2014   *"Toolbox for Applying Beam-Based Alignment to Linacs"*, E. Adli, A. Latina, D. Pellegrini, J. Pfingstner, D. Schulte, Linac'14, Geneva, Switzerland, THPP034
"The LHeC project", **Invited Talk** at POETIC V Workshop at Yale University
"Multi-bunch wakefield effects", **Invited Talk** at LHeC Workshop

2013   *"Beam Dynamics Studies for the Injection System of a High Luminosity Flavour Factory"*, D. Pellegrini, S. Guiducci, M.E. Biagini, IPAC'13, TUPME008

2012   *"Beam dynamics studies and design of the LINAC-LER transfer line for the electron injector of SuperB"*, D. Pellegrini, S. Guiducci, INFN-12-24/LNF
"Baseline Design of the SuperB Factory Injection System", S.Guiducci *et al.*, IPAC'12, TUPPR088

2009   *"Experimental Setup for the Test of DANTE Detector"*, D. Pellegrini, J.J. Valiente Dobon, S. Brambilla, A. Gadea, INFN-LNL annual report, page 64.

---

[1] main developer

OTHER ACTIVITIES

Occasionally guiding tourists and students at CERN.